Stability of compressible boundary layers in presence of smooth roughness and wall temperature effects

by

Francis Lacombe

A thesis
presented to the University of Waterloo
in fulfillment of the
thesis requirement for the degree of
Doctor of Philosophy
in
Mechanical and Mechatronics Engineering

Waterloo, Ontario, Canada, 2022

Examining Committee Membership

The following served on the Examining Committee for this PhD comprehensive examination. The decision of the Examining Committee is by majority vote.

Supervisor: Jean-Pierre Hickey, Ph.D.
                          Assistant Professor, Department of Mechanical and
                          Mechatronics Engineering, University of Waterloo

Internal Member: John Wen, Ph.D.
                          Professor, Department of Mechanical and
                          Mechatronics Engineering, University of Waterloo

Internal Member: Serhiy Yarusevych, Ph.D.
                          Professor, Department of Mechanical and
                          Mechatronics Engineering, University of Waterloo

Internal-External Member: Kevin Lamb, Ph.D.
                          Professor, Department of Applied Mathematics,
                          University of Waterloo

External-External Member: Pedro Paredes, Ph.D.
                          Senior Research Engineer, National Institute of Aerospace
                          NASA Langley Research Center

Author's Declaration

I hereby declare that I am the sole author of this thesis. This is a true copy of the thesis, including any required final revisions, as accepted by my examiners.

I understand that my thesis may be made electronically available to the public.

Abstract

In natural laminar flow design, aircraft manufacturers aim to delay the laminar-to-turbulent transition by modifying the geometric features of the aircraft to stabilize the boundary layer. Yet, the transitional process is highly sensitive to surface imperfections; the presence of grooves, rivets or dimples, for instance, greatly affects the transitional properties of the flow and need to be considered for accurate predictive modelling. To this end, the nonlinear parabolized stability equations (NPSE) have shown promising predictive capabilities over a wide range of operating conditions. The NPSE are less dependent on experimental data, which is a step towards a generalizable transition model.

Here, we first present a novel NPSE-based numerical framework, developed in-house but made open-source, to investigate transition in compressible flows. The code can handle complex geometries and only requires the coordinates of the wall to generate an orthonormal computational grid. The mesh spacing is refined based on the curvature of the wall. The model is formulated in dimensionless variables, and the disturbances are discretized using a finite-bandwidth approach. Written in Python and leveraging well-established libraries, the framework includes a laminar flow solver using the same numerical formulation as the modal stability solver to remain consistent. The code is validated against published cases and large-scale Direct Numerical Simulations (DNS). It can serve as the basis for the future development of modal stability-based problems in aerospace engineering, geophysical, and multiphase flows.

The computational framework is used in combination with large-scale DNS to study the effect of smooth two-dimensional surface roughness on the stability characteristics of a canonical boundary layer flow under transonic conditions ($M = 0.714$). In particular, the influence of two-dimensional smooth roughness on the stability of 2D Tollmien-Schlichting (T-S) waves is investigated with a particular emphasis on frequency content generation. The DNS reveals a stronger destabilizing effect of the disturbance higher frequencies for the case featuring the highest roughness amplitude. This causes a rapid growth of secondary instabilities which skips the standard T-S mechanism and give rise to a cyclical transitional pattern in which both late K-type structures and premature bypass transition are observable. The modal stability analysis also shows that, in the presence of two-dimensional

smooth roughness, the mode experiencing the highest linear growth is three-dimensional.

Finally, the coupling effect between roughness and wall temperature inhomogeneities is investigated at transonic condition using the nonlinear parabolized stability equations (NPSE). To this end, the effect of localized heating and cooling strips on the stability of a flat plate boundary layer with zero pressure gradient at $M = 0.714$ is first investigated and confirms the stabilizing (destabilizing) effect of cooling (heating) strips. Then, the coupling effect between the wall roughness and heating strips is addressed by superimposing the effect of a smooth roughness patch, consisting of five sinusoidal, two-dimensional humps, to the numerical setup. The NPSE study reveals a catalytic coupling effect between the temperature strips and roughness. In other words, compared with the flat plate case, the stability of the flow is decreased in the presence of heating strips and roughness, and, inversely, increased in the presence of cooling strips and roughness.

Acknowledgements

My deepest gratitude goes to my supervisor and friend Prof. Jean-Pierre Hickey, for providing me with this Ph.D. opportunity. Your guidance was crucial and always laced with the highest respect. I am deeply thankful to you for the level of autonomy you gave me to pursue my research.

I would like to sincerely pay my special regards to all the members of the committee, for taking the time and effort to review the thesis in detail and provide such constructive feedback during the defence.

To the very people who supported me during this journey, thank you. Alexandra, for your love and emotional support in the most challenging moments. Namasté. My closest friends, who have endured me for the last 25 years. Vous êtes ma famille. My family, who taught me the value of perseverance and sparked my interest for the concept of stability.

More importantly, thank you Billie for high vitamin D intake.

Dedication

This is dedicated to the one who makes me feel home.

Table of Contents

List of Figures

xiv

List of Tables

List of Abbreviations

General

DNS Direct Numerical Simulations

CNSE compressible Navier-Stokes equation

RANS Reynolds Averaged Navier-Stokes Equations

CFD Computational Fluid Dynamics

LES Large Eddy Simulations

DES Detached Eddies Simulations

Modal Stability Theory

LST Linear Stability Theory

PSE Parabolized Stability Equations

NPSE Nonlinear Parabolized Stability Equations

LPSE Linear Parabolized Stability Equations

OWNS One-Way Navier-Stokes Equations

List of Symbols

Dimensionless Numbers

Re_δ Reynolds number based on δ

Ma Mach number

Pr Prandtl number

Greek symbols

γ Heat capacity ratio

δ Length scale, proportional to boundary layer thickness $\sqrt{\frac{x_0 \nu_0}{u_0}}$

λ Thermal conductivity

ρ Density

α Streamwise wavenumber

β Spanwise wavenumber

ω Temporal wavenumber

μ Dynamic viscosity

ν Kinematic viscosity

Letters

$\overline{q}$ Base flow vector $\{u, v, w, p, T\}^T$

q' Fluctuating flow vector $\{u', v', w', p', T'\}^T$

$\tilde{q}$ Fluctuating flow shape function vector $\{\tilde{u}, \tilde{v}, \tilde{w}, \tilde{p}, \tilde{T}\}^T$

x_i i^{th} dimension

u_i i^{th} component of velocity

$\mathcal{C}''$ Nonlinear forcing term (Continuity equation)

$\mathcal{M}''$ Nonlinear forcing term (Momentum equation)

$\mathcal{E}''$ Nonlinear forcing term (Energy equation)

$\mathcal{F}''$ Nonlinear forcing term vector $\{\mathcal{C}'', \mathcal{M}'', \mathcal{E}''\}^T$

T Temperature

p Pressure

Chapter 1

Introduction

At the 41st Assembly of the International Civil Aviation Organization (ICAO), the ICAO and its members agreed on "the necessity for the international air transport industry, to continuously improve CO_2 efficiency by an average of 1.5 percent per annum [...] and achieve a long-term goal of net-zero carbon emissions by 2050" [133]. To this end, aircraft manufacturers have made great efforts to reduce their dependence on fossil fuels. Among the possible cleaner alternatives, hydrogen could be a game changer, but requires significant infrastructure [62]; new sustainable aviation fuels promise a significant reduction in emissions, but can only provide an intermediate step toward carbon neutrality. On the other hand, the energy density of lithium batteries, in the current state of the technology, the energy density of lithium batteries is still an order of magnitude away from practical use in civil aviation [38]. In this light, the path leading to carbon neutrality will most likely involve technological advances in energy storage densities, which may include hydrogen, in combination with a drastic reduction of energy consumption. In this regard, significant gains in efficiency can be achieved through weight and drag reduction. Recent advances in the development of second-generation aluminum alloys for additive manufacturing offer more design freedom and should (hopefully) translate into more rigid structures at a fraction of the weight of the current designs. On the aerodynamic side, the prediction of the laminar-to-turbulent transition plays a key role in modern aerospace design. As the skin friction greatly increases in turbulent flows, there is an increasing impetuous to maintain a

stable laminar boundary layer over a large portion of the lifting surfaces and fuselage. Over the past decades, design strategies to mitigate drag have continuously evolved, and the use of topological optimization and laminar flow control (LFC) techniques is now becoming more common. Although the use of favorable pressure gradients in aircraft design can help in extending the laminar flow regions, geometric inhomogeneities and flow complexities—characteristic of aerospace devices—usually destabilize boundary layer flows and promote laminar-to-turbulent transition. The accurate prediction of transition in these complex compressible regimes remains an outstanding problem in the aerospace industry.

Transition prediction is also central to other aspects of aerospace design, for example, the prediction of engine stall under strong crosswind conditions. The efficiency of the engine is strongly dependent on the uniformity of the flow entering the front of the fan; at sufficiently high distortion levels, the fan blades may stall or encounter aerodynamic instabilities. When the engine is in operation but the plane is idling on the runway, a typical operating condition, severe crosswinds cause the flow entering the engine to separate from the nacelle, which results in flow distortion to the engine. The size of the flow separation is greatly affected by the location of the transition line on the nacelle, as the flow accelerates from the stagnation point to the lip of the nacelle. As a result, the size of the separation bubble and concomitantly the engine distortion level, is based on an accurate prediction of the laminar-to-turbulent transition [159]. None of the most existing RANS-based transition models is capable of accurately predicting the separation and transition phenomena of this complex three-dimensional compressible flow [31]. The aerospace industry requires a robust, yet high-fidelity, transition prediction tool to predict laminar-to-turbulent transition on realistically complex geometries and flow configurations; the present thesis contributes to this effort.

1.1   Motivation and objectives

Typically, the transition process in a subsonic laminar boundary layer along a wall is dominated by the formation of two-dimensional streamwise instability modes, also termed Tollmien-Schlichting (T-S) waves. For this class of flows at realistic operating conditions,

Direct Numerical Simulations (DNS) are out of reach in terms of computational resources. In this regard, an alternative is to use modal stability-based transition models which are up to three orders of magnitude cheaper than the equivalent DNS [86]. This is mainly due to the fact that in the PSE approach, the stability analysis is performed on the laminar base flow, whereas the spatial and temporal discretization in a DNS must be sufficiently refined to capture the nonlinearities and temporal fluctuations of the small scale turbulence after the transition onset. For this reason, for a compressible flow over a complex geometry, the PSE approach becomes even more advantageous.

The main goal of this research is to enhance transition prediction capabilities in realistic aeronautical conditions with surface imperfections. To this end, the transition prediction model must be applicable to handle complex flows that feature compressibility effects, adverse pressure gradients, nonadiabatic surface effects, and roughness-induced bypass transition over complex geometries. In this regard, the modal stability theory has shown encouraging results in such complex flows. However, most modal-stability-based transition models are highly dependent on experimental data (Linear Stability Theory, Linear Parabolized Stability Equations, Bi-Global) or have mostly been applied to simple geometries such as flat plates, hypersonic cones, pipe flows, or axisymmetric jets (Nonlinear Parabolized Stability Equations, Global stability theory). This research advances the prediction of transitions in more realistic compressible high-speed flows in complex geometries using a nonlinear modal stability approach in combination with high-fidelity simulations. From a physical point of view, the proposed approaches will be used to study the nonlinear growth and breakdown of wavepackets in the presence of roughness elements, pressure gradient, and cross-flow. More specifically, the current research aims to answer the following questions:

- Is the PSE framework a sufficiently accurate tool to study the evolution of modal-like disturbances in complex compressible flows subject to smooth wall roughness (or wavyness) and nonhomogeneous wall temperature effects?

- What is the impact of two-dimensional smooth roughness on the modal and nonmodal growth of instability in transonic boundary layer flows?

- Is there an interdependence between wall roughness (or wavyness) and wall temperature on the flow stability?

- Can smooth roughness be used in combination with localized heating or cooling to enhance stabilization in transonic boundary layer flows?

To answer these questions, the following contributions are made in the present thesis.

1. Development of an open-source solver for the compressible Nonlinear Parabolized Stability Equations (NPSE) in curvilinear coordinates capable of studying the modal growth of instability in the presence of smooth roughness. To the best of our knowledge, this is the only openly available modal stability code that combines

   - Variable properties for both the fluctuations and the base flow
   - A consistent base-flow and stability solver
   - Consistent numerical stabilization
   - Automatic orthonormal grid generation
   - Automatic grid refinement based on the curvature of the wall
   - Finite-bandwidth disturbance representation

2. Implementation of curvilinear coordinates in a massively parallel DNS code and conduction of large-scale simulations of a compressible transitional boundary layer flow subject to smooth roughness. This objective serves three purposes:

   (a) Assess the applicability of the NPSE to study the modal growth of instabilities in the presence of two-dimensional smooth roughness

   (b) Identify the role of roughness on the modal and nonmodal growth of disturbances.

   (c) Determine whether the presence of two-dimensional roughness favors the onset of span-periodic instability.

3. Establishing, by means of an NPSE-based parametric study, whether there exists an interdependence between wall roughness (or waviness) and wall temperature on the flow stability?

4. Assessing, by means of an NPSE-based parametric study, the possibility of using localized roughness to enhance the efficacy of temperature-based flow control devices.

1.2 Outline of the thesis

This thesis is organized as follows. Chapter 2 presents a brief review of the literature on laminar-to-turbulent transition and discusses the main modeling strategies that are relevant to the current research. Additionally, Chapters 4 to 6 are based on submitted or prepared manuscripts, thus they contain a more specific review of the literature relevant to that section. Chapter 3 defines the governing equations and presents the theoretical background of modal stability theory. This is also where we present the numerical framework, the curvilinear coordinate system implementation, and the resolution algorithms. The chapter 4 presents the main motivation behind the development of an open-source NPSE solver and gives an overview of the main capabilities of the solver through some illustrative examples. Chapter 5 discusses the role of two-dimensional roughness in the modal growth of the T-S instability in compressible boundary layer flow. In this chapter, we present a detailed description of the cases of interest, including a detailed description of the DNS configuration. In Chapter 6, we investigate the intricate effect of heating and cooling on the transitional characteristics of flows from the boundary layer subject to localized smooth roughness. Finally, in Chapter 7 the major conclusions drawn from this body of work are presented in addition to providing some suggestions for future research.

The material presented in this thesis and the research contributions made during the doctoral studies are summarized in the following works:

- Journal papers:

  - Francis Lacombe and Jean-Pierre Hickey, "Krypton: Nonlinear Parabolized Stability Equation solver for transonic flow in curvilinear coordinates", SoftwareX, Volume 20, 101206, (2022) - **Chapter 4 in thesis**

  - Francis Lacombe, Subhajit Roy, Krishnendu Sinha, Sebastian Karl, and Jean-Pierre Hickey, "Characteristic Scales in Shock–Turbulence Interaction" AIAA Journal 59:2, 526-532, (2021)

  - Francis Lacombe and Jean-Pierre Hickey, "The role of two-dimensional smooth roughness on the modal growth of instability in compressible boundary layer flow", Journal of Fluid Mechanics, (under review) **Chapter 5 in thesis**

  - Francis Lacombe and Jean-Pierre Hickey, "Boundary layer stabilization via thermodynamic roughness," Physical Review Fluid, (to be submitted) **Chapter 6 in thesis**

- Conferences:

  - Francis Lacombe and Jean-Pierre Hickey, "Roughness-induced laminar-turbulent transition prediction over complex geometries", American Physical Society- Division of Fluid Dynamics, Atlanta, Georgia (2018)

  - Francis Lacombe and Jean-Pierre Hickey, "Roughness-induced transition prediction over complex geometries with linear parabolized stability equations (LPSE)", 11th International Symposium on Turbulence and Shear Flow Phenomena, Southampton, UK (2019)

  - Subhajit Roy, Krishnendu Sinha, Francis Lacombe and Jean-Pierre Hickey, "Anisotropic turbulent heat flux modelling through shock waves", AIAA Aviation, Dallas, Texas (2019)

- Sebastian Karl, Jean-Pierre Hickey and Francis Lacombe, "Reynolds stress models for shock-turbulence interaction", International Symposium on Shock Waves, Nagoya, Japan (2017)

- Open-source contributions:

  - Git repository : https://git.uwaterloo.ca/flacombe/krypton-softwarex.git

  - Language: Python3

  - Legal code license: GPL

Chapter 2

Literature review

> When I meet God, I am going
> to ask him two questions: Why
> relativity, and why turbulence?
> I really believe he will have an
> answer for the first.

Werner Heisenberg

In this chapter, we provide a brief review of the literature on the transition to turbulence
and discuss the main modeling strategies.

2.1   Transition to turbulence

There are multiple definitions of turbulence; the definition of Lewis Richardson is particu-
larly colorful: "Big whorls have little whorls, which feed on their velocity, and little whorls
have lesser whorls, and so on to viscosity" [153]. Taking this definition in a literary sense,
studying transition comes down to studying the formation of the very first 'big whorls.'
The underlying physics behind the formation of these first whorls is highly dependent on
the type of flow. Depending on the geometry and initial conditions, the transition to tur-

8

bulence will occur following a given mechanism, or sometimes a combination of multiple mechanisms. For boundary layers, the level of understanding behind each transition mechanism varies greatly from a nearly complete understanding (natural transition) to a more limited understanding (bypass transition, especially in complex flows). Here, we describe the main mechanisms that lead to transition in boundary layers.

2.1.1 Natural transition

The *natural transition*, also commonly called *normal transition*, occurs in flows where the background noise or the turbulence level of the freestream is low [174] and generally follows path A, in Figure 2.1. Typically, for low intensity of freestream turbulence (Tu < 1%) [156], boundary layer transition over a perfectly smooth flat plate follows a natural transition. In the subsonic regime, the normal transition commonly occurs in boundary layer flows and is characterized by the formation and development of two-dimensional Tollmien-Schlichting (T-S) waves. The term T-S wave is used to refer to the most unstable modal instability in the flow. In subsonic flows over a zero-pressure gradient flat plate, it is commonly accepted that the most unstable mode is two-dimensional and that its frequency mostly depends on the Reynolds number. With that in mind, the transition process in boundary layer flows is divided into two main steps. The first step is called *receptivity*, it is a mechanism by which external perturbations enter the boundary layer and cause disturbance within it. Possible sources of external disturbances include acoustic disturbances in the freestream, vortical waves or even discretization errors in numerical simulations. Typically, acoustic waves, present in the free stream, begin to interact with another disturbance, for example, wall roughness. Their mixing produces a forcing term that excites the boundary layer and generates the very first wave of instability [161]. This instability wave usually corresponds to the most unstable eigenmode of the Orr-Sommerfeld equation, i.e., the mode that will experience the highest amplification at a given location. The Orr-Sommerfeld equation is an eigenvalue problem that describes the shape of a two-dimensional modal disturbance in a parallel flow. The second step, characterized by the modal *growth* of the disturbances, is divided into two sub-steps: the linear and the nonlinear growth of the disturbance eigenmodes. The linear stability theory has proven to be successful at predicting the linear

9

eigenmode growth in a variety of flows ranging from the typical Blasius boundary layer, to more general shear flows such as in jets or channels. In the second sub-step, the amplitude of the fluctuation eigenmodes will reach a point where the growth is predominantly governed by nonlinear interactions. At this point, because of the rapid growth of higher harmonics, the flow gradually develops a spanwise periodicity, visible by the formation of H-type, or K-type structures, depending on the environmental disturbance intensity. H-type and K-type structures are characterized by the formation of staggered and aligned Λ-shaped vortices, respectively. Ultimately, the breakdown to turbulence will be triggered by the rapid growth of broad-band perturbations [164].
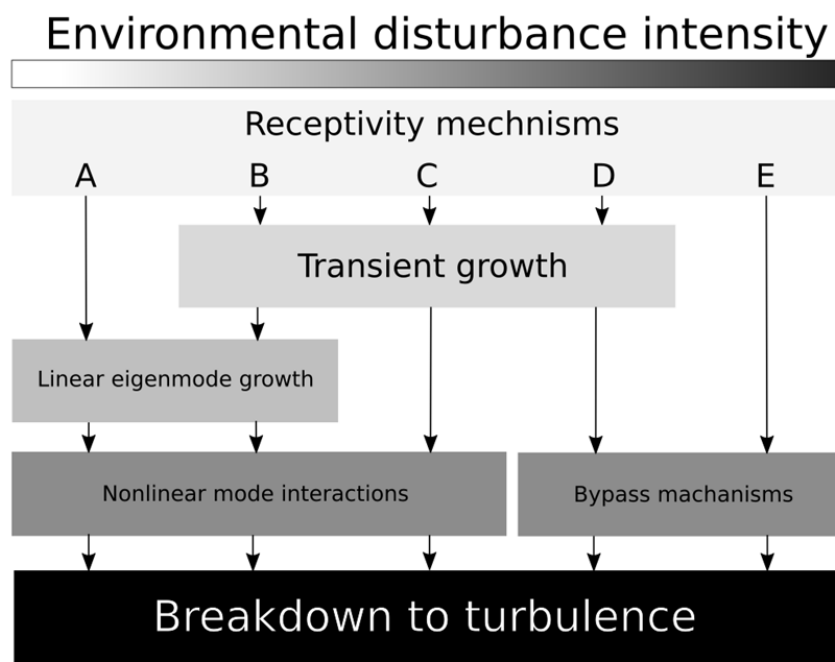
FIGURE 2.1. Paths to turbulence in BL flows. Figure adapted from [161]

These Regions bypassed for bypass transition

Region 1	Region 2	Region 3	Region 4	Region 5
TS Waves	Spanwise Vorticity	Three-Dimensional Breakdown	Turbulent Spots	Fully Turbulent Flow
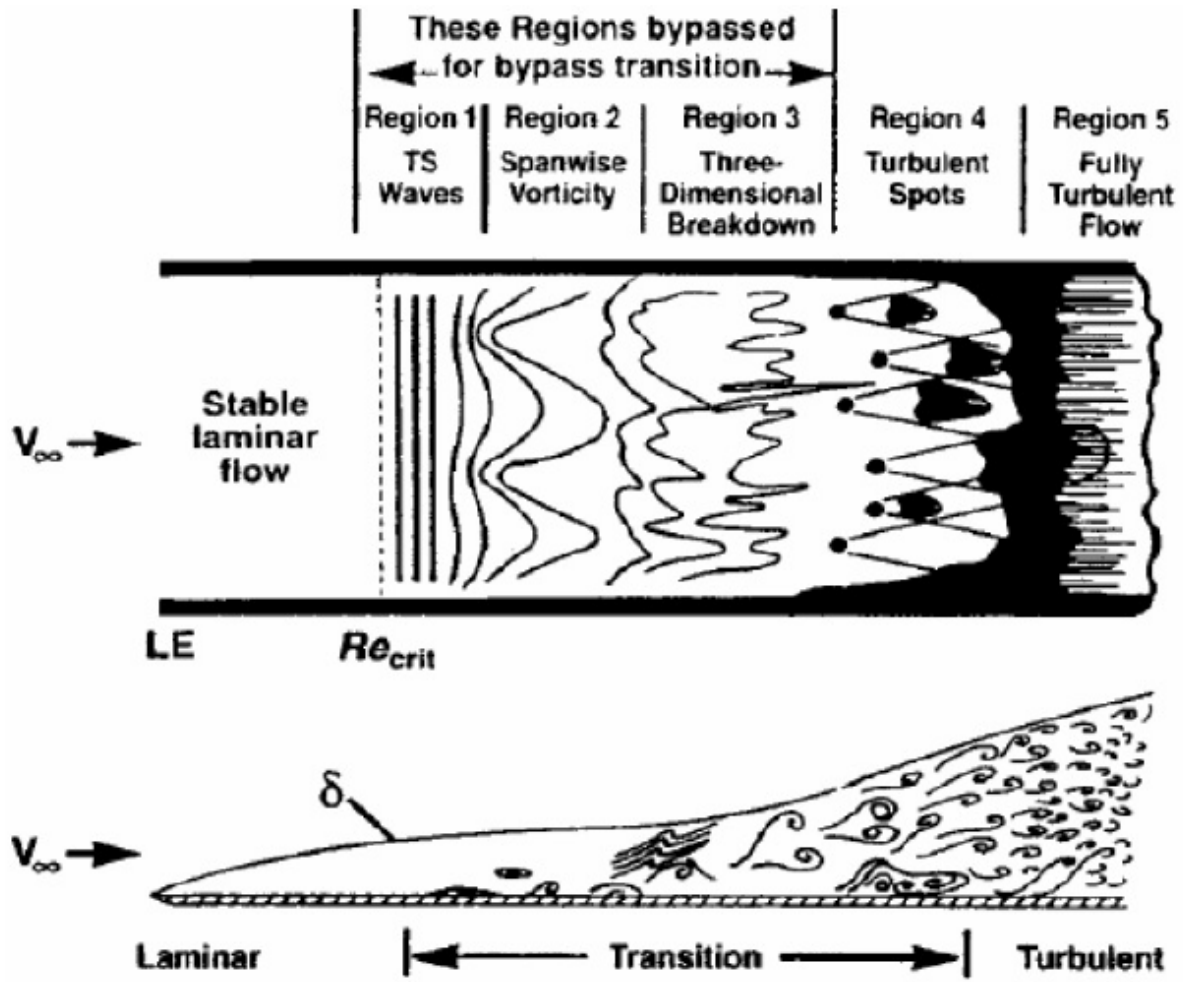
FIGURE 2.2. The natural transition process, reproduced from [60]

11

2.1.2 Bypass transition

Bypass transition is a generic term used to describe any transitional process that bypasses or skips the classical modal growth of the perturbation. The most common cause of bypass is free-stream turbulence [161] in which the perturbation follows path E in Figure 2.1. Under these conditions, the modal growth of the perturbations is skipped, and the flow becomes turbulent extremely rapidly. An illustration of the bypassed regions of the transition is shown on Figure 2.2. Bypass transition is still an area of ongoing research. There exist multiple mechanisms and emergent structures that lead to a bypass transition, most of which are not fully understood, and many remain to be identified. Many of these open questions are highlighted by the recent Annual Review of Fluid Mechanics paper on transitional turbulent spots [212], one of the common structures arising in bypass transition. However, it is generally accepted that the initial conditions that lead to the bypass transition cannot be studied with *linear* stability theory. Other examples of bypass transition include Poiseuille pipe flow (although sometimes assumed to follow path C), hypersonic blunt body paradox, distributed roughness effects on flat plates or cones, and subcritical transition observed on spherical forebodies [141, 152]. In some cases, the bypass transition is triggered by the interaction of a high-shear layer and streamwise vortices caused by discrete roughness elements [131], suction/blowing at the wall, trip wires, or body forces [215]. On a more nuanced note, transient growth has been suggested as a precursor of bypass transitions in regions where disturbance growth is algebraic, but modes are spectrally stable [198, 29, 152]. Bypass mechanisms could therefore be much more prevalent than Figure 2.1 might suggest, as many low-disturbance environment problems, such as high-speed aeronautical flows, feature high shear layers, roughness or surface inhomogeneities.

2.1.3 Compressibility and transition

Increasing the freestream Mach number results in an increase in the temperature in the boundary layer. Under the action of shear forces, more energy of the boundary layer is dissipated in the form of heat. The temperature reaches its maximum value in the near-wall region and gradually decreases to its freestream value as the shear decreases. This

has the effect of decreasing the density and increasing the viscosity in the lower region of the boundary layer, resulting in a locally lower Reynolds number. In subsonic flows, this stabilizing effect is subtle and tends (mostly) to reduce the frequency of the most unstable T-S mode. For this reason, it is generally assumed that under the subsonic regime the transition is delayed by compressibility, but its impact is too small to change the physical mechanism leading to turbulence [49, 22]. If the Mach number increases to within the supersonic regime, other factors will eventually come into play. The presence of a strong shock near the leading edge, the emergence of an entropy layer, and high wall heating as a result of strong viscous interactions are just a few examples of phenomena that impact flow stability as the Mach number increases [5]. In the high supersonic regime, these effects intensify and eventually impact the transition mechanism. Mack found that the dominant waves of instability that lead to the transition to turbulence in smooth zero-pressure gradient flat plate flows are the first and second modes [116]. The first mode is essentially an inviscid instability related to the inflection of the velocity profile. The second mode, also inviscid, originates from acoustic wave resonance that propagates between the wall and the sonic line in the laminar boundary layer [49]. In the supersonic regime, the damping effect of compressibility starts to progressively weaken. Above $Ma > 1.6$, the inviscid instability increases and progressively manifests at lower Reynolds numbers. For an insulated wall at $Ma > 3.8$, the dominant mode is the second mode [116].

2.2   Transition Modeling

Modeling transition is not an easy task, as multiple pathways can lead to turbulence. Depending on the geometry and flow conditions, one or the other of the transition modes may dominate the process. On rare occasions, more than one transition mode may prevail. Nevertheless, there exist three different approaches to studying laminar-to-transition. The first consists in removing any additional modeling assumptions from the Navier-Stokes equations through the use of Direct Numerical Simulations (DNS). Although DNS can virtually simulate any type of transition process, this approach is extremely computationally expensive and is rarely applied to industrial problems under realistic conditions. The second approach consists of statistical-based models, which can be integrated into typical

13

RANS frameworks. The main concept behind most RANS transitional models is to relate local variables (velocity, vorticity, wall distance, etc.) to the kinetic energy production term through an empirical correlation based on experimental data. RANS approaches usually lead to acceptable results for the class of problems for which they were optimized. The most notable model is the $\gamma - Re_\theta$ model which solves two additional equations, for intermittency (γ) and momentum thickness Reynolds Number (Re_θ), to relate the onset of turbulence to the local vorticity Reynolds number Re_ω. Although this model is still under development and was recently extended to account for cross-flow instabilities [174], it presents some major shortcomings. As the model was developed using experimental data, it makes it hard to generalize as it is "virtually impossible to include all mechanisms into a physic-based equation framework" [174]. Finally, the modal stability approach includes all the models derived from Prandtl's small disturbance hypothesis, including the Linear Stability Theory (LST), the Parabolized Stability Equations (PSE), the Global stability theory and, more recently, the One-way Navier-Stokes (OWNS) [195, 89]. In modal stability theory, the perturbation vector is expanded in spectral space, and the stability analysis is performed separately on each of its eigenmodes. Most linear-modal-stability-based models rely on empirical correlations to relate the transition onset position to the amplification factor of the most unstable mode. Nonlinear methods, such as the Nonlinear Parabolized Stability Equations (NPSE), account for the nonlinear interactions between the eigenmodes and can accurately predict the amplitude of the perturbations; the transition is thus triggered once the perturbations' amplitude reaches a certain threshold. There exist other methods, such as the so-called laminar kinetic energy method[139] or nonmodal methods [166]; however, these methods fall out of the scope of this research.

2.3   Transition over inhomogeneous walls

The effect of surface inhomogeneities on the transitional characteristics of boundary layers has been addressed by several experimentalists. Klebanoff's work [96] helped identify stationary disturbances and characterize their destabilizing effect on modal instability in the wake of two-dimensional roughness elements. More recently, the work of Kotsonis suggested a similar effect in the presence of discrete roughness elements [224]. Zoppini conducted a

comparative study in a similar setup using a combination of experiments and NPSE and observed more complex, possibly nonmodal mechanisms [223]. However, most experimental studies on this topic were in the subsonic regime. On the DNS side, only relatively simple flows are within reach of the current computing power, but with the continued technological advancements, we are just beginning to see DNS at a practical transitional Reynolds number [7]. The first hydrodynamic instabilities studied by direct numerical simulations were conducted by Fasel [51] in 1976 who characterized the stability of an incompressible Blasius flow. In the following decades, others have investigated different aspects of the laminar to turbulent transition [87, 88, 52, 76]. Such numerical experiments, although limited to incompressible low-speed flows, have laid the groundwork for the observation of two basic secondary instabilities. That is, fundamental and subharmonic breakdowns [19], which are characterized by the formation of staggered or aligned Λ-structures. In the last decade, we have seen increased interest from the modeling community toward the study of alternative transition mechanisms such as bypass [165, 213, 171, 215] and, with growing interest for military and space applications, hypersonic transition [220, 64, 40, 176, 192]. Transient growth has been suggested as a possible route for multiple cases of bypass transition, many of which feature discrete roughness elements [210, 141, 45, 152]. Direct numerical simulations of transition in the presence of roughness have been studied mainly in the supersonic [131, 175, 135, 10] and hypersonic [39, 220, 47, 184] regimes. On this topic, probably the most relevant work for the current thesis is that of Suman [131], who studied the effect of distributed surface roughness on the stability of supersonic ($Ma > 2.9$) boundary layers. The results of his simulation show that the presence of wavyness tends to create a strong shear above the boundary layer, and also generates streamwise vortices. The interaction between the shear layer and these vortices causes the breakdown to turbulence. In the subsonic regime, the transition to turbulence usually follows a normal path characterized by the growth of two-dimensional T-S instabilities. In the supersonic regime, the most unstable mode is usually three-dimensional, and the transition is ultimately caused by the rise of secondary instabilities. Under hypersonic conditions, the most dominant instability mode is two-dimensional [116], but the flow reacts differently to surface inhomogeneities. For example, the effect of wall cooling is stabilizing for supersonic and subsonic boundary layer flow, but it is destabilizing in the hypersonic regime [181, 118]. The effect of wall

perturbations is, therefore, extremely dependent on the flow regime. This thesis seeks to fill the literature gap in the investigation of surface inhomogeneities such as smooth roughness or wavyness and nonadiabatic surface effects in the transonic regime. A more detailed literature review on the topics of wall roughness and nonadiabatic effects in the context of transition is given in Chapters 5 and 6.

Chapter 3

Stability Theory: theory and numerical tools

The motion of a fluid in continuum mechanics is governed by the Navier-Stokes equations. These equations are, in fact, classical conservation laws and can be simplified, under appropriate assumptions, to develop different branches of the stability theory. The simplification of the governing equations and the relevant assumptions are summarized in Section 3.1 after which the basis for local (Section 3.2) and nonlocal (Section 3.3) stability theory is presented. This chapter concludes with a summary of the Parabolized Stability Equation (Section 3.4) and Direct Numerical Simulations (Section 5.2.3) framework.

3.1   Governing equations

In this section, we describe the general derivation steps of various modal stability theories. We begin by stating the governing equations. Here, we use the dimensionless compressible Navier-Stokes equations (CNSE) in their non-conservative form. The non-conservative formulation is selected as the focus is put primarily on subsonic flows (without shock waves) and, more importantly, because of the convenience handling the primitive thermodynamic variables, such as pressure, without conversions. The modified conservation of mass, mo-

mentum, and energy, in non-conservative form, reads:

$$-pT\frac{\partial u_i}{\partial x_i} = T\left[\frac{\partial p}{\partial t} + u_i\frac{\partial p}{\partial x_i}\right] - p\left[\frac{\partial T}{\partial t} + u_i\frac{\partial T}{\partial x_i}\right] \tag{3.1}$$

$$\rho\left[\frac{\partial u_i}{\partial t} + u_j\frac{\partial u_i}{\partial x_j}\right] = -\frac{\partial p}{\partial x_i} + \frac{1}{Re_\delta}\frac{\partial}{\partial x_j}\left[\mu\left(\frac{\partial u_i}{\partial x_j} + \frac{\partial u_j}{\partial x_i}\right) - \frac{2}{3}\mu\frac{\partial u_k}{\partial x_k}\delta_{ij}\right] \tag{3.2}$$

$$\rho c_p\left[\frac{\partial T}{\partial t} + u_j\frac{\partial T}{\partial x_j}\right] = \frac{1}{Re_\delta Pr}\frac{\partial}{\partial x_i}\left(\lambda\frac{\partial T}{\partial x_i}\right) + (\gamma-1)Ma^2\left(u_i\frac{\partial p}{\partial x_i}\right)$$
$$+ \frac{(\gamma-1)Ma^2}{Re_\delta}\left[\mu\left(\frac{\partial u_i}{\partial x_j} + \frac{\partial u_j}{\partial x_i}\right) - \frac{2}{3}\mu\frac{\partial u_k}{\partial x_k}\delta_{ij}\right]\frac{\partial u_i}{\partial x_j} \tag{3.3}$$

Where the flow properties are governed by the *dimensionless* Ideal Gas Law equation. The viscosity and conductivity are deduced from Sutherland's law

$$\bar{\rho} = \gamma Ma^2\frac{\bar{p}}{\bar{T}} \qquad\qquad \bar{\mu} = \frac{C_1 T^{3/2}}{T+S} \qquad\qquad \bar{\lambda} = \frac{C_2 T^{3/2}}{T+S} \tag{3.4}$$

3.1.1 Dimensionless variables

The use of dimensionless variables can greatly simplify any mathematical problem to a minimum number of physically meaningful key variables. Equations (3.1)-(3.3) were nondimensionalized using a classical approach[127] with the following set of dimensionless variables:

$$x_i = \frac{x_i^*}{\delta} \qquad u_i = \frac{u_i^*}{u_0} \qquad T = \frac{T^*}{T_0} \qquad p = \frac{p^*}{p_s}$$
$$\mu = \frac{\mu^*}{\mu_0} \qquad \rho = \frac{\rho^*}{\rho_0} \qquad c_p = \frac{c_p^*}{c_{p0}} \qquad \lambda = \frac{\lambda^*}{\lambda_0} \tag{3.5}$$

Where $\delta = \sqrt{\frac{x_0\nu_0}{u_0}}$ is a length scale that is *proportional* to the inlet boundary layer thickness and $p_s = \rho_0 u_0^2$ is the pressure scale. The dimensional quantities are defined with the asterisk (*). The subscript 0 represents the reference quantities, typically the conditions of

the freestream. Therefore, the reference thermodynamic conditions must ensure that the equation of state is satisfied.

$$p_0 = \rho_0 R_0 T_0 \tag{3.6}$$

Reference Reynolds and Mach numbers are defined as

$$Re_\delta = \sqrt{\frac{u_0 x_0}{\nu_0}} \qquad\qquad Ma = \frac{u_0}{\sqrt{\gamma R_0 T_0}} \tag{3.7}$$

In practice, the following reference quantities are set to

$$Ma = \text{Value} \qquad\qquad Re_\delta = \text{Value} \qquad\qquad Pr = 0.71$$
$$\rho_0 = 1. \qquad\qquad u_0 = 1. \qquad\qquad T_0 = 1.$$

The other reference quantities are deduced from the set nondimensional variables:

$$\nu_0 = \frac{u_0 x_0}{Re_\delta^2} \qquad\qquad p_s = \rho_0 u_0^2 \tag{3.8}$$

3.1.2   Modal stability equations

Modal stability theory is a branch of fluid mechanics that has been developed to study the evolution of small-amplitude perturbations within a variety of flows. It is based on the decomposition of flow quantities into a steady part $\overline{q}$ and an unsteady part q' [86]:

$$q(\vec{x}, t) = \overline{q}(\vec{x}) + q'(\vec{x}, t) \tag{3.9}$$

Here, $\vec{x}$ is the spatial coordinate vector and t is the time. Substituting equation (3.9) into the compressible Navier-Stokes equations and neglecting the product of fluctuating components (nonlinear terms) leads to the *Linearized Compressible Navier-Stokes Equations*:

$$\frac{\partial u_i'}{\partial x_i} + \left(\frac{T'}{\overline{T}} + \frac{p'}{\overline{p}}\right)\frac{\partial \overline{u}_i}{\partial x_i} = \frac{p'}{\overline{p}\,\overline{T}}\frac{\overline{DT}}{\overline{Dt}} + \frac{1}{\overline{T}}\left[\frac{\overline{DT'}}{Dt} + u_i'\frac{\partial \overline{T}}{\partial x_i}\right]$$

$$- \frac{T'}{\overline{p}\,\overline{T}}\frac{\overline{Dp}}{\overline{Dt}} - \frac{1}{\overline{p}}\left[\frac{\overline{Dp'}}{Dt} + u_i'\frac{\partial \overline{p}}{\partial x_i}\right] + \mathcal{C}'' \tag{3.10a}$$

$$\overline{\rho}\left[\frac{1}{\overline{p}}p' - \frac{\overline{\rho}}{\overline{T}}T'\right]\frac{\overline{D\overline{u}}}{\overline{Dt}} + \overline{\rho}\left[\frac{\overline{Du_i'}}{\overline{Dt}} + u_j'\frac{\partial \overline{u}_i}{\partial x_j}\right] = -\frac{\partial p'}{\partial x_i} + \frac{1}{Re}\frac{\partial \sigma_{ij}'}{\partial x_j} + \mathcal{M}'' \tag{3.10b}$$

$$\overline{\rho}c_p\left[\frac{1}{\overline{p}}p' - \frac{1}{\overline{T}}T'\right]\frac{\overline{DT}}{\overline{Dt}} + \overline{\rho}c_p\left[\frac{\overline{DT'}}{\overline{Dt}} + u_j'\frac{\partial \overline{T}}{\partial x_j}\right] = \frac{1}{RePr}\frac{\partial}{\partial x_i}\left(\lambda'\frac{\partial \overline{T}}{\partial x_i} + \overline{\lambda}\frac{\partial T'}{\partial x_i}\right)$$

$$+ (\gamma - 1)M^2\left(\overline{u}_i\frac{\partial p'}{\partial x_i} + u_i'\frac{\partial \overline{p}}{\partial x_i}\right) + \frac{(\gamma - 1)Ma^2}{Re}\phi_{ij}' + \mathcal{E}'' \tag{3.10c}$$

The nonlinear vector $\mathcal{F}''$ is defined as $\{\mathcal{C}'', \mathcal{M}'', \mathcal{E}''\}^T$ and the total derivative operator, $\frac{\overline{D}}{\overline{Dt}}$, is defined as:

$$\frac{\overline{D}}{\overline{Dt}} = \frac{\partial}{\partial t} + \overline{u}_j\frac{\partial}{\partial x_j} \tag{3.11}$$

In modal stability theory, the perturbations are assumed to be oscillatory in time and/or space, and the stability is studied on a mode-dependent basis. In this regard, the perturbation vector in equation (3.9) is assumed to be of the following form:

$$q'(\vec{x}, t) = \hat{q}(\vec{x})\chi(\vec{x}, t) = \hat{q}(\vec{x})e^{i\theta} \tag{3.12}$$

Where $\hat{q}$ and χ are the amplitude and phase functions, respectively. This constitutes the starting point of all modal stability theories. From there, different simplifications can be made on the amplitude and/or phase functions and lead to different branches of modal stability theory (*local*, *nonlocal*, *global*).

The perturbed flow properties are deduced from

$$\rho' = \frac{\partial \overline{\rho}}{\partial \overline{p}}p' + \frac{\partial \overline{\rho}}{\partial \overline{T}}T' \qquad\qquad \mu' = \frac{d\overline{\mu}}{d\overline{T}}T' \tag{3.13}$$

3.2 Local stability analysis

Assuming $\vec{x} = [x, y, z]^T$, where x, y, z represents the stream, normal, and span dimensions. The *local* stability theory relies on the ansatz that the perturbation vector q' grows (or decays) following a quasi-static process. Thus, the stability analysis is carried out at a specific *local* position and does not account for the evolution of the perturbation along its path [86]. This approach is valid if we assume that the flow is *parallel*. Furthermore, in a Blasius boundary layer, since the flow is also homogeneous in z, the amplitude function can only vary in the normal direction. This leads to the following form for the perturbation vector:

$$q' = \hat{q}(y) \exp(i(\alpha x + \beta z - \omega t)) \tag{3.14}$$

Where $\hat{q}$ is the perturbation shape function and $\exp(i(\alpha x + \beta z - \omega t))$ is the phase function. The shape function is what gives the perturbation its physical shape, i.e. this is what we see in the root mean squared signal. The phase function is what gives the perturbation its amplitude and oscillatory behavior. Substituting the perturbation vector (3.14) into equations (3.10a)-(3.10c) and neglecting the nonlinear interactions leads to the following system of equation:

$$\mathcal{L}\vec{\phi} + \mathcal{L}_y \frac{d\vec{\phi}}{dy} + \mathcal{L}_{yy} \frac{d^2\vec{\phi}}{dy^2} = \vec{0} \tag{3.15}$$

Where $\vec{\phi} = [\hat{u}, \hat{v}, \hat{w}, \hat{p}, \hat{T}]^T$ and the matrices $\mathcal{L}$, $\mathcal{L}_y$ and $\mathcal{L}_{yy}$ depend only on the mean flow quantities and wavenumbers (α, β, ω). The equation (3.15), is the basis of the linear *local* stability theory –usually simply termed *Linear Stability Theory*. To solve this system, we must first define boundary conditions that are consistent with the nature of the base flow. The term *base flow* refers to the laminar flow on which the stability analysis is performed. It is different from the mean flow, which includes both the base flow and the mean flow distortion. This nuance will be discussed in Section 5.2.2. The LST is usually applied to simple cases such as self-similar flows (Blasius, Falkner-Skan-Cooke, jets, etc.). Each of these examples requires the definition of specific boundary conditions. Here, we focus on general boundary layer flows and assume a disturbance-free freestream and vanishing fluctuating velocities at the wall, due to the no-slip condition. Assuming an isothermal wall,

the temperature fluctuation is also assumed to be null at the wall. The only inhomogeneous boundary condition is the fluctuating wall pressure $\hat{p}(0)$. The boundary conditions read:

$$\hat{u}(0) = \hat{v}(0) = \hat{w}(0) = \hat{T}(0) = \hat{p}(0) - 1 = 0 \tag{3.16}$$

$$\hat{u}_y(\infty) = \hat{v}_y(\infty) = \hat{w}_y(\infty) = \hat{p}_y(\infty) = \hat{T}_y(\infty) = 0 \tag{3.17}$$

The boundary condition on $\hat{p}$ serves two purposes: (1) to avoid the trivial solution; and (2) to provide a scaling to the solution. The main flaw in local stability theory is its inability to account for the growth of the boundary layer and *history effects* of the perturbation. The nonlocal stability theory circumvents these weaknesses.

3.3   Nonlocal stability analysis

In the *nonlocal* stability analysis, the *history effects* associated with the spatial variation of the perturbations and the varying base flow properties are taken into account [86] which results in a streamwise dependency of both the amplitude and the phase functions. The motivation behind the development of the nonlocal stability theory was driven by the need for an efficient tool to study the propagation of perturbations along the stream direction but to avoid the necessity of solving an elliptic system of equations. This is only achievable if the second derivative in the streamwise direction $\partial_x^2 \hat{q}$ is neglected, effectively transforming the elliptic-nature of the partial differential equation set into a *parabolic form*. This simplification only holds if the flow is slowly varying in the streamwise direction such as in boundary layers, jets or channels. For example, in a Blasius boundary layer, $\partial_x^2 \hat{q}$, scales with $O(Re_\delta^{-2})$ and is negligible compared to $\partial_x \hat{q}$ which scales with $O(Re_\delta^{-1})$. As a result, it is possible to derive a parabolic system of equations that can be solved incrementally along the streamwise direction to study the stability of downstream-propagating modal perturbations. First introduced by Hall [65], the idea of studying the evolution of T-S waves through the Parabolized Stability Equations (PSE) was further developed by Itoh [83] and Bertolotti [15, 14, 193, 16], who extended the method further with the *Nonlinear Parabolized Stability Equations (NPSE)*, which can account for the modal interactions. The nonlinear effects are addressed in Section 3.3.2, in the current section, we first focus

on the *Linear* PSE. In the *Linear* PSE (LPSE) approach, the perturbation vector takes the following form:

$$q' = \hat{q}(x,y) \exp\left(\int^x i\alpha(x)dx + i\beta z - i\omega t\right) \tag{3.18}$$

Introducing equation (3.18) into (3.10a)-(3.10c) leads to the following system of equations

$$\mathcal{L}\vec{\phi} + \mathcal{L}_y \frac{\partial\vec{\phi}}{\partial y} + \mathcal{L}_{yy}\frac{\partial^2\vec{\phi}}{\partial y^2} = \mathcal{L}_x \frac{\partial\vec{\phi}}{\partial x} \tag{3.19}$$

Where the matrices $\mathcal{L}$, $\mathcal{L}_y$ and $\mathcal{L}_{yy}$ are the same as in (3.15) while the matrix $\mathcal{L}_x$ accounts for the streamwise derivatives. The boundary conditions are also similar to those of the LST except that the condition on $\hat{p}$ at the wall is relaxed since $\frac{\partial\hat{p}}{\partial x}$ is no longer neglected.

$$\hat{u}(0) = \hat{v}(0) = \hat{w}(0) = \hat{T}(0) = 0 \tag{3.20}$$

$$\hat{u}_y(\infty) = \hat{v}_y(\infty) = \hat{w}_y(\infty) = \hat{p}_y(\infty) = \hat{T}_y(\infty) = 0 \tag{3.21}$$

3.3.1 Normalization condition

In the PSE approach, the streamwise wave number α is also a variable in the problem and thus the system lacks closure as we have more variables than equations. An additional equation is needed to close the system. For this purpose, we introduce the so-called *Normalization condition* (or *Auxiliary condition*) [86, 218], given by equation (3.22). Physically, the role of the normalization condition is to transfer energy from the shape function to the phase function, so that $\vec{\phi}_{xx} \sim O(Re_\delta^{-2})$.

$$\int_0^\infty \vec{\phi}^\dagger \frac{\partial\vec{\phi}}{\partial x} dy = 0 \tag{3.22}$$

This supplementary condition prevents the use of a central scheme due to its integral form. We must therefore solve this system with a combination of numerical methods; a monolithic discretization in the normal direction and an implicit marching scheme in the streamwise direction.

3.3.2 Nonlinear forcing terms

In *Local Stability Theory* and *Linear Parabolized Stability Equations*, as the modes do not interact, we can only investigate the stability of the system for a range of individual modal perturbations [79]. In other words, only the growth rate and the shape of the perturbation vectors obtained with these methods have a physical meaning [32]. To circumvent this shortcoming and in order to extend the validity of the theory, it is possible to account for the nonlinear interactions. In the *Nonlinear Parabolized Stability Equations (NPSE)* approach, mode interactions are no longer neglected. Therefore, instead of solving every mode separately, all modes must be solved simultaneously, as they are coupled through nonlinear forcing terms. In this sense, the disturbance vector must now be expanded in terms of its truncated Fourier components. Assuming periodicity in time and in the spanwise direction, ϕ' now takes the following form:

$$\phi'(\mathbf{x}, t) = \sum_{m=-M}^{M} \sum_{n=-N}^{N} \tilde{\phi}_{m,n}(x, y) \exp i(m\beta z - n\omega t) \tag{3.23}$$

$$\tilde{\phi}(x, y) = \hat{\phi}_{m,n}(x, y) \exp\left[i \int_{x_0}^{x} \alpha_{m,n}(x) dx\right] \tag{3.24}$$

Indeed, since the NPSE accounts for the nonlinearities, the forcing terms $\mathcal{F}''$ are no longer neglected in equations (3.10a)-(3.10c). The nonlinear terms are defined as follows:

$$\begin{aligned}
\mathcal{C}'' = {} & p'T'\frac{\partial \overline{u}_i}{\partial x_i} + p'\overline{T}\frac{\partial u_i'}{\partial x_i} + \overline{p}T'\frac{\partial u_i'}{\partial x_i} + p'T'\frac{\partial u_i'}{\partial x_i} \\
& + T'\left[\frac{\partial p'}{\partial t} + \overline{u}_i\frac{\partial p'}{\partial x_i} + u_i'\frac{\partial \overline{p}}{\partial x_i} + u_i'\frac{\partial p'}{\partial x_i}\right] \\
& - p'\left[\frac{\partial T'}{\partial t} + \overline{u}_i\frac{\partial T'}{\partial x_i} + u_i'\frac{\partial \overline{T}}{\partial x_i} + u_i'\frac{\partial T'}{\partial x_i}\right]
\end{aligned} \tag{3.25}$$

$$\mathcal{M}'' = \frac{\mu'}{Re}\left[\frac{\partial^2 u'_j}{\partial x_j^2} + \frac{\partial^2 u'_j}{\partial x_i \partial x_j} - \frac{2}{3}\frac{\partial^2 u'_k}{\partial x_k^2}\delta_{ij}\right]$$
$$+ \frac{1}{Re}\frac{\partial \mu'}{\partial x_j}\left[\frac{\partial u'_i}{\partial x_j} + \frac{\partial u'_j}{\partial x_i} - \frac{2}{3}\frac{\partial u'_k}{\partial x_k}\delta_{ij}\right] \quad (3.26)$$
$$-\rho'\left[\frac{\partial u'_i}{\partial t} + \overline{u}_j\frac{\partial u'_i}{\partial x_j} + u'_j\frac{\partial \overline{u}_i}{\partial x_j}\right]$$
$$-\overline{\rho}u'_j\frac{\partial u'_i}{\partial x_j} - \rho'u'_j\frac{\partial u'_j}{\partial x_j}$$

$$\mathcal{E}'' = \frac{\lambda'}{RePr}\frac{\partial^2 T'}{\partial x_i^2} + \frac{1}{RePr}\frac{\partial \lambda'}{\partial x_i}\frac{\partial T'}{\partial x_i} + (\gamma-1)Ma^2\left(u'_i\frac{\partial p'}{\partial x_i}\right)$$
$$+ \frac{(\gamma-1)Ma^2}{Re}\left[\overline{\mu}\left(\frac{\partial u'_i}{\partial x_j} + \frac{\partial u'_j}{\partial x_i} - \frac{2}{3}\frac{\partial u'_k}{\partial x_k}\delta_{ij}\right)\frac{\partial u'_j}{\partial x_j}\right]$$
$$+ \frac{(\gamma-1)Ma^2}{Re}\left[\mu'\left(\frac{\partial u'_i}{\partial x_j} + \frac{\partial u'_j}{\partial x_i} - \frac{2}{3}\frac{\partial u'_k}{\partial x_k}\delta_{ij}\right)\frac{\partial \overline{u}_j}{\partial x_j}\right]$$
$$+ \frac{(\gamma-1)Ma^2}{Re}\left[\mu'\left(\frac{\partial \overline{u}_i}{\partial x_j} + \frac{\partial \overline{u}_j}{\partial x_i} - \frac{2}{3}\frac{\partial \overline{u}_k}{\partial x_k}\delta_{ij}\right)\frac{\partial u'_j}{\partial x_j}\right] \quad (3.27)$$
$$+ \frac{(\gamma-1)Ma^2}{Re}\left[\mu'\left(\frac{\partial u'_i}{\partial x_j} + \frac{\partial u'_j}{\partial x_i} - \frac{2}{3}\frac{\partial u'_k}{\partial x_k}\delta_{ij}\right)\frac{\partial u'_j}{\partial x_j}\right]$$
$$- \left[\rho'c_p\left(\frac{\partial T'}{\partial t} + \overline{u}_j\frac{\partial T'}{\partial x_j} + u'_j\frac{\partial \overline{T}}{\partial x_j}\right) + \overline{\rho}c_pu'_j\frac{\partial T'}{\partial x_j} + \rho'c_pu'_j\frac{\partial T'}{\partial x_j}\right]$$

The nonlinear system now reads:

$$\left\{\mathcal{L}\vec{\phi} + \mathcal{L}_y\frac{\partial\vec{\phi}}{\partial y} + \mathcal{L}_{yy}\frac{\partial^2\vec{\phi}}{\partial y^2}\right\}_{m,n} = \Lambda_{m,n}\exp\left(-i\int_x \alpha_{m,n}dx\right)\left\{\tilde{\mathbf{F}} + \mathcal{L}_x\frac{\partial\vec{\phi}}{\partial x}\right\}_{m,n} \quad (3.28)$$

The system (3.28) is mode-specific and, therefore, must be solved for every {m,n} combination. Moreover, every mode is subject to the normalization condition (3.22). Concerning the nonlinear forcing terms, they can be evaluated in physical or spectral space. The direct method expands the nonlinearities and evaluates the forcing terms using a Cauchy summation. The alternative is to use an Inverse Fast Fourier Transform (IFFT), compute

the forcing terms in the physical space using equations (3.25)-(3.27) and finally use a Fast Fourier Transform (FFT) to convert the forcing terms back into spectral space. The FFT and IFFT algorithms are well optimized, while the direct method requires the derivation and numerical evaluation of dozens of intermediate terms. Airiau even found that the FFT method was not only simpler, but also faster [2]. For these reasons, we implemented the FFT method for the forcing terms in the code.

The main advantage of integrating nonlinear effects and mode interactions within the modal analysis is that the perturbation vector, ϕ', is predicted with the correct amplitude. In other words, one can simply use an IFFT to reconstruct the perturbation ϕ' from its eigenmodes and predict the transition based on the friction coefficient evaluated from the Reynolds stresses or the turbulent kinetic energy.

3.3.3   Finite-bandwidth representation

In the classical PSE theory, the disturbance is given by (3.23) and thus each mode is represented discretely, the disturbance is thus represented by a dominant mode and its subharmonics. However, to properly represent nonlinear interactions and accurately predict the generation of frequency content, the whole frequency spectrum must be considered [91]. A novel approach, developed by Kuehl[91], is to represent the wave packet using finite bandwidth disturbances. In this approach, the perturbation vector ϕ' is defined as

$$\phi'(\mathbf{x}, t) = \int_{-\infty}^{\infty} \int_{-\infty}^{\infty} \tilde{\phi}(\omega, \beta, x, y) \exp[i(m\beta z - n\omega t)] d\omega d\beta \tag{3.29}$$

Where $\tilde{\phi}(\omega, \beta, x, y)$ is defined as

$$\tilde{\phi}(\omega, \beta, x, y) = W(\omega, \beta) \hat{\phi}_{m,n}(x, y) \exp\left[i \int_{x_0}^{x} \alpha_{m,n}(x) dx\right] \tag{3.30}$$

This explicit dependence of the shape function $\tilde{\phi}(x, y)$ on ω enables better representation of the energy transfer between the modes [100]. In practice, it is indeed impossible to represent the full spectrum of the perturbation, and thus the double integral (3.29) is

truncated and represented by equation (3.31).

$$\phi'(\mathbf{x},t) = \sum_{m=-M}^{M} \sum_{n=-N}^{N} \tilde{\phi}_{m,n}(\omega,\beta,x,y) \exp i(m\beta z - n\omega t)\Delta\omega\Delta\beta \qquad (3.31)$$

Similarly, certain terms can be grouped to lead to a perturbation formulation similar to that of (3.23):

$$\phi'(\mathbf{x},t) = \sum_{m=-M}^{M} \sum_{n=-N}^{N} \underbrace{\tilde{\phi}_{m,n}(x,y) \exp i(m\beta z - n\omega t)}_{\text{from Equation (3.23)}} \underbrace{W(\beta,\omega)\Delta\omega\Delta\beta}_{\tilde{W}(\omega,\beta)} \qquad (3.32)$$
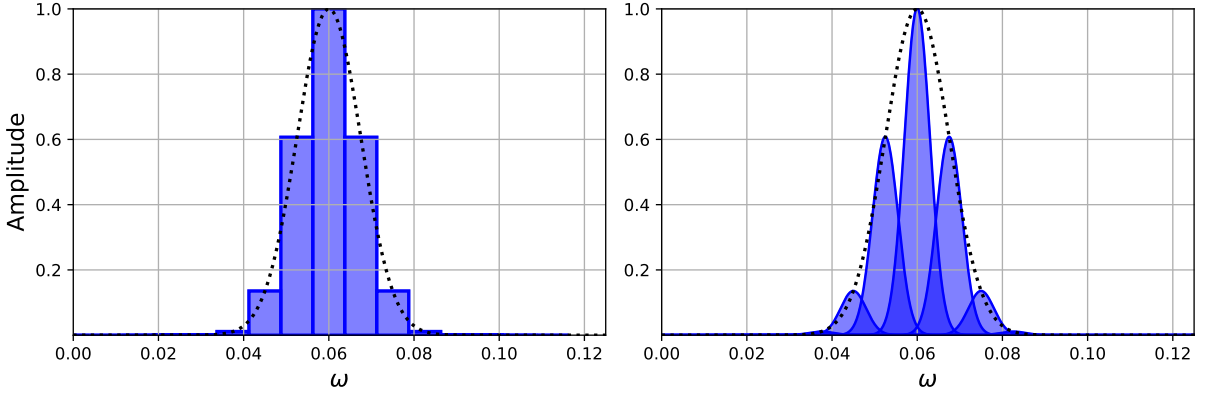
FIGURE 3.1. Illustration of the finite-bandwidth representation. The dotted line represents the frequency content of the perturbation. Each bar and gaussian function represent the modes solved in the PSE using the *delta* (left) and *normal* (right) mode shape.

The main advantage of this formulation is that it allows for modeling of finite-bandwidth disturbances. For example, a spectral shape function $\tilde{W}$ can be defined for each mode of disturbance, and acts as a transfer function that redistributes energy between modes. By defining W using the delta Dirac function $W = \delta(\omega) \cdot \delta(\beta)$, it is possible to retrieve the classical wave-packet approach. In the finite-bandwidth approach, $\tilde{W}$ can take any form, as long as the energy is conserved, that is, the energy contained in each mode must remain the same. The obvious choice for W in the context of the finite-bandwidth approach is

27

a normal distribution. Figure 3.1 illustrates the difference between the *delta* and *normal* finite-bandwidth representations. In Figure 3.1, the disturbance is only discretized in ω, but the concept is easily generalizable to include both ω and β. Slight overlaps between modes enhance the study of spectral broadening and low-frequency content generation [91]. On the algorithmic side, the main difference in the implementation is an additional loop over the modes in the computation of the amplitude, as each mode now slightly contributes to the growth of the other modes.

3.3.4 Measure of stability

The disturbance growth rate σ is calculated from α (streamwise wavenumber) and E_k (disturbance kinetic energy) with equation (3.33). The first term, $-Im(\alpha)$, corresponds to the contribution of the exponential part of the disturbances, while the second term is the correction related to the change in the amplitude function [86].

$$\sigma = -Im(\alpha) + \frac{\partial}{\partial x}\left[\ln\left(\sqrt{E_k}\right)\right] \tag{3.33}$$

$$E_k = \int_0^\infty \overline{\rho}\left(|\hat{u}|^2 + |\hat{v}|^2 + |\hat{w}|^2\right) dy \tag{3.34}$$

When $\sigma > 0$, the disturbances are amplified, when $\sigma < 0$ they are damped. Figure 3.2 shows the evolution of the growth rate along the x-direction. The results are compared with Juniper's (incompressible) results for a ZPG flat plate [86].

The neutral stability curve provides valuable information on the stability of the flow under given conditions (Re_δ, ω, β, Ma). The neutral stability curve is obtained by performing multiple PSE simulations over a range of ω and β. In incompressible boundary layer flows, the most unstable mode is two-dimensional, and thus it is common practice to simply set $\beta = 0$ and investigate the spatial evolution of α by varying the temporal frequency (ω). As seen in the Figure 3.3, the PSE results agree well with the experimental data, except for the height of the teardrop peak. However, the PSE results are almost perfectly in agreement with the previous DNS predictions. The disparities between the experiments and the DNS/PSE results are probably due to the experimental setups themselves: background

28
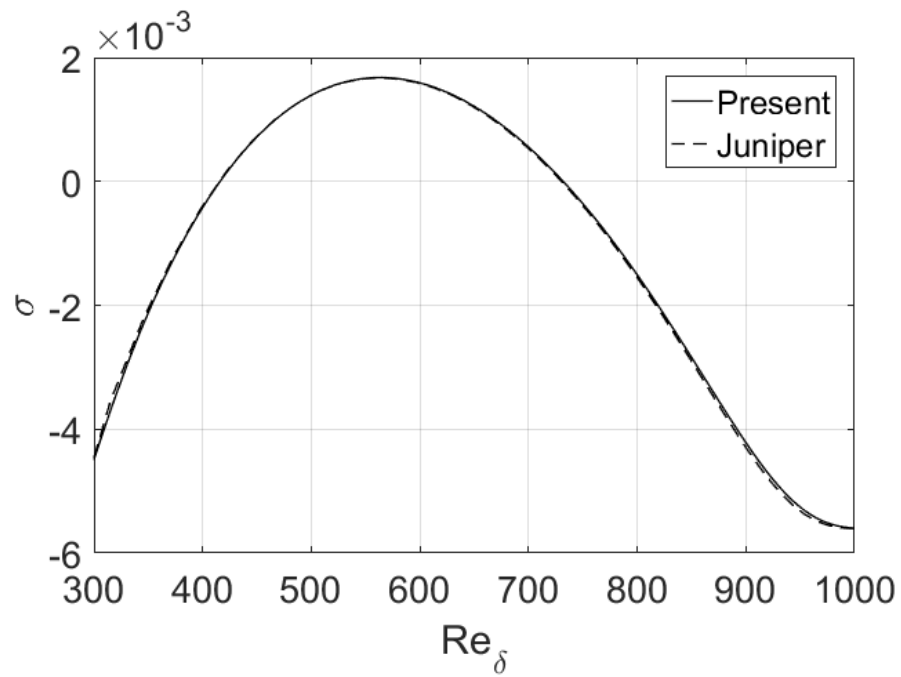
FIGURE 3.2. Comparison of the growth rate in a laminar boundary layer obtained with the LPSE approach at Mach 0.1 ($F = 100$), compared with incompressible results from [86]
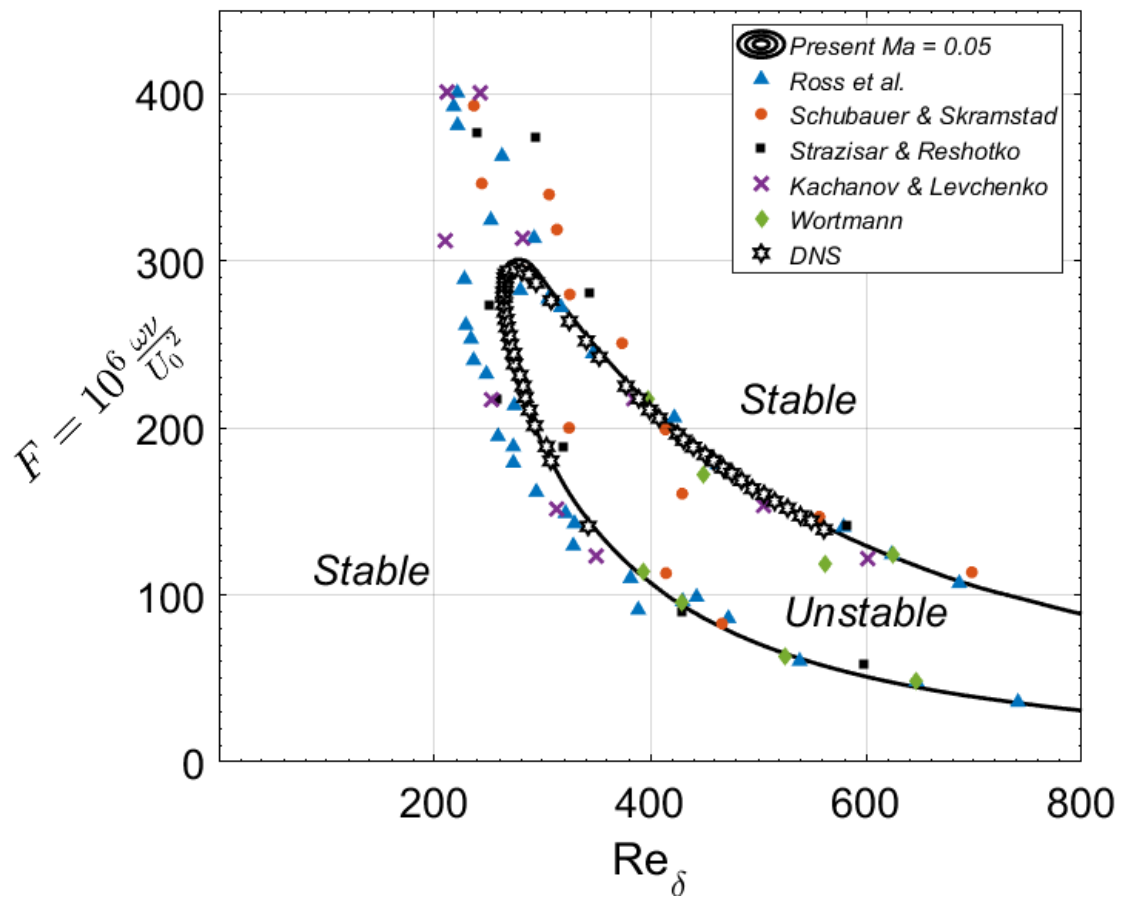
FIGURE 3.3. (a) Neutral stability curve, $Ma = 0.05$ ZPG flat plate

noise, wall vibration, and/or surface roughness may induce perturbation in the freestream and extend the zone of instability further than the idealized DNS/PSE case.

3.3.5   N-factor

The e^N method is widely used in aerodynamic design. Based on empirical measurements, industry has made huge efforts to collect the experimental data needed for transition correlations [72]. The n-factor can be seen as a measure of the amplification of a particular mode along the stream path. However, it should be noted that the n-factor is a function of the temporal and spanwise wavenumbers (ω and β); every combination of wavenumbers has a corresponding n-factor curve that cannot be directly correlated with the transition position.

$$\text{n-factor} = -\int_{x_0}^{x_i} \sigma dx \tag{3.35}$$

To remove this ambiguity, Ingen [80], [81] defined the *N-factor*, with a capitalized letter, corresponding to the envelope of the n-factor curves (see Figure 3.4).

From a physical point of view, the e^N method is nothing more than a correlation between the transition position (obtained experimentally) and the N-factor (obtained with the modal stability theory). The method is thus highly data-driven and specific to the geometry of the experiment: a critical N-factor must be correlated for every geometry and flow condition. The use of the method beyond its range of applicability may lead to considerable errors. For the Blasius boundary layer, Ingen [81] reached the following critical N-factors for the beginning and end of the transition.

$$N_B = 2.13 - 6.18 \log_{10}(Tu) \tag{3.36}$$

$$N_E = 5.00 - 6.18 \log_{10}(Tu) \tag{3.37}$$

where Tu represents the freestream turbulence intensity. The relations (3.36) and (3.37) are based on the experiments of Schubauer and Skramstad [170] and are valid for $Tu > 0.1\%$. Combining the relations (3.36) and (3.37) and the results plotted on the Figure 3.4a, one can obtain an estimate of the location of the transition. Figure 3.4b shows the prediction of the transition location for an incompressible zero pressure gradient (ZPG) flat plate
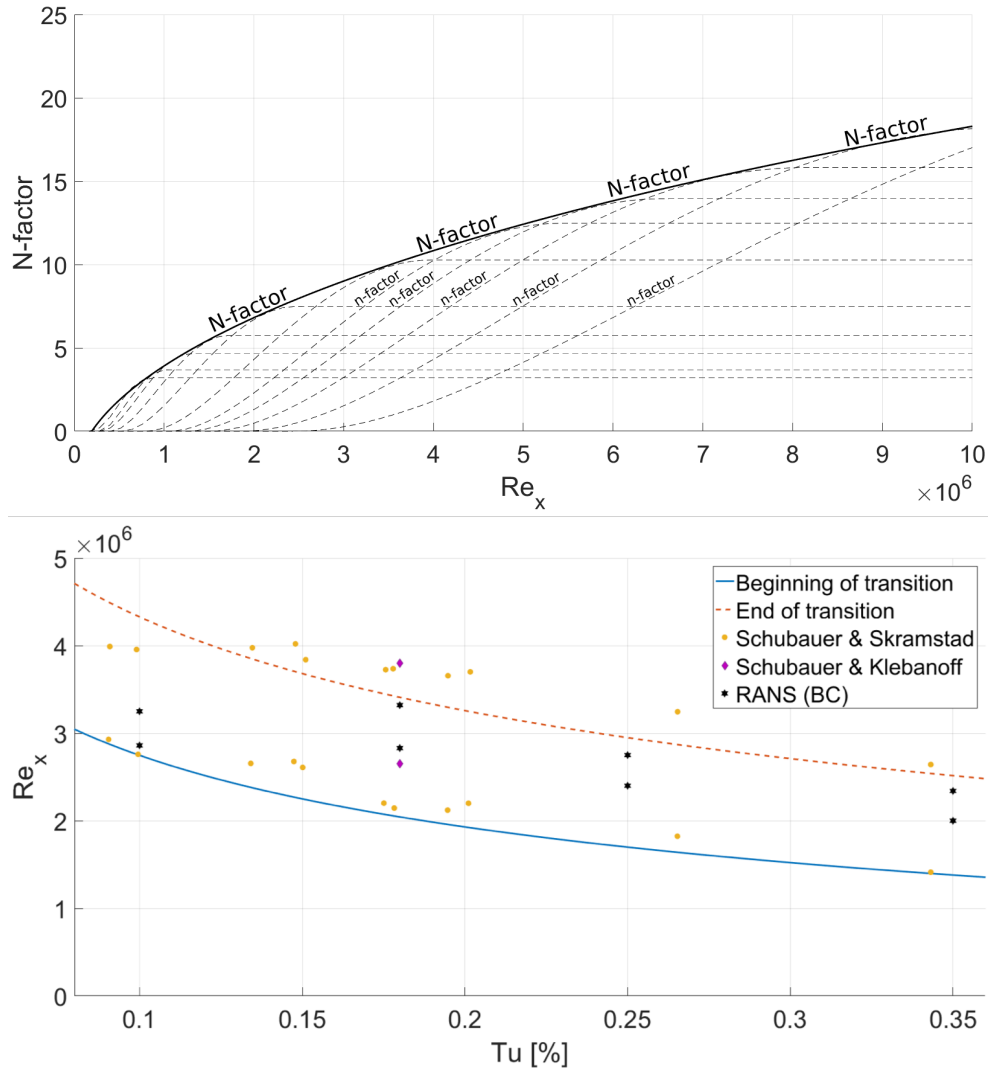
FIGURE 3.4. (top) N-factor versus n-factor, (bottom) PSE predictions of the beginning and end of transition as a function of the turbulence intensity (Tu [%]), $Ma = 0.1$ ZPG flat plate
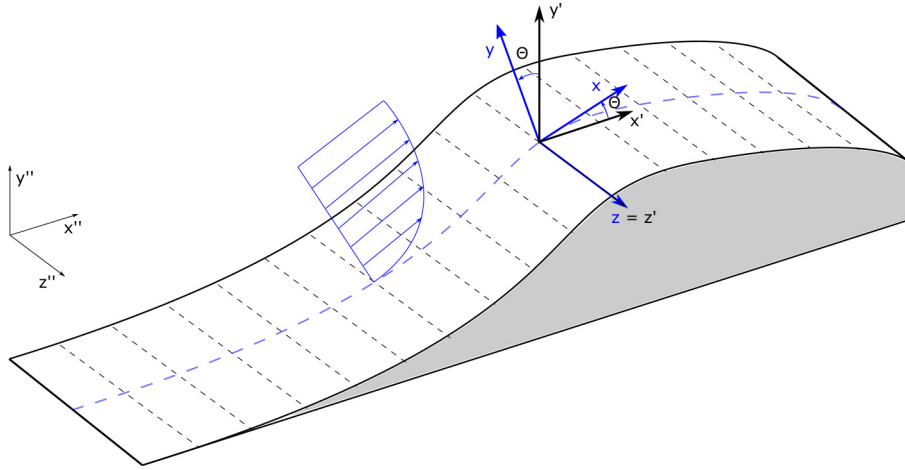
FIGURE 3.5. Illustration of the ortho-curvilinear coordinate system

boundary layer. The RANS, using the $k - \omega$ model supplemented with the 2 equations $\gamma - Re_\theta$ transition model, and the e^N method lead to similar results for the *End of transition line*, which is expected since both approaches have been optimized for this exact test case (ZPG transitional flat plate boundary layer).

3.4 Parabolized stability equation framework

3.4.1 Curvilinear coordinates

One of the main objectives of the research is to develop a tool to predict the transition in compressible flows over complex geometries. The marching procedure is performed in the streamwise direction and is therefore incompatible with general Cartesian coordinates, except in the case where x is perfectly aligned with the streamlines (which is the case for very simple flows such as Blasius, Poiseuille and Couette flows). To overcome this difficulty, we define the following orthocurvilinear coordinate system as illustrated in Figure 3.5. For conciseness, the Cartesian and the translated Cartesian systems are referred to by the superscripts $''$ and $'$, respectively, while the ortho-curvilinear system is simply noted $\{x, y, z\}$, without any superscript.

$$x = x' \cos(\theta(x)) - y' \sin(\theta(x)) \tag{3.38}$$

$$y = x' \sin(\theta(x)) + y' \cos(\theta(x)) \tag{3.39}$$

$$z = z' \tag{3.40}$$

The geometric Jacobian associated with equations (3.38) -(3.40) can be written in matrix form:

$$\mathbf{J} = \begin{bmatrix} \frac{\partial x}{\partial x'} & \frac{\partial x}{\partial y'} & 0 \\ \frac{\partial y}{\partial x'} & \frac{\partial y}{\partial y'} & 0 \\ 0 & 0 & 1 \end{bmatrix} \tag{3.41}$$

where the coefficients are given by:

$$\frac{\partial x}{\partial x'} = \frac{\cos\theta}{1 + y\frac{d\theta}{dx}} \qquad = J_{xx} \qquad \frac{\partial x}{\partial y'} = -\frac{\sin\theta}{1 + y\frac{d\theta}{dx}} \qquad = J_{yx} \tag{3.42}$$

$$\frac{\partial y}{\partial x'} = \sin\theta + x\frac{d\theta}{dx}\frac{\partial x}{\partial x'} \qquad = J_{xy} \qquad \frac{\partial y}{\partial y'} = \cos\theta + x\frac{d\theta}{dx}\frac{\partial x}{\partial y'} \qquad = J_{yy} \tag{3.43}$$

Using the chain rule, the Cartesian derivatives of a scalar function F can be expressed in the curvilinear coordinate system using equations (3.44)-(3.48).

$$\frac{\partial F}{\partial x'} = \frac{\partial F}{\partial x}J_{xx} + \frac{\partial F}{\partial y}J_{yx} \tag{3.44}$$

$$\frac{\partial F}{\partial y'} = \frac{\partial F}{\partial x}J_{xy} + \frac{\partial F}{\partial y}J_{yy} \tag{3.45}$$

$$\frac{\partial^2 F}{\partial x'^2} = \frac{\partial^2 F}{\partial x^2}J_{xx}^2 + \frac{\partial^2 F}{\partial x \partial y}2J_{yx}J_{xx} + \frac{\partial^2 F}{\partial y^2}J_{yx}^2 \tag{3.46}$$

$$\frac{\partial^2 F}{\partial y'^2} = \frac{\partial^2 F}{\partial x^2}J_{xy}^2 + \frac{\partial^2 F}{\partial x \partial y}2J_{xy}J_{yy} + \frac{\partial^2 F}{\partial y^2}J_{yy}^2 \tag{3.47}$$

$$\frac{\partial^2 F}{\partial x' \partial y'} = \frac{\partial^2 F}{\partial x^2}J_{xx}J_{xy} + \frac{\partial^2 F}{\partial x \partial y}\left(J_{yy}J_{xx} + J_{yx}J_{xy}\right) + \frac{\partial^2 F}{\partial y^2}J_{yx}J_{xy} \tag{3.48}$$

The complete compressible Navier-Stokes equations as well as the modal stability equations in curvilinear coordinates can be found in the appendix.

The geometric Jacobian is only defined for the normal and tangential directions. The details of the numerical implementation of the modal stability equations as well as the

34

compressible Navier-Stokes equations are addressed in the next section.

3.4.2   Numerical Methods

One of the main advantages of the parabolized stability equations is their ability to be solved using a computationally advantageous marching procedure. This approach allows for the use of two different numerical methods in the streamwise and normal directions. For instance, we use a multi-element spectral collocation method in the normal direction and Backward Differentiation Formulas (BDF) in the streamwise direction. This approach was also preferred by several other authors [71, 117, 146].

Wall-normal discretization

The spectral collocation method is an accurate class of numerical techniques for the solution of linear/nonlinear partial differential equations (PDE). The main idea behind the spectral collocation method is to expand the solution in terms of global basis functions so that the numerical solution satisfies the PDE at the so-called *collocation points*, or *Chebyshev Gauss-Lobatto points*[78],

$$\xi_j = \cos \frac{\pi j}{n} \qquad\qquad \xi_j \in [-1, 1] \qquad\qquad (3.49)$$

The general spectral representation of a solution to a PDE takes the following form:

$$u^*(\xi) = \sum_{j=0}^{n} \phi_j(\xi) u(\xi_j) \qquad\qquad (3.50)$$

where $\phi_j(\xi)$ are the basis functions. In the case of modal stability theory, since the solution is not periodic, we use Chebyshev polynomials of the following form:

$$\phi_j(\xi) = \left(\frac{1 - \xi_j^2}{\xi - \xi_j} \right) \frac{T_n'(\xi)}{n^2 c_j} (-1)^{j+1}; \qquad c_0 = c_n = 2, \ c_j = 1 \qquad (3.51)$$

35

where T_n and T_n' are the Chebyshev polynomials

$$T_n(\xi) = \cos(n \cos^{-1} \xi) \tag{3.52}$$

$$T_n'(\xi) = \frac{n \sin(n \cos^{-1} \xi)}{\sqrt{1 - \xi^2}} \tag{3.53}$$

The derivatives of the Chebyshev polynomials can be computed from the following expression:

$$\left. \frac{du^*}{d\xi} \right|_i = \sum_{j=0}^{n} \Phi_{ij}(\xi) u(\xi_j) \tag{3.54}$$

where

$$\Phi_{ij} = \frac{c_i}{c_j} \frac{(-1)^{i+j}}{\xi_i - \xi_j}, \text{for } i \neq j \tag{3.55}$$

$$\Phi_{ii} = -\frac{\xi_i}{2(1 - \xi_i^2)} \tag{3.56}$$

$$\Phi_{00} = \frac{2m^2 + 1}{6} \tag{3.57}$$

$$\Phi_{nn} = -\frac{2m^2 + 1}{6} \tag{3.58}$$

The collocation points ξ_j are defined on a domain from $[-1, 1]$. To compute the derivative on the physical domain $y_j \in [y_0, y_f]$, a scaling function, S_i, must be applied.

$$\left. \frac{du^*}{dy} \right|_i = \left. \frac{du^*}{d\xi} \frac{d\xi}{dy} \right|_i = \sum_{j=0}^{n} S_i \Phi_{ij} u(\xi_j) = \sum_{j=0}^{n} D_{ij} u(y_j) \tag{3.59}$$

Higher derivatives are defined through the powers of the matrix D. For example, the second derivative is D^2, the third is D^3, and so forth [196]. For example,

$$\left. \frac{d^2 u^*}{dy^2} \right|_i = \sum_{j=0}^{n} D_{ik} D_{kj} u(y_j) \tag{3.60}$$

Finally, the solution and its derivatives can be represented in a more convenient matrix-vector form:

$$\mathbf{u}^* = \mathbf{I} \cdot \mathbf{u} \qquad\qquad \frac{d\mathbf{u}^*}{dy} = \mathbf{D} \cdot \mathbf{u} \qquad\qquad \frac{d^2\mathbf{u}^*}{dy^2} = \mathbf{D}^2 \cdot \mathbf{u} \qquad (3.61)$$

Multi-Domains Spectral collocation method

Due to its exponential convergence rate, the spectral collocation method is one of the most accurate and efficient numerical schemes. However, in practice, the collocation points are not necessarily well distributed for the shape of the solution. To deal with this problem, we can increase the degree of the polynomial to within the range of 200-300, which usually leads to numerical instabilities. Moreover, the classical spectral collocation method requires the resolution of a dense matrix, which can be a problem for computational performance optimization. The use of a multi-domain spectral collocation approach helps alleviate these issues by converting the system matrix into a sparse matrix and allowing the user to define a *less stringent* grid spacing. This approach was first used in the context of the PSE by Malik [117] The general idea behind this approach is to divide the computational domain into multiple subdomains and apply the classical spectral collocation method locally, on every *element*. Appropriate boundary conditions at the interfaces of the elements ensure the smoothness of the solution. Thus, it is possible to define a global differentiation matrix $\mathcal{D}$, composed of multiple sub-differentiation matrices. For example, for 3 subdomains $\mathcal{D}$ is defined as

$$\mathcal{D} = \begin{bmatrix} \mathbf{D}_0 & 0 & 0 \\ 0 & \mathbf{D}_1 & 0 \\ 0 & 0 & \mathbf{D}_2 \end{bmatrix} \qquad (3.62)$$

To better illustrate this feature, a typical mesh for a forward facing step (FFS) is shown in Figure 3.6. The irregular clustering is due to the spectral multi-element collocation method. The first interface is visible near $y = 5\delta$. Each element uses a polynomial of degree 48. The main advantage of the multi-elements spectral collocation method is that

37

one can choose the location of each element in order to ensure a minimum number of points in the boundary layer.
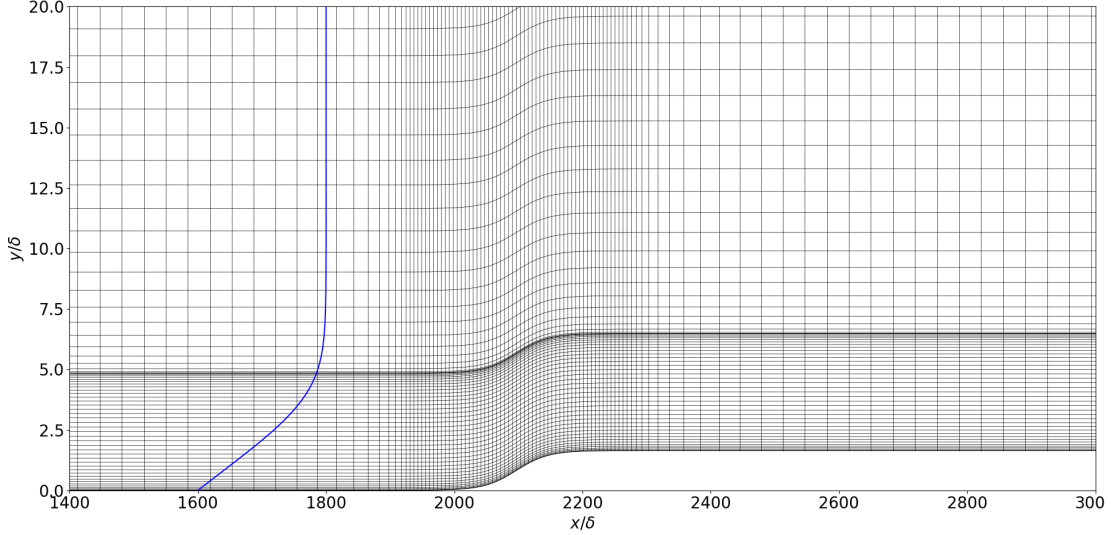
FIGURE 3.6. A typical mesh for the forward facing step case (FFS), only a small portion of the domain is displayed. The U-velocity profile is displayed in blue for scaling

Stream-wise discretization

Due to the elliptic nature of the steady-state Navier-Stokes equations, the laminar base flow solver requires the use of an implicit (central) numerical scheme. To this end, we use a high-order central finite-difference scheme. The coefficients are deduced from the Lagrange polynomials, which allow the use of non-uniform grids and polynomials of arbitrary degree.

$$L(x_i) = \sum_{j=0}^{k} y_j \ell_j(x_i) \qquad\qquad \ell_j(x_i) = \prod_{\substack{0 \le m \le k \\ m \ne j}} \frac{x_i - x_m}{x_j - x_m} \qquad (3.63)$$

In practice, the finite difference coefficients are obtained by evaluating the derivative of the Lagrange polynomials at the grid points using equation (3.64). The higher derivatives

38

are obtained through recursion.

$$L^{'}(x) := \sum_{j=0}^{k} y_j \ell_j^{'}(x) \qquad \ell_j^{(1)}(x) := \sum_{\substack{i=0 \\ i \neq j}}^{k} \left[\frac{1}{x_j - x_i} \prod_{\substack{m=0 \\ m \neq (i,j)}}^{k} \frac{x - x_m}{x_j - x_m} \right] \qquad (3.64)$$

We noticed that the multi-element method induced small oscillations in the solution of the base flow, which were susceptible to tarnish the modal response of the flow. In order to keep the robustness and accuracy of the modal solver, we decided to use a pure finite difference approach for the *base flow*, but keep an hybrid spectral/BDF approach for the fluctuating flow as it is the most accurate and robust method for the stability solver. As a result, the base flow is solved using a different grid spacing in the normal direction; this means that the solution must be interpolated at the spectral collocation points using (3.63).

The PSE are solved using an implicit spatial-marching procedure. For this purpose, we chose standard Backward Differentiation Formulas (BDF). The BDF coefficients are computed with (3.64) using the points upwind of the query point, allowing the use of a variable step size. To avoid numerical instabilities in the marching procedure when the step size is reduced, Krypton uses the stabilization technique proposed by [6]. In Krypton, the BDF order is arbitrary, but the stabilization term is only valid for first-order BDF.

3.4.3 Algorithm

In this section, we provide a brief overview of the code architecture, its main algorithms, and provide an overview of the approaches used to discretize the governing equations.

Architecture

The program, Krypton, was developed with a strong emphasis on modularity and flexibility, as it is the main framework for the current research. The paper describing the

overview of the code implementation and usage is presented in the next chapter. Most of the code is written in Python to take advantage of the numerous scientific computing packages (NumPy, SciPy, Matplotlib). The vast majority of NumPy and SciPy functions are, in fact, wrappers for lower-level functions and solvers, such as those contained in the BLAS, LAPACK and Pardiso libraries. By default, the Anaconda distribution of Python is compiled with the Intel *Math Kernel Library* (MKL), a highly optimized, threaded, and vectorized library. In this way, we take advantage of a high-level programming language (speed of development, flexibility, simplicity), as well as some advantages of mid-level languages (efficiency, threading, rapidity). It is important to point out that Krypton was developed from scratch; everything from the numerical methods (which include the multi-elements spectral collocation method, the finite difference scheme, and the BDF-based marching procedure) to the flow solver (which include the compressible laminar Navier-Stokes and the modal stability solver) were developed by the author, for the need of the current research. Krypton was developed using an Object Oriented Programming (OOP) philosophy; its architecture is described in the present section.

How it works

The figures 3.7 and 3.8 illustrate how the different modules communicate together within Krypton. First, all the input of the simulation, including the flow properties (Re, Ma, T_w, ω, β, crossflow intensity), and the specification of the numerical methods (BDF order, discretization, geometry) are specified in the main.py module. These inputs are then passed to the Discret.py module, which is used to compute the relevant differentiation matrices (spectral collocation in y and FD/BDF in x). The Discret.py module also includes different classes and methods for multidimensional interpolation and numerical integration that were developed directly from the basis functions to ensure consistency with the numerical schemes.

Base flow: Laminar Compressible Navier-Stokes Solver

The next step is to generate the base flow. For this purpose, the module LaminarFlow.py first creates an object associated with the discretized Navier-Stokes equations. This ob-

ject, defined in NS.py, contains all the relevant methods to build the linear operator and iteratively solve the problem. The CNSE are solved using a Picard iterative method –also referred to as the fixed-point algorithm. In the Picard method, the non-linear terms are linearized with the solution at the previous step (k-1). For instance, the convective terms in the momentum equation are defined as

$$u_j^k \frac{\partial u_i^k}{\partial x_j} \approx u_j^{k-1} \frac{\partial u_j^k}{\partial x_j} \tag{3.65}$$

The Picard method is relatively simple and easy to implement but has only a linear convergence. The present algorithm usually takes around 8 iterations to converge for the computation of a simple zero pressure gradient (ZPG) flat plate simulation and has a time complexity of $O(n^{1.2})$, which means that if the number of equations is doubled, the computation time will increase by a factor $2^{1.2}$.

For the boundary condition, we impose a unitary velocity at the inlet while the pressure is extrapolated from the solution. We impose a traction-free boundary condition, given by equation (3.66), in the free-stream. The pressure is imposed at the outlet. In most cases, the temperature of the wall is kept constant ($\frac{T_w}{T_0} = \frac{T_w}{T_\infty} = 1$).

$$\frac{\mu}{Re} \left[\left(\frac{\partial u_i}{\partial x_j} + \frac{\partial u_j}{\partial x_i} \right) - \frac{2}{3} \frac{\partial u_k}{\partial x_k} \delta_{ij} \right] - p\delta_{ij} = 0 \tag{3.66}$$

Fluctuating flow : Modal Stability Solver

Once the tolerance on the residual is met, the solution derivatives are calculated and the base flow is transferred to the modal stability solver. The modal stability solver is, by construction, very similar to the laminar flow solver, the main difference lies in the definition of the object associated with the PSE. First, since the equations are parabolized, the problem is essentially divided into several smaller problems that will be solved sequentially through a marching procedure. Both the local (LST) and the nonlocal (LPSE) procedure are implemented in the PSE.py module, since they roughly only differ from each other by the addition of streamwise derivatives and a different convergence criteria. The local

main.py

Input conditions
- Ma, Re, Tw
- Geometry
- Wave numbers

Numerical Methods (Discret.py)

Compute differentiation matrices
- Spectral collocation
- Finite difference
- Backward differentiation formula (BDF)

Computing Base Flow (LaminarFlow.py)

Compressible Navier-Stokes Equations (NS.py)

Initialize solution
U, T = 1
V, W = 0
P = P_0

Build Linear Operator
[LHS] = f(ϕ^{n-1})

Solve System
[LHS]ϕ^n = [RHS]

Update solution

$| \phi^n - \phi^{n-1} | >$ tol

$|\phi^n - \phi^{n-1}| <$ tol

Output Base Flow
ϕ

FIGURE 3.7. Krypton block diagram (part 1 of 2)

stability problem is generally solved as a matrix eigenvalue problem [207, 86]:

$$[A]\Phi = \omega[B]\Phi \tag{3.67}$$

In such a case, the system can be solved with classical numerical methods, for instance, the standard QZ algorithm or inverse Rayleigh iterations. However, these methods are computationally expensive and often lead to inaccurate results. Instead, we chose to follow a simpler and more robust algorithm: rather than finding ω such that (3.67) is satisfied, we impose ω and find α such that the following boundary conditions are satisfied on the shape functions:

$$\hat{u}(0) = \hat{v}(0) = \hat{w}(0) = \hat{T}(0) = \hat{p}(0) - 1 = 0 \tag{3.68}$$

$$\hat{u}_y(\infty) = \hat{v}_y(\infty) = \hat{w}_y(\infty) = \hat{T}_y(\infty) = \hat{p}_y(\infty) = 0 \tag{3.69}$$

To do so, we impose the boundary conditions on all variables except $\hat{v}$ at the wall and iterate on α using the Newton-Raphson method until $|\hat{v}(0)| < \epsilon$. We usually set ϵ to somethin slightly larger than machine precision in our calculations. This approach is robust, lightweight, and converges quadratically. The results obtained from the local stability theory are then used as initial conditions for the PSE calculation.

The procedure for the PSE calculations is almost identical to the LST algorithm; there are only slight procedural differences. First, the boundary conditions are slightly different: $\hat{v}(0)$ is now explicitly set to zero, while the condition on $\hat{p}$ at the wall is relaxed. In the PSE approach, the normalization condition replaces the condition on $\hat{v}$ at the wall in Newton's iterations, and thus the new objective is to find α for which the condition (3.22) is satisfied. Once the solution is converged at the first station, the marching procedure begins. For this purpose, we opt for an implicit BDF-based approach. We define a station as a position on the x-axis.

The nonlinear algorithm is a bit more complicated, as it requires the use of two nested loops to ensure the convergence of the solution. In other words, the new objective is to find α that satisfies condition (3.22) for a given forcing term. The forcing terms are therefore updated once α is converged for all the modes. In general, each iteration requires 2 to 3

FlucFlow.py

Local Stability Theory (PSE.py)

Initialize
$\alpha_0 = 0.36\omega$

Build Linear Operator
[LHS] $= f(\alpha_0, \phi)$

set B.C.
$\hat{u}(0) = \hat{T} = \hat{w} = 0$
$\hat{v}(0) = free$
$\hat{p} = 1$

Solve System
[LHS] $\hat{\phi} = 0$

Update α_0

$\hat{v}(0) > 1e\text{-}15$

$\hat{v}(0) < 1e\text{-}15$

Output Fluctuating Flow
$\hat{\phi}_0$

Nonlocal Stability Theory (PSE.py)

Initialize
$\alpha_i = \alpha_{i-1}$

Build Linear Operator
[LHS] $= f(\alpha, \phi_i)$

set B.C.
$\hat{u}(0) = \hat{v}(0) = \hat{T}(0) = \hat{w}(0) = 0$
$\hat{p}(0) = free$

Compute
[RHS] $= f(\partial_x \hat{\phi}_i^n)$

Solve System
[LHS] $\hat{\phi}_i^n$ = [RHS]

Update α_i

$\int_0^\infty \hat{\phi}^c \partial_x \hat{\phi} dy < tol$

$\int_0^\infty \hat{\phi}^c \partial_x \hat{\phi} dy < tol$

i = i+1
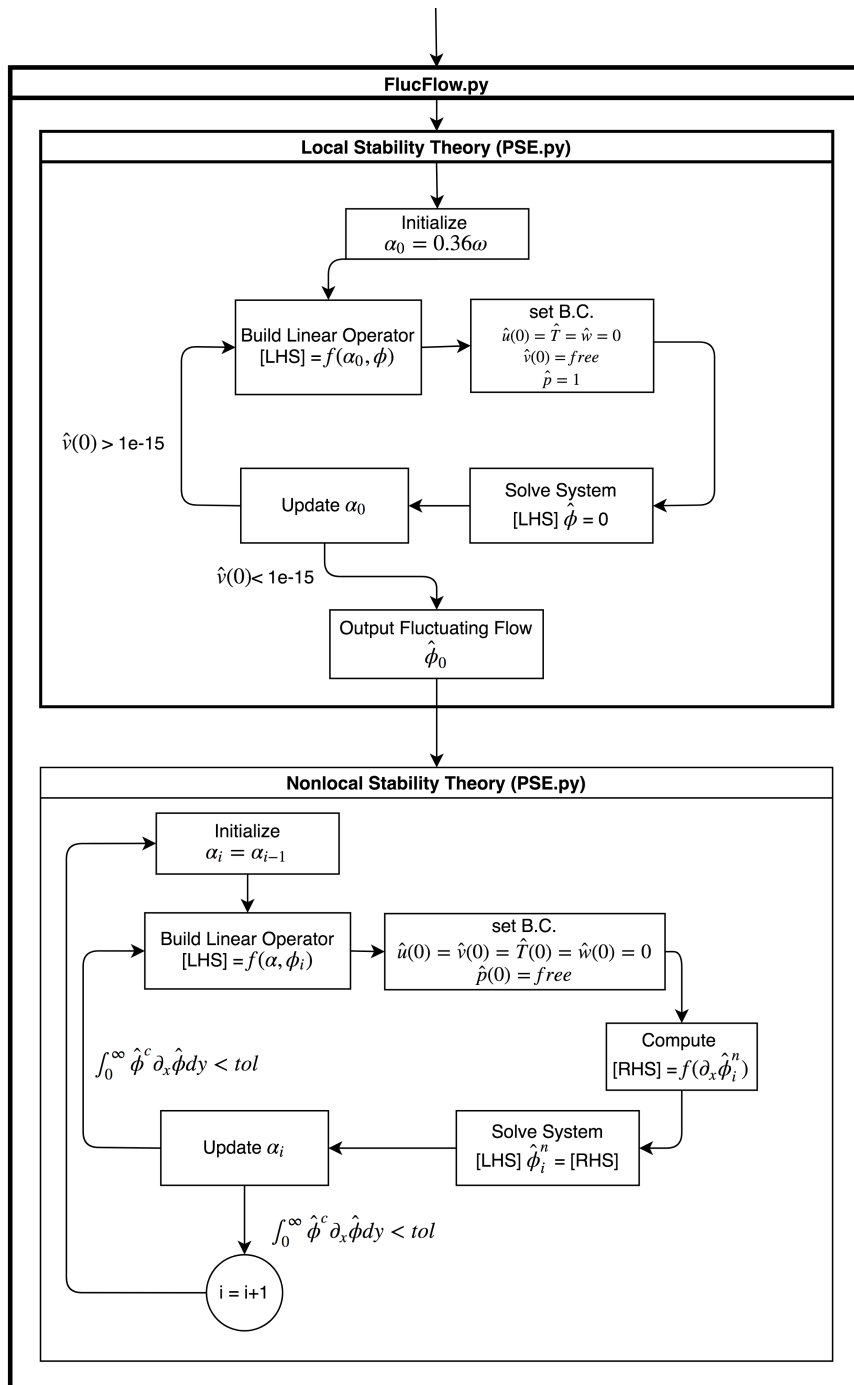
FIGURE 3.8. Krypton block diagram (part 2 of 2)

44

sub-iterations to converge.

3.5   Direct Numerical Simulations

The direct numerical simulation of compressible boundary layer flow in complex geometries with realistic Reynolds numbers requires the use of highly resolved grids in addition to high-order numerical methods–generally the mesh resolution for DNS falls in range of 100M to 10B grid points. At such grid resolution, the question of scalability becomes crucial. Most commercial software typically favours stability over high-order numerical methods, and are ill-suited for DNS studies of transitional flows or turbulence. The main reason for this is the same reason that CFD was once limited to academia: DNS in its current state is tractable only for simple, idealized problems. On the academic side, the obvious open source options are OpenFoam and Nektar++. While these softwares have DNS –or quasi-DNS–capabilities and support arbitrary complex geometries, they also use unstructured grids and/or implicit time integration, which is not adapted for the need of the current research. Through long-standing collaboration, we have access to Hybrid, an academic DNS code developed by Johan Larsson (University of Maryland) and Ivan Bermejo-Moreno (USC) [12]. Hybrid is a massively parallelized code that uses a sixth-order central finite-difference scheme coupled with high-order filtering for the spatial derivatives and a fourth-order Runge-Kutta scheme for the time integration. At the fluid boundaries, an NSCBC (Navier-Stokes Characteristic Boundary Condition) is enforced and is supplemented by a sponge layer to dampen spurious oscillations of the finite computational domain. The baseline code has been extensively used for shock turbulence interaction and wall-bounded flow studies. Hybrid, however, uses Cartesian coordinates, and thus in order to study the effect of smooth roughness on the boundary layer stability, we had to implement curvilinear coordinates. The mere implementation of curvilinear coordinates in such a high-performance DNS code represents a substantial contribution that requires special precautions to preserve the code efficiency and scalability. In this section, we summarize the main steps to derived the N-S equations in curvilinear coordinates and discuss the main implementation strategies into Hybrid.

3.5.1 Governing equations

In the current section, the change of coordinates system is made following the method described by [124]. Hybrid solves the compressible Navier-Stokes equations in conservative form for a calorically perfect gas in Cartesian coordinates:

$$\frac{\partial \rho}{\partial t} + \frac{\partial \rho u_i}{\partial x_i} = 0 \tag{3.70}$$

$$\frac{\partial \rho u_i}{\partial t} + \frac{\partial}{\partial x_j}\left(\rho u_i u_j + p\delta_{ij}\right) = \frac{\partial \sigma_{ij}}{\partial x_j} \tag{3.71}$$

$$\frac{\partial E}{\partial t} + \frac{\partial}{\partial x_j}\left(u_j(E + p)\right) = \frac{\partial}{\partial x_j}\left(u_i \sigma_{ij} - \kappa \frac{\partial T}{\partial x_j}\right) \tag{3.72}$$

where E corresponds to the sum of the internal and kinetic energy of the fluid. The equations are appropriately and consistently non-dimensionalized, the details of which can be found in the thesis of Daryan [126].

3.5.2 Coordinate transformation

The idea of a coordinate transformation is to uniquely map a rectangular mesh onto a body of arbitrary shape. Here we use the following notation:

Forward transformation	Backward transformation	
$x_1 = x_1(\xi_1, \xi_2, \xi_3)$	$\xi_1 = \xi_1(x_1, x_2, x_3)$	(3.73)
$x_2 = x_2(\xi_1, \xi_2, \xi_3)$	$\xi_2 = \xi_2(x_1, x_2, x_3)$	(3.74)
$x_3 = x_3(\xi_1, \xi_2, \xi_3)$	$\xi_3 = \xi_3(x_1, x_2, x_3)$	(3.75)

where x_i and ξ_i are the coordinates in Cartesian and curvilinear coordinates, respectively. In general, the forward transformation can be written explicitly using a functional relation; the backward transformation is usually more difficult to define due to its implicit relationship to x_i. The derivative of an arbitrary scalar function ϕ in Cartesian coordinates is

defined by

$$\frac{\partial \phi}{\partial x_1} = \frac{\partial \phi}{\partial \xi_1}\frac{\partial \xi_1}{\partial x_1} + \frac{\partial \phi}{\partial \xi_2}\frac{\partial \xi_2}{\partial x_1} + \frac{\partial \phi}{\partial \xi_3}\frac{\partial \xi_3}{\partial x_1} \tag{3.76}$$

$$\frac{\partial \phi}{\partial x_2} = \frac{\partial \phi}{\partial \xi_1}\frac{\partial \xi_1}{\partial x_2} + \frac{\partial \phi}{\partial \xi_2}\frac{\partial \xi_2}{\partial x_2} + \frac{\partial \phi}{\partial \xi_3}\frac{\partial \xi_3}{\partial x_2} \tag{3.77}$$

$$\frac{\partial \phi}{\partial x_3} = \frac{\partial \phi}{\partial \xi_1}\frac{\partial \xi_1}{\partial x_3} + \frac{\partial \phi}{\partial \xi_2}\frac{\partial \xi_2}{\partial x_3} + \frac{\partial \phi}{\partial \xi_3}\frac{\partial \xi_3}{\partial x_3} \tag{3.78}$$

In matrix form, the **Jacobian of the backward transformation** reads:

$$\begin{bmatrix} \frac{\partial \phi}{\partial x_1} \\ \frac{\partial \phi}{\partial x_2} \\ \frac{\partial \phi}{\partial x_3} \end{bmatrix} = \begin{bmatrix} \frac{\partial \xi_1}{\partial x_1} & \frac{\partial \xi_2}{\partial x_1} & \frac{\partial \xi_3}{\partial x_1} \\ \frac{\partial \xi_1}{\partial x_2} & \frac{\partial \xi_2}{\partial x_2} & \frac{\partial \xi_3}{\partial x_2} \\ \frac{\partial \xi_1}{\partial x_3} & \frac{\partial \xi_2}{\partial x_3} & \frac{\partial \xi_3}{\partial x_3} \end{bmatrix} \begin{bmatrix} \frac{\partial \phi}{\partial \xi_1} \\ \frac{\partial \phi}{\partial \xi_2} \\ \frac{\partial \phi}{\partial \xi_3} \end{bmatrix} \tag{3.79}$$

As mentioned earlier, the backward transformation is not known in its explicit form, and thus the Jacobian of the backward transformation cannot be evaluated using (3.79). To circumvent this problem, we begin with the Jacobian of the forward transformation:

$$x_1 = x_1(\xi_1, \xi_2, \xi_3) \quad \rightarrow \quad dx_1 = \frac{\partial x_1}{\partial \xi_1}d\xi_1 + \frac{\partial x_1}{\partial \xi_2}d\xi_2 + \frac{\partial x_1}{\partial \xi_3}d\xi_3 \quad = \frac{\partial x_1}{\partial \xi_i}d\xi_i$$

$$x_2 = x_2(\xi_1, \xi_2, \xi_3) \quad \rightarrow \quad dx_2 = \frac{\partial x_2}{\partial \xi_1}d\xi_1 + \frac{\partial x_2}{\partial \xi_2}d\xi_2 + \frac{\partial x_2}{\partial \xi_3}d\xi_3 \quad = \frac{\partial x_2}{\partial \xi_i}d\xi_i \tag{3.80}$$

$$x_3 = x_3(\xi_1, \xi_2, \xi_3) \quad \rightarrow \quad dx_3 = \frac{\partial x_3}{\partial \xi_1}d\xi_1 + \frac{\partial x_3}{\partial \xi_2}d\xi_2 + \frac{\partial x_3}{\partial \xi_3}d\xi_3 \quad = \frac{\partial x_3}{\partial \xi_i}d\xi_i$$

Similarly, to the backward transformation, we know that:

$$d\xi_1 = \frac{\partial \xi_1}{\partial x_j}dx_j \qquad d\xi_2 = \frac{\partial \xi_2}{\partial x_j}dx_j \qquad d\xi_3 = \frac{\partial \xi_3}{\partial x_j}dx_j \tag{3.81}$$

Substituting equations (3.80) into (3.81) leads to:

$$dx_1 = \frac{\partial x_1}{\partial \xi_1}\left(\frac{\partial \xi_1}{\partial x_j}dx_j\right) + \frac{\partial x_1}{\partial \xi_2}\left(\frac{\partial \xi_2}{\partial x_j}dx_j\right) + \frac{\partial x_1}{\partial \xi_3}\left(\frac{\partial \xi_3}{\partial x_j}dx_j\right)$$

$$dx_2 = \frac{\partial x_2}{\partial \xi_1}\left(\frac{\partial \xi_1}{\partial x_j}dx_j\right) + \frac{\partial x_2}{\partial \xi_2}\left(\frac{\partial \xi_2}{\partial x_j}dx_j\right) + \frac{\partial x_2}{\partial \xi_3}\left(\frac{\partial \xi_3}{\partial x_j}dx_j\right) \tag{3.82}$$

$$dx_3 = \frac{\partial x_3}{\partial \xi_1}\left(\frac{\partial \xi_1}{\partial x_j}dx_j\right) + \frac{\partial x_3}{\partial \xi_2}\left(\frac{\partial \xi_2}{\partial x_j}dx_j\right) + \frac{\partial x_3}{\partial \xi_3}\left(\frac{\partial \xi_3}{\partial x_j}dx_j\right)$$

$$\tag{3.83}$$

where x_1, x_2 and x_3 form an orthonormal basis, therefore, dx_1 cannot be written in terms of dx_2 and/or dx_3 and the only way the equation (3.82) can be true is if:

$$dx_1 = \frac{\partial x_1}{\partial \xi_i}\frac{\partial \xi_1}{\partial x_1}dx_1 \tag{3.84}$$

$$1 = \frac{\partial x_1}{\partial \xi_i}\frac{\partial \xi_1}{\partial x_1} \tag{3.85}$$

Or, in matrix notation:

$$\underbrace{\begin{bmatrix} \frac{\partial x_1}{\partial \xi_1} & \frac{\partial x_1}{\partial \xi_2} & \frac{\partial x_1}{\partial \xi_3} \\ \frac{\partial x_2}{\partial \xi_1} & \frac{\partial x_2}{\partial \xi_2} & \frac{\partial x_2}{\partial \xi_3} \\ \frac{\partial x_3}{\partial \xi_1} & \frac{\partial x_3}{\partial \xi_2} & \frac{\partial x_3}{\partial \xi_3} \end{bmatrix}}_{\text{Forward Jacobian}=[Jac]} \quad \underbrace{\begin{bmatrix} \frac{\partial \xi_1}{\partial x_1} & \frac{\partial \xi_1}{\partial x_1} & \frac{\partial \xi_1}{\partial x_1} \\ \frac{\partial \xi_2}{\partial x_2} & \frac{\partial \xi_2}{\partial x_2} & \frac{\partial \xi_2}{\partial x_2} \\ \frac{\partial \xi_3}{\partial x_3} & \frac{\partial \xi_3}{\partial x_3} & \frac{\partial \xi_3}{\partial x_3} \end{bmatrix}}_{\text{Backward Jacobian}=[Jac]^{-1}} = \begin{bmatrix} 1 & 0 & 0 \\ 0 & 1 & 0 \\ 0 & 0 & 1 \end{bmatrix} \tag{3.86}$$

Therefore, the next task is to find the inverse of the forward Jacobian $[Jac]$. Using Cramer's rule and stating that $[K] = [Jac]^{-1}$, we arrive to the following :

$$[K] = \frac{1}{J}\begin{bmatrix} \beta_{11} & \beta_{12} & \beta_{13} \\ \beta_{21} & \beta_{22} & \beta_{23} \\ \beta_{31} & \beta_{32} & \beta_{33} \end{bmatrix} \quad \text{Where } \beta_{ij} = \text{Co-factors of [Jac] and } J = det(Jac) \tag{3.87}$$

Thus, we have the following relationship.

$$\frac{\partial \phi}{\partial x_i} = \frac{\beta_{ik}}{J} \frac{\partial \phi}{\partial \xi_k} \tag{3.88}$$

Another way of writing this is

$$\frac{\partial \phi}{\partial x_i} = \frac{1}{J} \frac{\partial}{\partial \xi_k} (\beta_{ik} \phi) \tag{3.89}$$

Alternatively, some authors use a more compact notation where $\beta_{ik} = \beta_{ik}/J$. Here, we prefer to keep β_{ik} and J distinct, but we note that both approaches are equivalent. It is possible to define the general second derivative as:

$$\frac{\partial^2 \phi}{\partial x_i \partial x_j} = \frac{1}{J} \frac{\partial}{\partial \xi_k} \left(\beta_{ik} \frac{\partial \phi}{\partial x_j} \right) \tag{3.90}$$

$$\frac{\partial^2 \phi}{\partial x_i \partial x_j} = \frac{1}{J} \frac{\partial}{\partial \xi_k} \left(\beta_{ik} \frac{1}{J} \frac{\partial}{\partial \xi_k} (\beta_{jk} \phi) \right) \tag{3.91}$$

$$\frac{\partial^2 \phi}{\partial x_i \partial x_j} = \frac{1}{J} \frac{\partial}{\partial \xi_k} \left(\beta_{ik} \beta_{jk} \frac{1}{J} \frac{\partial \phi}{\partial \xi_k} \right) \tag{3.92}$$

Using equations (3.89)-(3.92), we can rewrite the governing equations in curvilinear coordinates. For the continuity equation, we obtain the following expressions:

$$\frac{\partial \rho}{\partial t} + \frac{\partial \rho u_i}{\partial x_i} = 0 \tag{3.93}$$

$$\frac{\partial \rho}{\partial t} + \frac{1}{J} \frac{\partial}{\partial \xi_k} (\beta_{ik} \rho u_i) = 0 \tag{3.94}$$

Expanding the terms, we can re-write the continuity equation as:

$$\frac{\partial \rho}{\partial t} + \frac{1}{J} \frac{\partial}{\partial \xi_1} (\beta_{11} \rho u_1 + \beta_{21} \rho u_2 + \beta_{31} \rho u_3) \tag{3.95}$$

$$+ \frac{1}{J} \frac{\partial}{\partial \xi_2} (\beta_{12} \rho u_1 + \beta_{22} \rho u_2 + \beta_{32} \rho u_3) \tag{3.96}$$

$$+ \frac{1}{J} \frac{\partial}{\partial \xi_3} (\beta_{13} \rho u_1 + \beta_{23} \rho u_2 + \beta_{33} \rho u_3) = 0 \tag{3.97}$$

The momentum and energy equations are derived using the same procedure. The complete derivation steps, including the expanded terms, is given in the appendix.

For the momentum equations, we obtain the following expression:

$$\frac{\partial \rho u_i}{\partial t} + \frac{1}{J}\frac{\partial}{\partial \xi_k}\left(\beta_{jk}(\rho u_i u_j + p\delta_{ij})\right) = \frac{1}{J}\frac{\partial}{\partial \xi_k}\left(\beta_{jk}\sigma_{ij}\right) \tag{3.98}$$

where

$$\sigma_{ij} = \frac{\mu}{J}\left[\frac{\partial}{\partial \xi_l}\left(\beta_{jl}u_i\right) + \frac{\partial}{\partial \xi_l}\left(\beta_{il}u_j\right) - \frac{2}{3}\frac{\partial}{\partial \xi_l}\left(\beta_{kl}u_k\right)\delta_{ij}\right] \tag{3.99}$$

For the energy equation, we obtain the following relation:

$$\frac{\partial E}{\partial t} + \frac{1}{J}\frac{\partial}{\partial \xi_k}\left(\beta_{jk}(u_j(E+p))\right) = \frac{1}{J}\frac{\partial}{\partial \xi_k}\left[\beta_{jk}\left(u_j\sigma_{ij} - \kappa\frac{\partial T}{\partial x_j}\right)\right] \tag{3.100}$$

The modification of the governing equations were implemented into Hybrid.

3.5.3 Boundary conditions

From a physical standpoint, the difficulty associated with the definition of well-posed boundary conditions for compressible flows often results in unnatural behaviors near the limit of the domain [129]. The authors emphasize the importance of paying particular attention to the nature of the problem and imposing physically coherent boundary conditions. On the numerical side, the application of lower-order extrapolation at the ghost points of the outflow boundary in the presence of convection or a high gradient favours the onset of spurious inward propagating acoustic instabilities and, in turn, leads to numerical stiffness and convergence challenges [134]. Identification and separation of the different waves crossing the boundary allow an elegant adjustment of the amplitude of the incoming waves to zero. This approach, first proposed by Poinsot & Lele [147], is commonly referred to as Navier-Stokes Characteristic Boundary Conditions (NSCBC), makes use of the *Local One-Dimensional Inviscid (LODI) Relations* to decompose the crossing waves into a sum of characteristics acoustic waves. The extension of the method to curvilinear –or generalized– coordinates is not straightforward. A comprehensive derivation of the

LODI relations in curvilinear coordinates falls out of the scope of the project. Here, we shall limit ourselves to the presentation of the overall implementation procedure rather than the complete derivation of the NSBC. The final transformation matrices that were implemented in the code are given in [94]. For a more complete derivation of the method, we refer the reader to the work of [147] and [93, 94].

Let us start the derivation from the unsteady compressible Euler equations in their differential form:

$$\frac{\partial q}{\partial t} + \frac{\partial F}{\partial \xi_k} = S_\nu \tag{3.101}$$

where

$$q = \{\rho, \rho u_i, \rho E\}^T \qquad\qquad F = \{c_{jk}, f_{ijk}, H_{jk}\}^T \tag{3.102}$$

and S_ν is a source that includes the viscous flux derivatives for the N-S equations. This term is null for the Euler equations. Here, k refer to the direction normal to the boundary surface.

Based on equations (3.94), (3.98) and (3.100), c_{jk}, f_{ijk} and H_{jk} are defined as:

$$c_{jk} = \frac{\beta_{jk}\rho u_j}{J} \qquad f_{ijk} = \frac{\beta_{jk}(\rho u_i u_j + p\delta_{ij})}{J} \qquad h_{jk} = \frac{\beta_{jk}(u_j(E+p))}{J} \tag{3.103}$$

Equation (3.101) can be transformed into a characteristic form in the direction normal to the boundary.

$$\frac{\partial R}{\partial t} + L = S_C \tag{3.104}$$

where $\mathbf{R}$ and $\mathbf{L}$ are the vector of characteristic variables and convection term, respectively. Equation (3.104) was obtained from the following identities :

$$P = \frac{\partial q}{\partial R} \qquad\qquad \partial R = P^{-1}\partial q \tag{3.105}$$

$$L = \Lambda \frac{\partial R}{\partial \xi_k} = P^{-1}\left(\xi_i \frac{\partial F}{\partial \xi_k}\right) \tag{3.106}$$

where Λ is the matrix containing the eigenvalues of the system (3.104). $diag(\Lambda) = [U, U, U, U + c\sqrt{\xi_k^2}, U - c\sqrt{\xi_k^2}]^T$, where c is the speed of sound and $U = \xi_k u_k$. To apply the boundary conditions, equation (3.104) can be recast in terms of primitive variables as follows:

$$\frac{\partial \rho}{\partial t} + L_1 + \frac{\rho}{2c}(L_4 + L_5) = S_{C1} + \frac{\rho}{2c}(S_{C4} + S_{C5}) \tag{3.107a}$$

$$\frac{\partial \tilde{u}}{\partial t} + \frac{1}{2}(L_4 - L_5) = \frac{1}{2}(S_{C4} + S_{C5}) \tag{3.107b}$$

$$\frac{\partial \tilde{v}}{\partial t} + L_3 = S_{C3} \tag{3.107c}$$

$$\frac{\partial \tilde{w}}{\partial t} + L_2 = S_{C2} \tag{3.107d}$$

$$\frac{\partial p}{\partial t} + \frac{\rho c}{2}(L_4 + L_5) = \frac{\rho c}{2}(S_{C4} + S_{C5}) \tag{3.107e}$$

Here, the terms S_C account for a viscous correction, but if we use the LODI relations, the RHS of equations (3.107a)-(3.107e) is zero. Depending on the flow conditions and the type of boundary condition, the value of the crossing waves L_i must be set correctly. At a subsonic outlet, we see that four characteristic waves leave the domain, while one enters at a velocity of $U - c\sqrt{\xi_k^2}$[147]. Thus, to implement a nonreflective outflow, only one condition is necessary, and one could simply set L_5 to zero and deduce the boundary conditions based on (3.107a)-(3.107e). In practice, although the use of NSBC is very effective in reducing the rise of acoustic instabilities near the outflow plane, the method is not perfect and the use of an additional sponge layer is usually required. This is the approach we followed here. A detailed description of the numerical setup, including the definition of the boundary conditions, is presented in Chapter 5.

Chapter 4

Open-source solver for the Nonlinear Parabolized Stability Equations

Abstract

`Krypton` *is an open source framework to solve the linear and nonlinear Parabolized Stability Equations (PSE) on a curvilinear coordinate system as a predictive tool to estimate the laminar-to-turbulent transition under transonic conditions. Written in Python and leveraging well-established libraries, the framework includes a laminar flow solver using a consistent numerical scheme as the modal stability calculations. The code is validated against published cases and can serve as the basis for future development of modal stability-based problems in aerospace engineering, geophysical, and multiphase flows.*

4.1 Motivation and significance

The accurate prediction of the onset of laminar-to-turbulence transition remains a topic of active research in aerospace engineering. The Parabolized Stability Equations (PSE) are a nonlocal stability analysis tool that changes the mathematical nature of the governing equations, and allows the computation of the spatial evolution and interaction of disturbances in weakly nonparallel flows. The integration of nonlinear mode interactions and their spatial evolution are some of the chief advantages of PSE compared to other stability theory paradigms. PSE has shown excellent agreement with experiments and direct numerical simulations (DNS) in boundary layer flows; although some shortcomings of the method are reported [194].

PSE can be used as a standalone predictive tool [140], can be coupled to a higher-fidelity simulation frameworks (such as Large Eddy Simulation, or LES) to set the laminar-to-turbulent transition location [113], or can be integrated into aerodynamic optimization frameworks [136]. Although it has a long history [83, 15, 14, 193, 16], its relevance for predictive modeling of aerospace flows has increased in recent years, especially for aerospace engineering problems where cross-flow instabilities [143], surface roughness [104], and/or compressibility effects become non-negligible [188]. Several well-established stability codes are actively being used by the transition community. Among them, we note institutional codes such as LASTRAC from NASA [132] or NOLOT from DLR, commercial codes such as STABL2D [202], and in-house codes such as EPIC [137]. The few open-source options available are generally focused on incompressible flow transition which present inherent differences to the transonic flow regime. It is the need for an open source comprehensive predictive tool at these complex high-speed flow conditions that motivated the development of the present framework.

`Krypton` is an open-source framework to compute linear and nonlinear PSE on a quasi-three-dimensional, curvilinear coordinate system at transonic conditions relevant to aerospace flows. The framework includes a laminar base flow solver with the exact same numerical methods used for stability calculations. `Krypton` has been developed with a strong emphasis on modularity and flexibility. The code is written in Python to take advantage of the numerous scientific computing packages (NumPy, SciPy, Matplotlib) and

was developed using an Object Oriented Programming (OOP) philosophy. Although not as computationally efficient as other programming languages, Python was nonetheless chosen because it is well established, easy-to-use, and open source. Furthermore, the computational requirements for the laminar base flow calculations remain modest. In addition to the classical flat-plate boundary layer transition, the framework can be used for the study of cross-flow instabilities, effect of pressure gradient, surface roughness-induced transition, and stabilization characteristics of nonadiabatic walls. `Krypton`'s theoretical underpinning, architecture, and illustrative examples are described in the next sections.

4.2   Mathematical background

`Krypton` consists of segregated laminar base flow and modal stability solvers. The mathematical background of the latter, which is the main focus of the code, will be presented here. The parabolized stability equations are derived from the compressible Navier-Stokes equations in their nondimensional and nonconservative form; this equation set is closed with the ideal gas equation of state.

As is common in modal stability theory, the flow quantities are decomposed into a steady component, $\overline{\phi}$, and an unsteady component, ϕ' where:

$$\phi' = \hat{\phi}(x, y) \exp\left(-i \int_x \alpha_{m,n} + \omega t\right) \tag{4.1}$$

By applying the decomposition to the compressible Navier-Stokes equations, subtracting the steady base flow, and lumping together the higher-order fluctuating components into a nonlinear forcing term, we obtain the perturbation transport equation. This represents a linearized form of the compressible Navier-Stokes equations, which is forced with a nonlinear forcing term. These nonlinear terms are neglected when considering the linearized form of the stability equations, denoted either as Linear Stability Theory (LST) or Linear Parabolized Stability Equations (LPSE). When the nonlinear forcing is included, we obtain a form which is used for the Nonlinear Parabolized Stability Equations, or NPSE. The detailed transport equations for the fluctuating components as well as the forcing term

56

are provided in the technical documentation provided with the code.

In PSE, the *history effects* associated with the initial conditions and the spatially varying properties of the perturbation and the base flow are taken into account [86] which results in a streamwise dependency of both the amplitude and phase functions. However, the evolution of the perturbation in the streamwise direction is considered small (weakly non-parallel) and $\partial_x^2 \hat{\phi}$ is assumed to scale with $O(Re_\delta^{-2})$, thus it is negligible compared to its first derivative ($O(Re_\delta^{-1})$), which leads to a system of parabolic equations.

In NPSE, a set of perturbation modes are simultaneously solved, and the nonlinear interaction among the modes acts as a mode-dependent forcing term to the linearized equations. In this sense, the disturbance vector is expanded in terms of its truncated Fourier components and introduced into the parabolized governing equations, which leads to the following system of equations:

$$\left\{ \mathbf{L}\hat{\phi} + \mathbf{S}\frac{\partial \hat{\phi}}{\partial y} + \mathbf{T}\frac{\partial^2 \hat{\phi}}{\partial y^2} + \mathbf{P}\frac{d\alpha}{dx} \right\}_{m,n} = \Lambda_{m,n} \exp\left(-i \int_x \alpha_{m,n} dx \right) \left\{ \hat{\mathbf{F}} + \mathbf{M}\frac{\partial \hat{\phi}}{\partial x} \right\}_{m,n} \quad (4.2)$$

The exact definition of each of these terms is provided in the technical documentation as it represents a well-established implementation of NPSE. The equation is mode-specific and therefore must be solved for every {m,n} combination. Moreover, every mode is subject to the normalization condition (details are provided in the code documentation). The nonlinear forcing terms are evaluated using an approach inspired by [2].

4.2.1   Numerical Methods

One of the main advantages of the PSE is its ability to be solved using a computationally advantageous marching procedure. This approach allows for the use of two different numerical methods in the streamwise and wall normal direction. For instance, a high-order spectral scheme in the normal direction and Backward Differentiation Formulas (BDF) in the streamwise direction. This approach was also preferred by several other authors [71, 117, 146]. Despite its name, the PSE still contains some ellipticity due to the $\partial_x \hat{p}$ term. To avoid numerical instabilities in the marching procedure when the step size is

reduced, `Krypton` uses the stabilization technique proposed by [6].

4.3   Software description

4.3.1   Software Architecture

`Krypton` first solves the laminar compressible Navier-Stokes base flow (in 2D or quasi-3D) and then the corresponding stability problem (either linear stability theory, LST, LPSE or NPSE). Here, *quasi-3D* means that the 3 velocity components (u,v,w) are solved, but only 2 directions are discretized. The code can thus handle three-dimensional flows, but the flow in the span-direction is assumed homogeneous. The entire solution procedure integrates both base flow and stability solvers and provides an integrated approach to the solution of the stability calculations. Figure 4.1 describes the main architecture of the code.

First, all the input of the simulation, including the flow properties (Re, Ma, T_w, ω, β, crossflow intensity), geometry, and the user-defined numerical methods (BDF order, discretization), are specified in the `main.py` file. These inputs are then passed to the module `NumMethod.py` which is used to compute the relevant differentiation matrices (spectral scheme in y and FD/BDF in x). Once the initialization is complete in `main.py` and `NumMethod.py`, the code sequentially proceeds to the base flow and stability solvers.

The module `LaminarFlow.py` first creates an object associated with the discretized Navier-Stokes equations. This object, defined in `NS.py`, contains all the relevant methods to build the linear operator and iteratively solve the set of discretized equations. The governing equations are solved using a Picard iterative method–also referred to as the fixed-point algorithm. For the boundary conditions, we impose ($u = \{1, 0, 0\}$ and $T = 1$) on at the inlet while the pressure is extrapolated from the solution. We impose a traction-free boundary condition at the outlet and in the free-stream. The wall temperature is kept constant ($\frac{T_w}{T_\infty} = C$), although this can be modified for nonadiabatic cases. Then, a base flow solution is obtained.

The converged flow field is then passed to the modal stability solver `FlucFlow.py`.

First, a linear stability theory (LST) problem is solved to provide a valuable starting point for the PSE solvers (either LPSE or NPSE). Given the parabolic nature of the equations, the modes (or mode, for LPSE) are advanced along the streamwise direction through a marching procedure. Both the local LST and the PSE (LPSE/NPSE) procedures are implemented within the PSE.py module. The local stability problem is solved as a matrix eigenvalue problem [207, 86]: $[A]\Phi = \omega[B]\Phi$. To solve the eigenvalue problem for the LST, we impose the boundary conditions on all variables except $\hat{v}$ at the wall and iterate on α with a Newton method until convergence $|\hat{v}(0)| < \epsilon$.

The procedure for the LPSE/NPSE calculations is almost identical to the LST procedure. First, the boundary conditions are slightly different: $\hat{v}(0)$ is now explicitly set to zero, while the condition on $\hat{p}$ at the wall is relaxed. In the LPSE approach, the normalization condition replaces the condition on $\hat{v}$ at the wall in the Newton iterative process; the objective is to find α for which the normalization condition is satisfied. Once the solution is converged at the first streamwise location, the marching procedure begins. For this purpose, we opt for an implicit BDF-based approach. The comprehensive details of the implementation are found in the documentation of the code.

4.4 Illustrative Examples

4.4.1 Computing the marginal stability curve

A first validation test case is the incompressible zero pressure gradient flat plate boundary layer transition in which the Reynolds number, based on the inlet boundary layer thickness, is $Re_\delta = 250$, the Mach number $Ma = 0.1$ and the dimensionless fluctuation frequencies range from $F = 20$ to $F = 300$. The validation of the LPSE results is shown in figure 4.2. This case can be run in examples/example2.py.

```
# Reference and local Reynolds number (Scale with sqrt(x)
setParam.dic['prop']['Re'] = Re0 # Re0 = 250
```
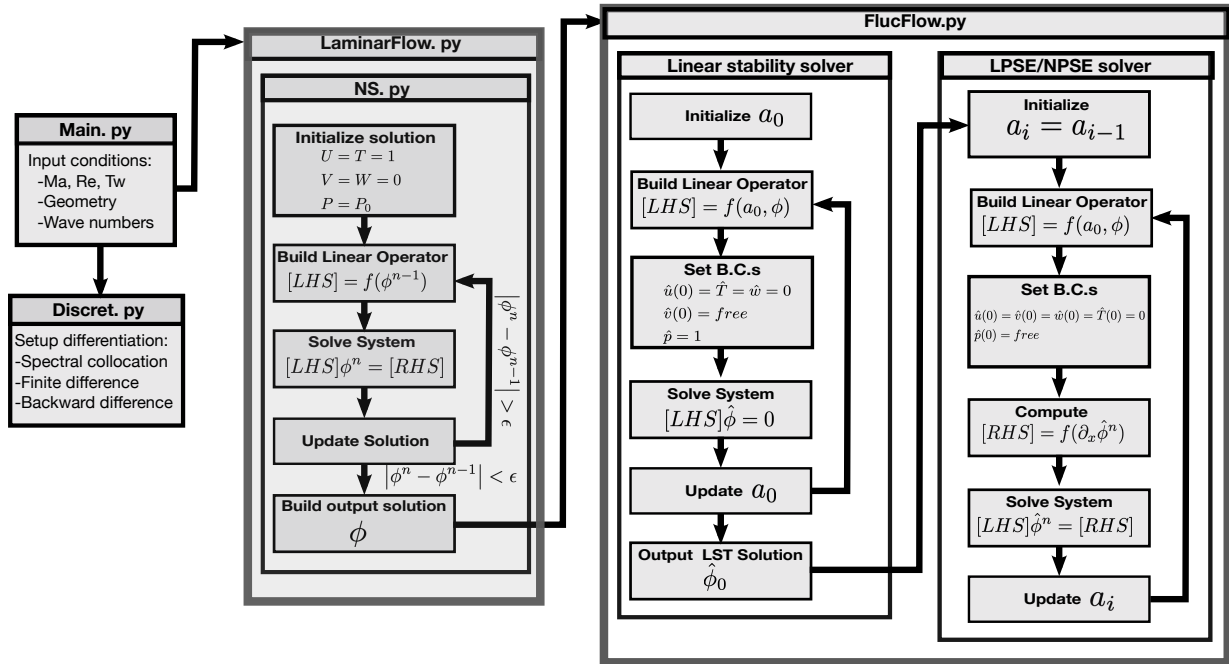
FIGURE 4.1. Algorithmic flow chart for `Krypton`.

```
# Reference Mach numbers
setParam.dic['prop']['Ma'] = 0.1
```

4.4.2   NPSE on smooth backward-facing step

Defining complex geometry

In the second illustrative example, we present a smooth backward-facing step (with the step height $h = \delta$) at $Ma = 0.5$ (see see `examples/example3.py`). Since Python scripts are used as input files, it is possible to use `numpy` functions (or any other package) to define the geometry of the case. To define the smooth step, we use the following:

```
# Nx, Ny : computational grid dimensions
# N : Length of coordinates vector
```
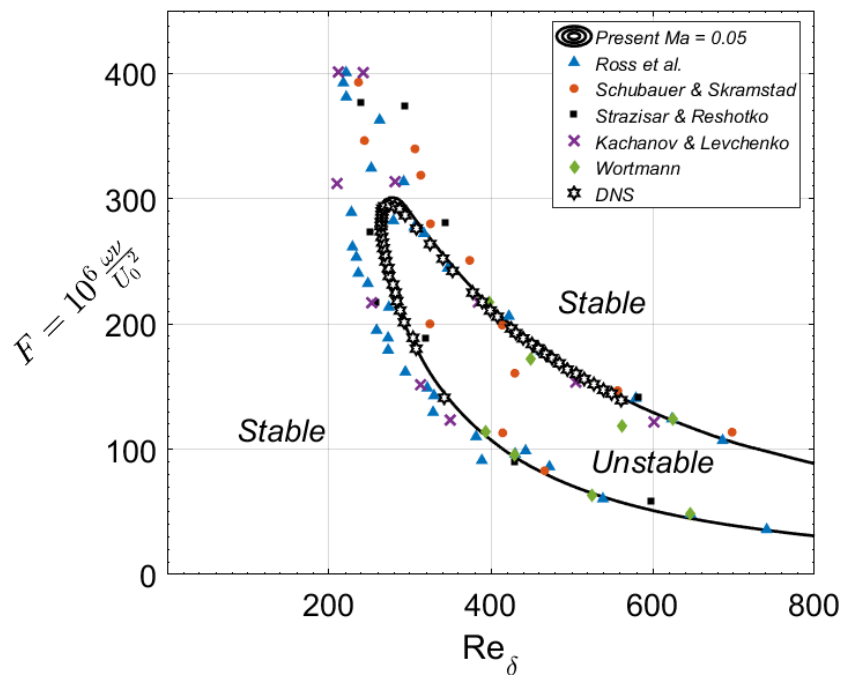
FIGURE 4.2. Neutral stability curve of a flat plate boundary layer at $Ma = 0.1$.
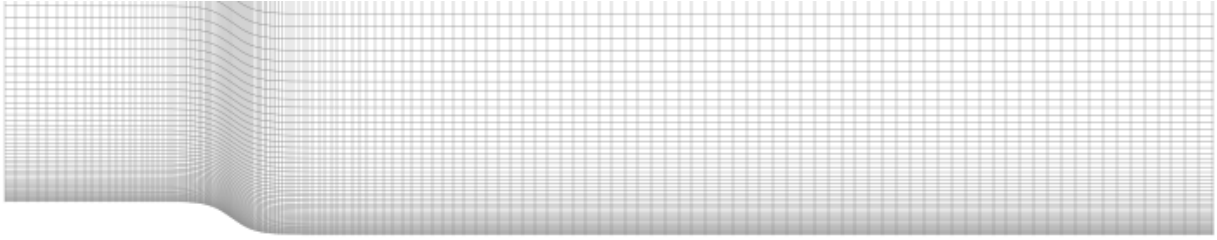
FIGURE 4.3. Curvilinear grid generated by `Krypton` using the `Optimal` algorithm from `Geom.py`

```
h = 1.25e-3 ; a = 10 ; b = 2*X0
coords = np.vstack([x.reshape((1,N)), y.reshape(1,N)]).T
x = np.linspace(-5*X0, Xf, N) ; y = h*(-1-np.tanh(a*(x-b)))
Geom = Geom(coords, Lref, Nx, Ny, Optimal=True)
```

The module `Geom.py` will then generate a curvilinear grid based on the surface description (x, y). Using the option `Optimal = True`, `Geom.py` will automatically increase the density of points in the region of high curvature, see figure 4.3.

Modal analysis

After running the base flow in the smooth backward step, the code will solve the desired modal stability problem. Although it is recommended to solve all modes using the same assumptions (`local`, `linear`, `parallel`), it is nevertheless possible to use different assumptions for each mode or position. As mentioned earlier, both the local LST and the PSE procedures (LPSE / NPSE) are implemented within the `PSE.py` module. In this example, we solve the NPSE equations, and thus `local = False` (except at first station), `linear = False` and `parallel = False`.

These settings must be defined in the parameter input stage before any calculations are performed using the following syntax:

```
# Setting up the initial conditions
for m, n in setParam.dic['modes'][i0]:
```

```python
# If True solved locally without
# implicit marching procedure
setParam.dic[(m,n)]['local'][i0]    = True
# if True nonlinear terms are neglected
setParam.dic[(m,n)]['linear'][i0]   = False
# if True Streamwise derivatives
# in the base flow field are neglected.
setParam.dic[(m,n)]['parallel'][i0] = False
#  Initial amplitude of the fluctuations
setParam.dic[(m,n)]['A_0'] = Amplitude * 1/(n+1)
```

The fluctuation amplitude history (see Figure 4.4) predicts a transition shortly after the step as the amplitude of the second mode increases drastically.

4.5 Impact

Although the theoretical framework for PSE has been developed for some time, there has been growing interest in including these methodologies into a wider range of aerospace applications such as the consideration of stability due to surface roughness, cross-flow instability, transpiration cooling or to optimize natural laminar flow designs. The modal stability framework, developed in Krypton, can be integrated into a number of subfields within aerospace engineering, such as the consideration of higher fidelity stability calculations for a multidisciplinary design analysis and optimization (MDAO). Much of the underlying PSE-based framework can also have a direct contribution to other fields such as acoustics. The underlying equation set can be leveraged, with modest modifications, to compute the propagation of wavepackets in acoustics [158, 85]. The extension of Krypton for acoustic calculations will be a topic future research. Outside of aerospace engineering, the use of the present modal stability framework can be extended, with some effort, to compute liquid film instabilities in multiphase flows as well as interfacial wave dynamics for geophysical flows.
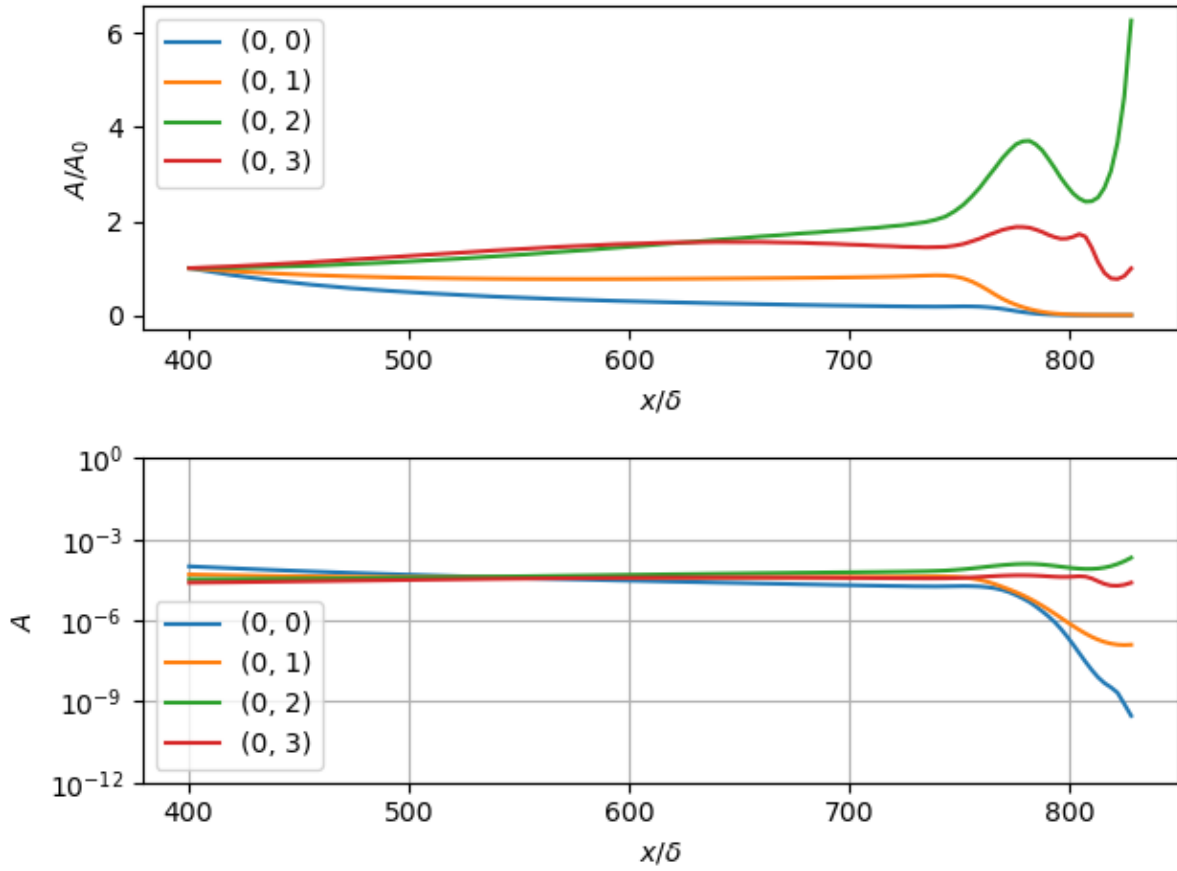
FIGURE 4.4. Mode amplification for the backward-facing step at $\frac{x}{\delta} = 800$, $Ma = 0.5$, $Re_\delta = 400$, $h = \delta$.

The barrier to entry for PSE-based modal stability calculations remains sizeable, especially for researchers outside the subdiscipline of transitional flows. `Krypton` aims to address the need for an openly accessible compressible, curvilinear modal stability tool that can be easily extended and adapted. The framework, which provides an integrated support for base flow calculations, is designed with a high-level of modularity with object-oriented coding written in Python. These features will help reduce the barrier to entry and provide the opportunity for researchers to extend the present code. `Krypton` is the basis for a number of ongoing publications on roughness-induced stability calculations [104], as well as the consideration of wall-heating-induced transition cases.

4.6   Conclusions

`Krypton` is a comprehensive framework, written in Python, to solve modal stability-based fluid dynamics problems. It aims to address the needs of the broad research community focused on determining the stability characteristics of weakly nonparallel aerospace flows. `Krypton` includes a base flow solver in 2D or quasi-3D along with a stability module that includes the computation of the linear and nonlinear parabolized stability equations. The main feature of the code is that it computes the compressible stability equations on a curvilinear mesh, which enables the consideration of more complex geometries including smooth surface roughness stability problems.

Chapter 5

The role of two-dimensional smooth roughness on the modal growth in compressible boundary layer flow

This chapter has been adapted from Francis Lacombe and Jean-Pierre Hickey. "The role of two-dimensional smooth roughness on the modal growth of instability in compressible boundary layer flow", Journal of Fluid Mechanics, 2022 (under review).

Abstract

The effect of smooth, two-dimensional surface roughness on the stability characteristics at transonic conditions ($M = 0.714$) is investigated using a combination of parabolized stability equations (PSE) and direct numerical simulations (DNS). In specific, the influence of the two-dimensional smooth roughness on the stability of 2D T-S waves is investigated with a particular emphasis on frequency content generation. Two variants of the same setup consisting of an array of 5 sinusoidal humps of two different heights are considered. The analysis of the wall friction spectrum reveals a stronger destabilizing effect on the higher frequencies for the case featuring the highest humps. This causes a rapid growth of secondary instabilities that skip the standard T-S mechanism and gives rise to a cyclical transitional pattern in which both late K-type structures and premature bypass transition are observable. The modal stability analysis also shows that, in the presence of two-dimensional smooth roughness, the mode experiencing the highest linear growth is three-dimensional. The results reveal that PSE is sufficiently accurate to be used in combination with more sophisticated approaches (DNS or LES) in order to reduce the computation time, including in complex flow situations featuring compressibility and boundary roughness.

5.1 Introduction

For aircraft manufacturers, friction is the sinew of war; delaying the laminar-to-turbulent transition–even over a short distance–can lead to important drag reduction and overall performance improvements. Transition is important in the fully incompressible regime, but is particularly critical at higher-speeds–in the limit of high-enthalpy conditions, the transition location can affect the thermal loading and, thus, determine the characteristics of the thermal protection system, which directly impacts the cost and weight of the entire system [177]. The laminar-to-turbulent transition is thus a key feature to be characterized in many aerospace flows, especially when compressibility effects are nonnegligible. In external flows with low freestream turbulence intensity over smooth walls with no crossflow, the transition to turbulence is dominated by convective Tollmien-Schlicting (T-S) instabilities which develop and grow until nonlinear interactions take hold as the flow transitions. This transition pathway is common to both sub- and supersonic regimes. Under higher freestream perturbations, the exponential growth of the instability modes is bypassed and other transitional mechanisms dominate.

Although a smooth, flat plate boundary layer with zero pressure gradient represents the most canonical setup to study the laminar-to-turbulent transition, such a simplified setup is typically not encountered in aeronautical flows. The walls often have surface imperfections such as dents, gaps, cavities, joints, or rivet heads, which directly impact the transitional characteristics of the boundary layer. Surface imperfections, although necessary for aircraft manufacturability, can lead to premature transition with all the associated deleterious consequences of turbulent flow. For example, over the nacelle, the transition to turbulence can be delayed by displacing downstream some of the geometric features that may instigate transition; the nacelle and the inlet lip can be designed to ensure that the gaps along the junction of the components do not induce a premature transition to turbulence. These modifications, along with other boundary layer stabilization design considerations, can delay transition to about 50% of the nacelle chord, which can result in savings in aircraft fuel of the order of 1% [125, 216].

The role of surface imperfections on the transition to turbulence is more nuanced than intuition would lead us to believe. [50] observed that the minimum height of a surface

imperfection (bulges, hollows, and ridges) that modifies the location of the boundary layer transition is independent of its geometric shape, a result that was slightly corrected in later work by [75]. Based on detailed experimental observations, [96] argued that two-dimensional roughness does not introduce new disturbances into the flow but accelerates the premature transition through the destabilization of the existing instability modes in the boundary layer. The minor effect of surface roughness has also been observed in fully turbulent boundary layer flows, in which the coherent structures remain, to a large extent, invariant to the presence of roughness [203]. Although in a turbulent channel flow with sinusoidal wall roughness, the compressibility and confinement effects of the setup make the impact of surface waviness more apparent [201]. For transitional studies, 2D surface waviness has been shown [211] to have an unconditionally destabilizing effect through a selective amplification of the T-S waves. The work by Wie et al. [211] was primarily based on a spatially-marching parabolized stability equation (PSE) and, thus, the receptivity of these instability modes could not be assessed. These investigations were extended by [190] by comparing a linearized Navier-Stokes (LNS) with a PSE formulation. In a subsequent work [191], it was found that the instabilities were amplified by deeper and wider gaps. The transitional mechanism based on the growth of the T-S waves remains dominant as long as the height of the roughness remains small. [37] estimated that as long as the height of a surface step is less than approximately 1.5 times the displacement thickness of the boundary layer, the underlying mechanism remains unchanged. Other types of surface imperfections can modify the transitional mechanism, affecting the path to turbulence. For example, [217] showed that the impact of a standing acoustic wave mode in a deep gap can force different T-S modes in the boundary layer. This results in a premature transition for a flat plate but can also delay transition, through destructive mode forcing, in a forward facing step.

Surface waviness, a canonical type of smooth roughness, represents a generic set-up to explore the effect of surface imperfection on the growth of instability modes in transitional flows. Experimental works have shown that the 2D wavy roughness is more destabilizing than a periodic array of 3D smooth roughness. This is due to the greater vertical displacement over the 2D roughness, which promotes the emergence of an inflectional instability which is not as prominent in the 3D staggered smooth array [66]. This contrasts with

the effect of the 3D isolated roughness elements, which are known to admit additional instability modes in the generated wake of the elements [112, 150, 24]. [35] experimentally investigated, among others, the effect of bump height and Mach number on the transition, with a separation region. It was observed that the Mach number effects were, for the most part, small, although for a smaller bump height, the transition location was modified, although may have been tied to a concomitant increase in the wall temperature with Mach number. In high-Mach number flows, smooth roughness with multiple wavelengths can suppress the acoustic second mode [221], thus stabilizing the boundary layer. Other works, such as [56] have suggested that alterations in the second-mode instability are tied to the mean flow modification caused by smooth roughness. The understanding of the effects of smooth roughness-induced transition in the transonic regime remains incomplete, especially with regard to the exact mechanism of transition and impact of compressibility.

To this end, we present a numerical work based on a combined study using the Parabolized Stability Equations (PSE) and Direct Numerical Simulations (DNS) to investigate the roughness-induced transition in transonic flows over surface waviness. There are typically two families of modal-stability-based transition approaches: *local* and *nonlocal* methods. The *local* stability analysis is carried out at a specific location in the flow, in opposition to the *nonlocal* approach that takes into account the evolution of perturbations along their path [86]. Traditionally, the local approaches, such as the Linear Stability Theory (LST), of which the Orr-Sommerfeld equations (OSE) are most well known, perform particularly well in incompressible flows over simple geometries. However, in realistic aeronautical flows, compressibility, pressure gradients, cross-flow, and roughness effects promote premature transition and are no longer negligible. For this reason, nonlocal approaches, such as the PSE, have received considerable attention in the last decades. [65] was the first to study the evolution of Tollmien-Schlichting (T-S) waves through a set of parabolized stability equations. [83] and [15] extended PSE to account for the nonlinear interaction between a subset of eigenmodes. More recently, [99] and [130] used the Nonlinear PSE (NPSE) approach to study the secondary instability of cross flow under hypersonic conditions. [113] showed that NPSE are sufficiently accurate to be used as inflow boundary conditions for Direct Numerical Simulation (DNS) or Large Eddy Simulation (LES). In this way, it is possible to significantly reduce the size of the computation domain by modeling

the pre-transitional region using a simple boundary condition supplied from the NPSE. Their work focused on an incompressible zero-pressure gradient boundary layer, without any curvature, roughness, or compressibility effects.

The effect of distributed roughness on the transitional characteristics of the compressible boundary layer was recently investigated by [185] who revisited the concept of roughness shielding to reduce the receptivity of discrete roughness elements of large amplitude. Using a hybrid DNS-experimental approach, they found that the use of continuous flat roughness strips upstream or downstream of surface imperfections had a beneficial effect on transition control. More recently, [128] and [69] investigated the effect of three-dimensional discrete roughness elements on hypersonic flows using different approaches; Montero focused on a modal stability theory, while Hein used a nonmodal approach.

In the present contribution, we study the effects of an array of small, two-dimensional, sinusoidal smooth wall roughness under transonic conditions using NPSE and DNS. The purpose of this work is to: (1) validate the applicability of NPSE in the presence of curvature and compressibility effects; (2) study the effect of two-dimensional smooth roughness on the modal and nonmodal growth of instabilities in compressible boundary layers subject to different levels of finite-amplitude disturbances; (3) investigate the effect of two-dimensional roughness on the development of span-periodic instabilities. In the following section, the numerical and theoretical background for both the modal stability theory and the direct numerical simulations is presented. In Section 5.3, two cases of roughness-induced transitions are presented and analyzed first using linear PSE and followed by a combined study of the nonlinear PSE and DNS. Finally, Section 5.4 presents the main conclusions of this work. The effect of two-dimensional smooth surface roughness on stability characteristics under transonic conditions ($M = 0.714$) is investigated using a combination of parabolized stability equations (PSE) and direct numerical simulations (DNS). In particular, the influence of the two-dimensional smooth roughness on the stability of 2D T-S waves is investigated with a particular emphasis on frequency content generation. Two variants of the same setup consisting of an array of 5 sinusoidal humps of two different heights are considered. The analysis of the wall friction spectrum reveals a stronger destabilizing effect on the higher frequencies for the case featuring the highest humps. This causes a rapid growth of secondary instabilities that skip the standard T-S mechanism

and gives rise to a cyclical transitional pattern in which both late K-type structures and premature bypass transition are observable. The modal stability analysis also shows that, in the presence of two-dimensional smooth roughness, the mode experiencing the highest linear growth is three-dimensional. The results reveal that PSE is sufficiently accurate to be used in combination with more sophisticated approaches (DNS or LES) in order to reduce the computation time, including in complex flow situations featuring compressibility and boundary roughness.

5.2 Numerical and theoretical background

The numerical tools and the necessary theoretical background are presented in this section. First, the Parabolized Stability Equations (PSE), which is a subset of modal stability theory, is discussed and the numerical solver used for this study is presented. Thereafter, the numerical details of Hybrid, the direct numerical simulation (DNS) solver used in this study, are discussed.

5.2.1 Dimensionless variables

In this work, all variables are non-dimensionalized following the method described in [127].

$$x_i = \frac{x_i^*}{\delta} \qquad u_i = \frac{u_i^*}{u_0} \qquad T = \frac{T^*}{T_0} \qquad p = \frac{p^*}{p_s}$$

$$\mu = \frac{\mu^*}{\mu_0} \qquad \rho = \frac{\rho^*}{\rho_0} \qquad c_p = \frac{c_p^*}{c_{p0}} \qquad \lambda = \frac{\lambda^*}{\lambda_0} \qquad (5.1)$$

Here, dimensional values are defined with an asterisk (*), the subscript 0 represents reference values, $\delta = \sqrt{\frac{\nu_0 x_0}{u_0}}$ is a length scale proportional to the thickness of the *inlet* boundary layer and $p_s = \rho_0 u_0^2$ is the pressure scale. In the PSE theory, the solution is sought using a marching procedure, and the final location is often unknown, as the computation usually stops when the solution diverges. Thus, it is common to use the inlet quantities as

reference. The reference Reynolds and Mach numbers are therefore defined as

$$Re_\delta = \sqrt{\frac{u_0 x_0}{\nu_0}} \qquad\qquad Ma = \frac{u_0}{\sqrt{\gamma R_0 T_0}} \qquad (5.2)$$

5.2.2   Modal stability theory

The modal stability theory is a branch of fluid mechanics that studies the evolution in time and/or space of modal-like perturbations on a base flow. Starting from the compressible Navier-Stokes equations in nonconservative form, the equations are linearized to obtain the *Linearized Compressible Navier-Stokes equations*:

$$\frac{\partial u_i}{\partial x_i} = \frac{1}{T}\frac{DT}{Dt} - \frac{1}{p}\frac{Dp}{Dt} \qquad (5.3a)$$

$$\rho\frac{Du_i}{Dt} = -\frac{\partial p}{\partial x_i} + \frac{1}{Re}\frac{\partial \tau_{ij}}{\partial x_j} \qquad (5.3b)$$

$$\rho c_p \frac{DT}{Dt} = \frac{1}{RePr}\frac{\partial}{\partial x_i}\left(\lambda\frac{\partial T}{\partial x_i}\right) + (\gamma - 1)M^2\left(u_i\frac{\partial p}{\partial x_i}\right) + \phi_{ij} \qquad (5.3c)$$

where u_i, ρ, γ, λ, p, and T represent respectively the velocity (vector), density, specific heat ratio, thermal conductivity, thermodynamic pressure and temperature; τ_{ij} is the viscous stress tensor according to the usual definition and ϕ_{ij} is the viscous heating term. In the above equations, M, Pr, and Re are nondimensional Mach, Prandtl, and Reynolds numbers. The above flow quantities can be decomposed into a steady, $\bar{q}$, and a fluctuating modal component, q', such that: $q(\vec{x}, t) = \bar{q}(\vec{x}) + q'(\vec{x}, t)$. Thus, the decomposition of the

terms in the *LCNSE* equation (5.4a-5.4c) results in:

$$\frac{\partial u_i'}{\partial x_i} + \left(\frac{T'}{\overline{T}} + \frac{p'}{\overline{p}} \right) \frac{\partial \overline{u}_i}{\partial x_i} = \frac{p'}{\overline{p}\,\overline{T}} \frac{\overline{DT}}{\overline{Dt}} + \frac{1}{\overline{\overline{T}}} \left[\frac{\overline{D}T'}{Dt} + u_i' \frac{\partial \overline{T}}{\partial x_i} \right]$$

$$- \frac{T'}{\overline{p}\,\overline{T}} \frac{\overline{D}\overline{p}}{\overline{Dt}} - \frac{1}{\overline{p}} \left[\frac{\overline{D}p'}{Dt} + u_i' \frac{\partial \overline{p}}{\partial x_i} \right] + \mathcal{C}'' \tag{5.4a}$$

$$\overline{\rho} \left[\frac{1}{\overline{p}} p' - \frac{\overline{\rho}}{\overline{T}} T' \right] \frac{\overline{D}\overline{u}}{\overline{Dt}} + \overline{\rho} \left[\frac{\overline{D}u_i'}{\overline{Dt}} + u_j' \frac{\partial \overline{u}_i}{\partial x_j} \right] = -\frac{\partial p'}{\partial x_i} + \frac{1}{Re} \frac{\partial \tau_{ij}'}{\partial x_j} + \mathcal{M}'' \tag{5.4b}$$

$$\overline{\rho} c_p \left[\frac{1}{\overline{p}} p' - \frac{1}{\overline{T}} T' \right] \frac{\overline{DT}}{\overline{Dt}} + \overline{\rho} c_p \left[\frac{\overline{D}T'}{\overline{Dt}} + u_j' \frac{\partial \overline{T}}{\partial x_j} \right] = \frac{1}{RePr} \frac{\partial}{\partial x_i} \left(\lambda' \frac{\partial \overline{T}}{\partial x_i} + \overline{\lambda} \frac{\partial T'}{\partial x_i} \right)$$

$$+ (\gamma - 1)M^2 \left(\overline{u}_i \frac{\partial p'}{\partial x_i} + u_i' \frac{\partial \overline{p}}{\partial x_i} \right) + \frac{(\gamma - 1)Ma^2}{Re} \phi_{ij}' + \mathcal{E}'' \tag{5.4c}$$

where $\mathcal{C}''$, $\mathcal{M}''$ and $\mathcal{E}''$ contain the nonlinear terms. The total derivative operator, $\frac{\overline{D}}{\overline{Dt}}$, is defined as

$$\frac{\overline{D}}{\overline{Dt}} = \frac{\partial}{\partial t} + \overline{u}_j \frac{\partial}{\partial x_j} \tag{5.5}$$

	$\hat{\boldsymbol{q}}(\vec{x})$	$\boldsymbol{\chi}(\vec{x},t)$	Main applications	Complexity
LST-1D	$\hat{q}(y)$	$\exp[i(\alpha(x)+\beta z-\omega t)]$	1D parallel flows such as Similarity solutions (Blasius, jet) ZPG flat plate with cross-flow	$O(\Delta t^1)$
PSE-2D	$\hat{q}(x,y)$	$\exp\left[i(\int_x \alpha dx+\beta z-\omega t)\right]$	2D weakly non-parallel flows such as BL with roughness/curvature	$O(\Delta t^1)$
PSE-3D	$\hat{q}(x,y,z)$	$\exp\left[i(\int_x \alpha dx-\omega t)\right]$	3D weakly non-parallel flows BL with roughness/curvature	$O(\Delta t^2)$
BiGlobal / LST-2D	$\hat{q}(y,z)$	$\exp[i(\alpha x-\omega t)]$	Non-homogeneous parallel flows shear flows, such as wakes and steps	$O(\Delta t^2)$
LST-3D / Global	$\hat{q}(x,y,z)$	$\exp[-i\omega t]$	strongly non-parallel flows free-convection, recirculating flows	$O(\Delta t^3)$

TABLE 5.1. $\hat{q}$ and χ definition for different modal stability theories. α, β and ω are the streamwise, spanwise and temporal wavenumbers. Complexity refers to the computational complexity of the model

In modal stability theory, the perturbation vector, q', takes the form of $q'(\vec{x}, t) = \hat{q}(\vec{x})\chi(\vec{x}, t)$, where $\hat{q}$ and χ are the amplitude and phase functions, respectively. Depending on the selected modal stability approach, $\hat{q}$ and χ can have slightly different definitions. Table 5.1 presents the definition of these terms for the main modal approaches. In the present work, the focus is on the effect of 2D smooth roughness on the growth of compressible T-S waves and thus we use the following Fourier decomposition of q':

$$\boldsymbol{q}'(\mathbf{x}, t) = \sum_{m=0}^{M} \sum_{n=0}^{N} \hat{\boldsymbol{q}}_{m,n}(x, y)\chi_{m,n}(x, z, t) + c.c. \tag{5.6}$$

where $c.c.$ refers to the complex conjugate and

$$\chi_{m,n}(x, z, t) = \exp(\Gamma_{m,n}) = \exp\left[i\int_x \alpha_{m,n}(x)dx + i(m\beta z - n\omega t)\right] \tag{5.7}$$

In PSE, the growth of the perturbation is assumed to be mostly contained in the phase function $\chi_{m,n}$ such that the amplitude function, $\hat{q}$, can only grow slowly in the streamwise direction ($\partial_x \hat{q} >> \partial_{xx}\hat{q}$), an assumption that results in a parabolized form of the stability equations, hence the name *Parabolized Stability Equations* or PSE. In summary, the following assumptions are made:

$$\frac{\partial \Gamma}{\partial y} = 0 \qquad \frac{\partial^2 \Gamma}{\partial y^2} = 0 \qquad \frac{\partial \hat{q}}{\partial z} = 0 \qquad \frac{\partial^2 \hat{q}}{\partial x^2} = 0 \tag{5.8}$$

By substituting (5.6) into the LCNSE and using the PSE-2D assumptions, it is possible to show that the PSE for a given mode $\{m, n\}$ can be written in a matrix-vector system of the form:

$$\left\{ \mathcal{L}\hat{q} + \mathcal{L}_x \frac{\partial \hat{q}}{\partial x} + \mathcal{L}_y \frac{\partial \hat{q}}{\partial y} + \mathcal{L}_{yy} \frac{\partial^2 \hat{q}}{\partial y^2} \right\}_{m,n} = \left\{ \exp\left(-i\int_x \alpha dx\right) \mathcal{F}'' \right\}_{m,n} \tag{5.9}$$

where $\hat{q} = [\hat{p}, \hat{u}_i, \hat{T}]^T$ and $\mathcal{F}'' = [\mathcal{C}'', \mathcal{M}'', \mathcal{E}'']$. Since α is variable, we need one more equation to close the system and ensure the PSE-2D assumptions are met, this is where the so-called

auxiliary condition come into play:

$$\overline{\rho} \int_0^\infty \hat{q}_{m,n}^\dagger \frac{\partial \hat{q}_{m,n}}{\partial x} dy = 0 \tag{5.10}$$

In linear stability theory, the base flow ($\overline{q}$) does not depend on q' and the origin of $\overline{q}$ is of little importance. Therefore, one could choose to either use a standalone CFD solver, interpolate the velocity field from experimental data, or solve a set of self-similar equations (Blasius, Falkner-Skan-Cooke, etc.) to compute the base flow. However, if nonlinearities are large enough, the mean flow distortion (MFD) becomes significant and the base flow has to be redefined as $\overline{q} = q_{lam} + \hat{q}_{(0,0)}$. To maintain consistency, the numerical formulation of q_{lam} and $\hat{q}_{(0,0)}$ should be the same. Therefore, the same governing equations (5.3a)-(5.3c) should be solved for both the base flow and the derivation of the PSE.

Mean Flow Distorsion (MFD)

Physically, the Mean Flow Distortion (MFD) –or mode $(0,0)$– is a non-oscillatory perturbation resulting from the nonlinear interactions between the fluctuations and the base flow. Since it does not have a complex conjugate, both $\hat{q}_{0,0}$ and $\chi_{m,n}$ are purely real, and therefore α is purely imaginary. The rapid change in the shape function is mainly caused by oscillatory behavior rather than growth [208] and the normalization condition (5.10) serves this exact purpose by ensuring that the growth of energy is contained in the phase function χ. However, because the MFD does not have a wavenumber, the use of the normalization condition to redirect the energy from the amplitude function to the phase function is therefore impossible. To bring closure to the problem, $\alpha_{0,0}$ is instead set to 0 and thus the growth of the perturbation is completely accounted for by the amplitude function $\hat{q}$.

PSE: Numerical considerations

Both the laminar base flow and the modal stability analysis were computed using Krypton [105], an open-source framework to solve the compressible NPSE in curvilinear coordinates.

The solver used herein, along with all input files, can be downloaded at: . Krypton also solves the steady, laminar base-flow solution in two dimensions, using numerical methods consistent with the NPSE calculations. In Krypton, the steady laminar base flow is discretized using a central fourth-order finite difference scheme. The governing equations are solved simultaneously using an efficient fixed-point iteration method. For the evolution of the perturbation equations, a first-order implicit marching procedure is used in the streamwise direction while a spectral approach is favored in the wall-normal direction. The spectral collocation method is used as it is well suited for the PSE and has been used by several other authors [16, 173, 190]. The main idea is to expand the solution in terms of global basis functions so that the numerical solution satisfies the PDE at the *collocation points*, also termed *Chebyshev Gauss-Lobatto points* [78], defined as: $\xi_j = \cos \frac{\pi j}{n}$. These points were chosen to minimize Runge's phenomenon at the boundaries of the domain and help stabilize the integration of the PSE. The spectral collocation method has the advantage of greatly simplifying the expression of the discretized equation with a compact matrix-vector notation in which the solution and its derivative take the following forms.

$$u^*(\xi) = \sum_{j=0}^{n} \psi_j(\xi) u(\xi_j) \qquad \frac{du^*}{d\xi} = \sum_{j=0}^{n} \Psi_{ij} u(\xi_j) = \mathbf{\Psi} \cdot \vec{u}(\xi), \qquad (5.11)$$

where ψ_j is the Lagrange polynomial passing by the *Chebyshev Gauss-Lobatto points*. The spectral convergence makes the method particularly efficient for simple problems in which the location of the computational nodes is not crucial. However, to accurately capture the physics of the problem near the wall, we use a multi-element spectral-collocation method consisting of multiple lower order collocation subdomains. In this way, the problem can be elegantly discretized using the following differentiation matrices:

$$\mathcal{D} = \begin{bmatrix} \mathbf{\Psi}_0 & 0 & 0 \\ 0 & \mathbf{\Psi}_1 & 0 \\ 0 & 0 & \mathbf{\Psi}_2 \end{bmatrix} \qquad \mathcal{D}^2 = \mathcal{D} \cdot \mathcal{D} \qquad (5.12)$$

where Ψ_i is the standard spectral differentiation matrix for the ith subdomain. In practice, this method is more robust but also less memory-consuming than standard collocation methods, as the resulting differentiation matrix is sparse. We typically use 12th-degree polynomials and 20 subdomains with a stronger concentration at the wall, which results in a sparsity index in the range of 0.95.

Using (5.12) and Backward Differentiation Formulas (BDF), the PSE system can be written as:

$$\left[\mathcal{L} + \mathcal{D}\mathcal{L}_y + \mathcal{D}^2\mathcal{L}_{yy} - \frac{\mathcal{L}_x}{\Delta x} \right] \vec{q}_i = \exp\left(-i\int_x \alpha dx \right) \mathcal{F}'' - \frac{\mathcal{L}_x}{\Delta x} \vec{q}_{i-1} \tag{5.13}$$

where $\vec{q} = [\hat{u}, \hat{v}, \hat{w}, \hat{p}, \hat{T}]^T$, $\mathcal{D}$ is the differentiation matrix and the matrices depend only on the base flow and the wavenumbers.

As mentioned earlier, the equations are parabolized as the second x-derivative of $\vec{q}$ was eliminated using the normalization condition. However, there is still some ellipticity in the system, mainly caused by the pressure gradient terms. The problem arises when the step size becomes smaller than the wavelength of the mode, i.e., when $\Delta x < \frac{1}{|\alpha_r|}$[109], where α_r represents the phase of the fluctuation in the streamwise direction. To alleviate the problem, one possibility is to define a minimal lower bound on the marching-step size. In practice, it is not always possible, as complex geometries may require a smaller step size to accurately represent regions of higher curvature. The stabilization technique proposed by Andersson [6], although very efficient at suppressing the numerical instabilities as the step size is reduced, does not garantee the validity of the PSE near discontinuities or sharp corners. Further investigations to quantify this limit in terms of curvature of the wall or temperature variation are needed. Here, we will limit ourselve to validate the PSE on two cases using DNS. Alternatively, as shown by [109], it is possible to drop the $\frac{\partial \hat{p}}{\partial x}$ terms, in which case the solution is significantly affected while the step size restriction is relaxed but not eliminated. To avoid these workarounds, it is possible to add a stabilization term to the system, as done in the current implementation in Krypton. The stabilizing term, μ, is added to the system following the approach of [86]:

$$\mathbb{L}\hat{q} + \mu\mathbb{L}\frac{\partial\vec{q}}{\partial x} = -\mathcal{L}_x\frac{\partial\vec{q}}{\partial x} \tag{5.14}$$

79

Once discretized:

$$\left[\mathbb{L} + \frac{\mu}{\Delta x}\mathbb{L} + \frac{\mathcal{L}_x}{\Delta x}\right]\vec{q_i} = \left[\frac{-\mathcal{L}_x - \kappa\mathbb{L}}{\Delta x}\right]\vec{q_{i-1}} \tag{5.15}$$

where $\mathbb{L} = \mathcal{L} + \mathcal{D}\mathcal{L}_y + \mathcal{D}^2\mathcal{L}_{yy}$ and κ is defined as $\max(\frac{2}{|\alpha_r|} - 2\Delta x, 0)$ and has the same order of magnitude as the truncation error associated with the first-order backward differentiation scheme.

5.2.3 Direct Numerical Simulation

In parallel to the PSE framework described above, a Direct Numerical Simulation (DNS) of an identical roughness-induced transitional configuration was performed using Hybrid, a high order finite difference code developed by Johan Larsson and Ivan Bermejo-Moreno [12]. Hybrid solves the compressible Navier-Stokes equations using a conservative formulation with a skew-symmetric convective term for stability.

$$\frac{\partial \rho}{\partial t} + \frac{\partial \rho u_i}{\partial x_i} = 0 \tag{5.16a}$$

$$\frac{\partial \rho u_i}{\partial t} + \frac{\partial}{\partial x_j}\left(\rho u_i u_j + p\delta_{ij}\right) = \frac{\partial \tau_{ij}}{\partial x_j} \tag{5.16b}$$

$$\frac{\partial E}{\partial t} + \frac{\partial}{\partial x_j}\left(u_j(E + p)\right) = \frac{\partial}{\partial x_j}\left(u_i\tau_{ij} - \kappa\frac{\partial T}{\partial x_j}\right) \tag{5.16c}$$

where the nomenclature is similar to the equations presented in the previous section, although the last equation solves for the total energy (internal and kinetic), $E = \rho e + \frac{1}{2}\rho u_i u_i$, of the fluid. The equation set is closed with the ideal gas law assuming a calorically perfect gas. The viscosity is computed using a temperature-dependent power law, and a constant Prandtl number of 0.7 is assumed. Hybrid classically solves the equations on a structured Cartesian mesh but, for the needs of the current research, a curvilinear coordinate system was implemented and validated.

Hybrid is a highly parallelized code that uses a sixth-order central finite-difference scheme coupled with high-order filtering for the spatial derivatives. Although the code has an adaptive scheme which can switch to a WENO scheme in regions of large spatial
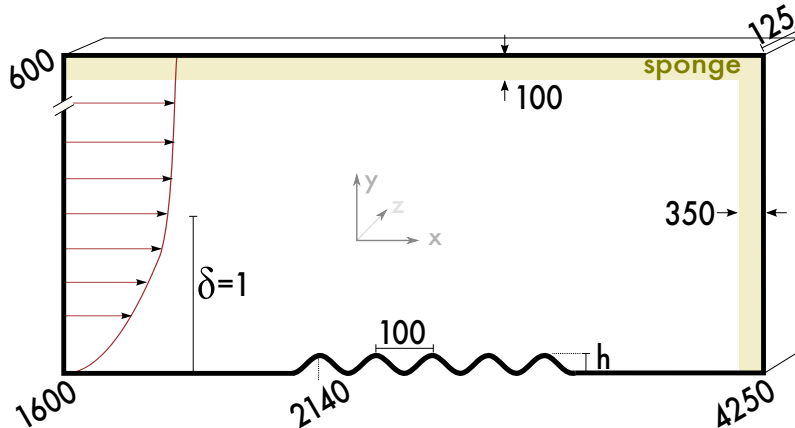
FIGURE 5.1. Characteristic features of the numerical setup for the DNS. The height of the roughness array, h, is 0.33 δ (case 1) and 0.5 δ (case 2). Figure is not to scale.

	h	T.I. [%]	Nx	Ny	Nz	Δx^+	Δy^+	Δz^+
Case 1	0.33δ	0.18	6000	350	256	16	1	16
Case 2	0.50δ	0.36	6500	350	256	14	0.8	16

TABLE 5.2. DNS grid resolution

gradients, only the high-order finite difference schemes were used herein. The set of equations is advanced in time with an explicit fourth-order Runge-Kutta scheme. At the fluid boundaries, an NSCBC (Navier-Stokes Characteristic Boundary Condition) is enforced and is supplemented by a sponge layer to dampen spurious oscillations of the finite computational domain. At the solid walls, tangential, non-slip conditions are enforced on both the flat plate and the wavy portions of the domain.The baseline code has been extensively used for shock-turbulence interaction [107, 106] and wall-bounded-flow studies [197].

5.3   Results

In the present work, we investigate, using a combination of PSE and DNS, the effects of a two-dimensional, sinuous roughness array on boundary layer transition at a freestream Mach number of 0.714. A canonical setup of a spatially-evolving, zero-pressure gradient,

flat plate boundary layer with a roughness array consisting of 5 successive sinusoidal humps (see Figure 5.2) was simulated using NPSE and DNS. In particular, we targeted a setup in which the smooth roughness resulted in a laminar-to-turbulent transition slightly downstream of the roughness patch. Thus, the roughness acts to perturb the already present T-S instabilities in the base flow without causing an immediate transition above the roughness array. This setup isolates *effects* of the roughness from the geometric complexities of the smooth roughness elements. Given the computational expense of the DNS, preliminary parametric studies using NPSE allowed us to define a geometric setup to characterize the desired transitional effects. A near perfect match of the conditions between the NPSE and DNS simulations enables a direct comparison between both computational approaches.

The main geometric features of the setup are shown in Figure 5.1; the PSE studies only considered the two-dimensional setup, while the DNS was fully three-dimensional and used periodic boundary conditions in the span-direction. The inlet consists of a Blasius boundary layer with a Reynolds number of $Re_\delta = \frac{u\delta}{\nu} = 1600$. The thickness of the inlet boundary layer, δ, is used to nondimensionalize the spatial dimensions in the computational domain. Thus, all dimensions, unless otherwise specified, are presented in terms of inlet boundary layer height. An array of five sinusoidal humps, with a peak-to-peak distance of 100, is defined, the first peak located at $x/\delta = 2140$. The Reynolds number above the roughness elements ranges from $Re_\delta = 1850$ to 2016. In the present study, two cases are considered: in case 1, the dimensionless height of the roughness array $h_1/\delta = 0.33$; in Case 2, it is $h_2/\delta = 0.50$. Both cases have slightly different perturbation amplitudes at the inlet of the DNS, as discussed later. Downstream of the roughness array, the flat plate extends up to approximately $x/\delta = 4250$. For all cases, we consider a constant wall temperature of $\frac{T_{wall}}{T_\infty} = 1$. Recall that these dimensions were selected such that the roughness does not trigger a transition, but instead causes a precocious transition downstream of the roughness array. Figure 5.2 shows an overview of the base flow obtained using Krypton's laminar solver, which is then used for the PSE calculations.

Large-scale, three-dimensional direct numerical simulations of Cases 1 and 2 are used as a comparative baseline with the NPSE results. As discussed in the previous section, a high-order finite difference scheme is used on a curvilinear coordinate system in Hybrid. The geometric dimensions of the sponge layer are shown in Figure 5.1. To resolve all scale
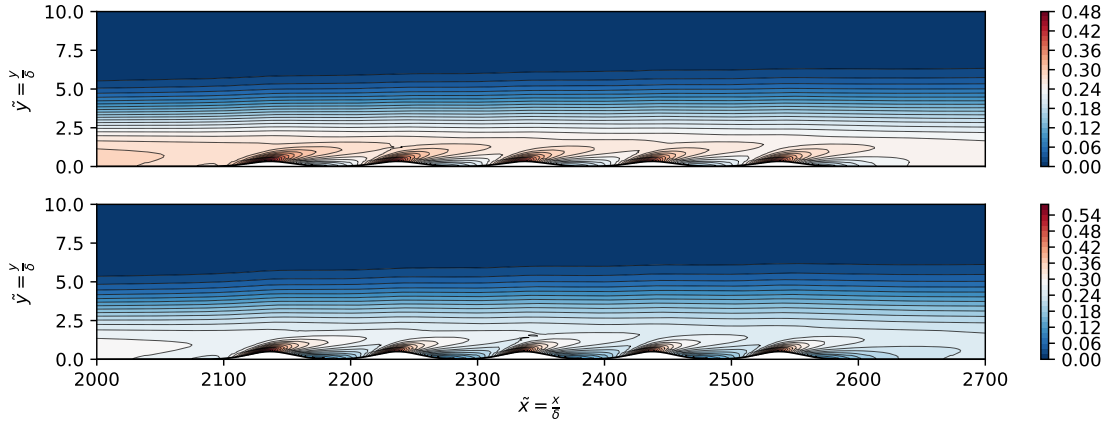
FIGURE 5.2. Vorticity contour plot of the laminar base flow for Case 1 (top) and Case 2 (bottom). The y-axis is expanded for increased visibility of the roughness elements.

of the simulation, over 537 million grid points was required with a strong grid clustering at the wall and over the roughness patch; this high resolution is required despite the very high order of the numerical scheme. The characteristics of the DNS mesh are shown in Table 5.2. The simulations, conducted on the Digital Research Alliance of Canada systems of Niagara and Narval, were run until a statistically steady transitional state was reached and the unsteady data was then averaged over 2 flow through times (we note here the very long streamwise simulation domain). In order to match the NPSE results, the freestream conditions were perfectly matched and the Blasius inflow conditions were superimposed with the two most unstable harmonic perturbations computed from the PSE results. In this section, we first present the results of the laminar PSE (LPSE) followed by the comparison of the NPSE and DNS results.

5.3.1 Linear modal stability analysis

The growth rate can be seen as a mode-specific measure of flow stability [72] that combines the effect of two components: first, the growth of the phase function χ and second, the growth of the amplitude function $\hat{q}$. Here, we use the definition from [86], to define growth

83

σ:

$$\sigma = -Im(\alpha) + \frac{\partial}{\partial x}\left[\ln\left(\sqrt{E_k}\right)\right] \qquad E_k = \int_0^\infty \overline{\rho}\left(|\hat{u}|^2 + |\hat{v}|^2 + |\hat{w}|^2\right) dy \qquad (5.17)$$

In linear PSE (LPSE), as the modes do not interact, we can only investigate the stability of the system for a range of individual perturbations. Figure 5.3 shows the impact of the roughness array on the local growth rate for a range of frequencies with LPSE. The solid line corresponds to the neutral stability curve and delineates the instability regions, in other words, the regions of positive growth. The red areas represent unstable regions, whereas the blue areas indicate where the instabilities are damped. As expected, the convex regions of the roughness array tend to destabilize the flow, while the concave regions cause a re-stabilization. The height of the humps mostly impacts the bounds of the stability region, since slightly higher frequencies undergo local growth in the convex regions. More specifically, growth is maximum when $v = 0$, which happens slightly past the crest of each hump. The same effect is observed slightly downstream of the roughness array, near $\tilde{x}/\delta \approx 2700$, in Figure 5.4; in this so-called *recovery zone* where all modes experience a higher growth rate. In their experiments on smooth roughness elements, [96] observed that the immediate zone after a roughness array was significantly more unstable than a Blasius flow. However, they theorized that this effect was mainly driven by nonlinear interactions. Here, we observe a destabilizing effect at all frequencies in the linear analysis, yet the higher modes remain damped in the recovery zone. In Section 5.3.2, we will see that although the amplification of the higher modes is increased in the recovery zone, this effect cannot be explained solely by nonlinear interactions.

Unlike linear stability theory, in the NPSE approach, particular attention should be paid to both the relative and absolute initial amplitudes of the modes. Indeed, in the nonlinear theory, the modal response of the perturbation is intrinsically tied to the boundary layer properties through the MFD. If the MFD is neglected, assuming that the relative amplitude between the modes remains the same, the solution is simply scaled by the initial conditions. Here, we account for the MFD. To generate the initial conditions, we must first identify the fundamental mode (or the most unstable mode) and its harmonics. To this end, in the LPSE, we used the so-called *n-factor*, obtained by integrating the growth rate along the

84
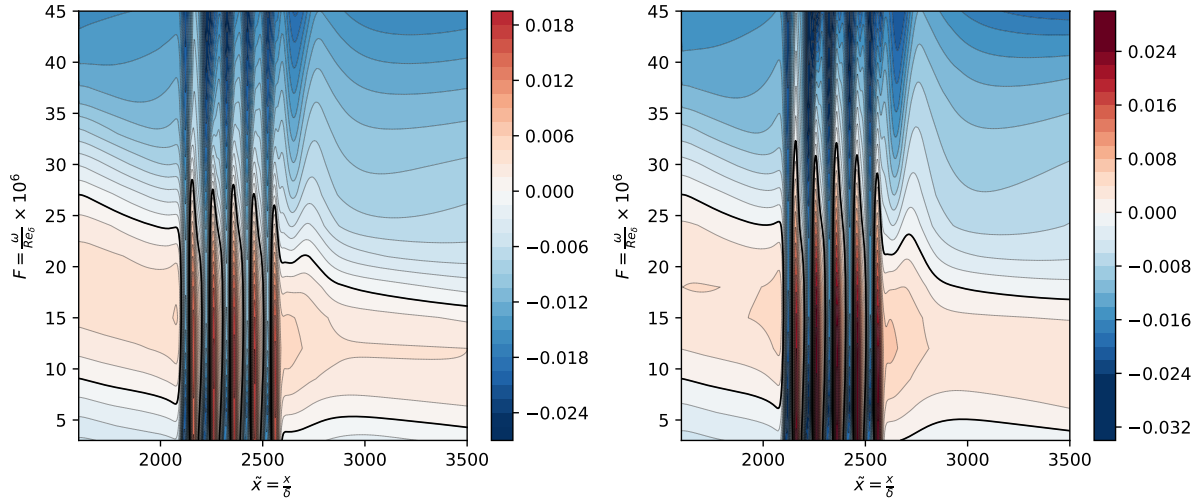
FIGURE 5.3. Neutral stability map for Case 1 (left) and Case 2 (right). Solid line indicate neutral stability ($\sigma = 0$).
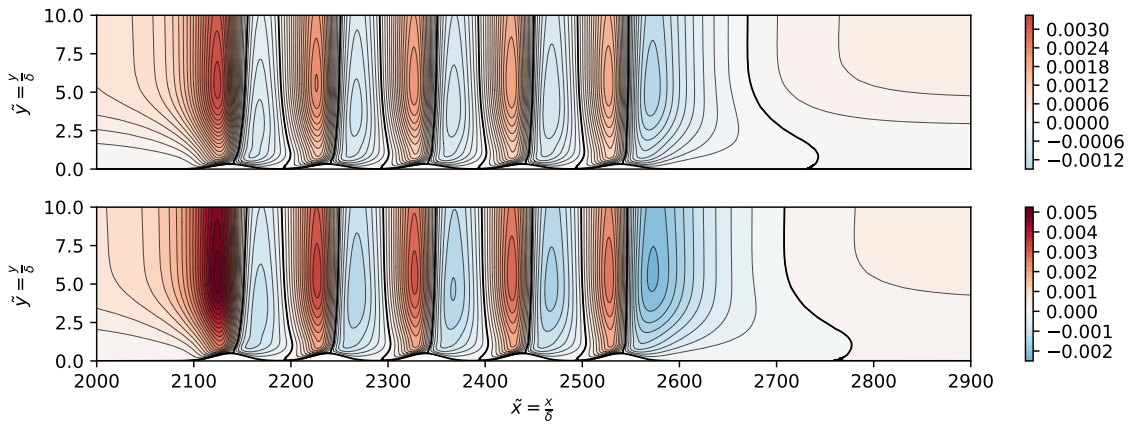
FIGURE 5.4. Normal velocity contour plot of the laminar base flow for Case 1 (top) and Case 2 (bottom). The solid line indicates V=0
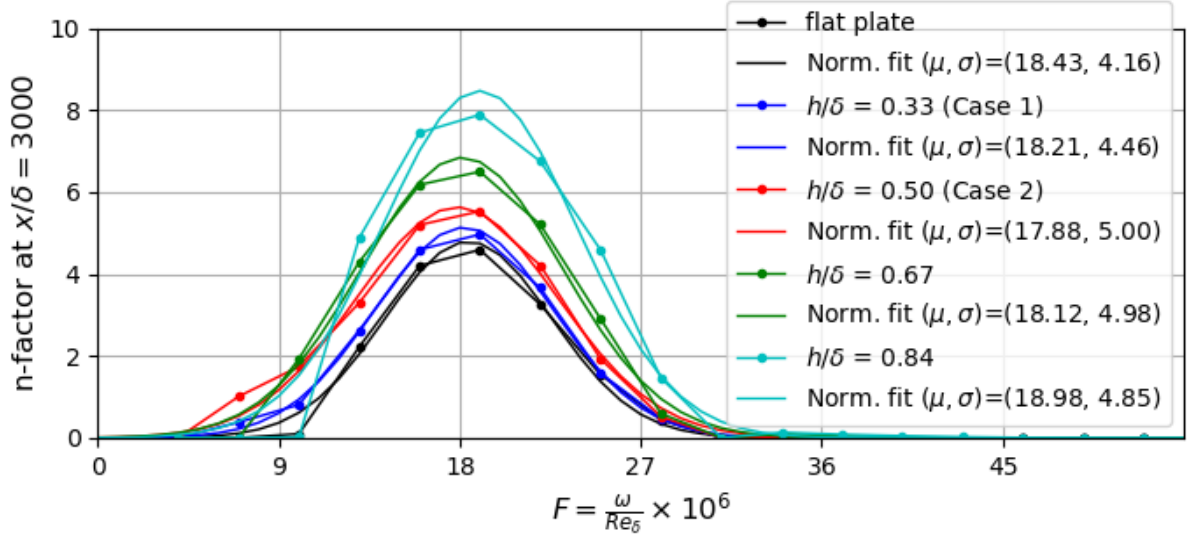
FIGURE 5.5. Maximum amplification ratio for a range of dimensionless frequencies and different roughness heights $M = 0.714$, $Re_\delta = 1600$, $\frac{T_{wall}}{T_\infty} = 1$

streamwise direction:

$$\text{n-factor} = -\int_{x_0}^{x_i} \sigma dx \qquad (5.18)$$

The n-factor curves represent a mode-specific measure of the disturbance amplification along the stream path. Figure 5.5 presents a sensitivity analysis of the maximum n-factor downstream of the roughness array, for a range of frequencies and roughness heights. As shown in Figure 5.5, the height of the roughness array only has a limited impact on the frequency of the most unstable mode, at least for the roughness heights studied herein. In other words, in Cases 1 and 2, the destabilizing effect of the roughness array only impacts the ratio of amplification of the perturbations while the frequency of the most unstable mode remains unchanged. At a higher roughness amplitude of $h > 0.84\delta$, we observe a slight increase in the frequency of the most unstable mode, but further investigations would be needed to see if the trend continues. A more general stability indicator was introduced by [80] with the concept of *N-factor* corresponding to the envelope of the n-factor curves, i.e. the n-factor of the most unstable mode at a given position. Based on this concept, [80]
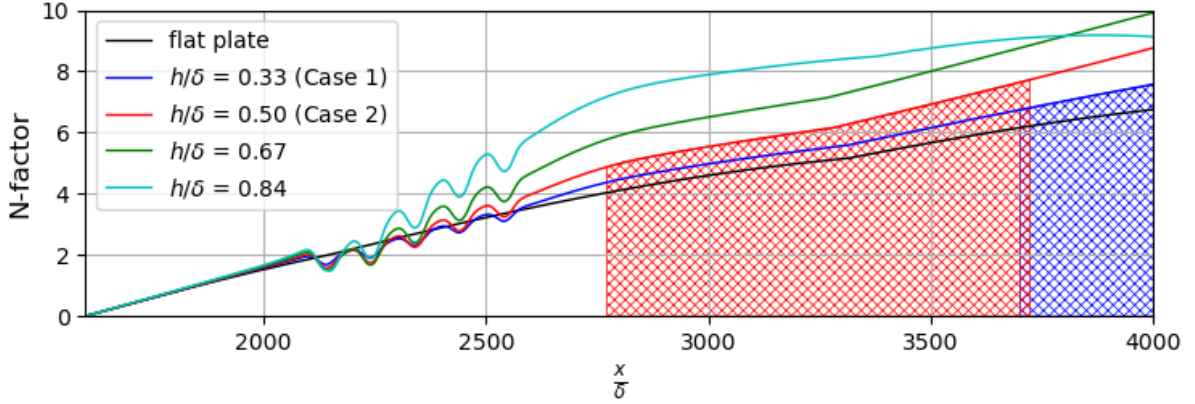
FIGURE 5.6. N-factor curve for different roughness amplitudes. The hatched area correspond to the expected transition location for case 1 and 2, based on equations (5.19) and (5.20).

developed the e^N method and, later, the *enhanced* e^N method [81]. Both methods are based on the same premise that the transition location, obtained experimentally, is correlated to a critical N-factor value obtained with the linear modal stability theory. Indeed, the method is tied to the geometry and flow regime of the experiments but can nonetheless be used as a first approximation of the transition location. For an incompressible Blasius flow, the enhanced e^N method [81] predicts that the transition should begin (N_B) and end (N_E) once the N-factor reaches certain thresholds, given by:

$$N_B = 2.13 - 6.18 \log_{10}(Tu) \tag{5.19}$$

$$N_E = 5.00 - 6.18 \log_{10}(Tu) \tag{5.20}$$

According to (5.20), in the current configuration, we expect that the transition should occur in a region where the N-factor is in the range of $N \in [6.7, 9.6]$ and $N \in [4.9, 7.7]$, for Cases 1 and 2, respectively. Figure 5.6 shows the curve of the N-factor for various heights of roughness and the expected transitional region for Cases 1 and 2.

87

5.3.2 Nonlinear modal stability analysis

In the classical NPSE approach, perturbations are discretely represented by a fundamental mode and their harmonics (e.g. $1F$, $2F$, $3F$, etc.). However, because of the presence of viscosity, any disturbance will experience, to various degrees, spectral diffusion. At some point, nonlinear interactions will eventually generate side lobes, and the discrete formulation assumption will gradually become less accurate. This effect was reported by Kuehl [100, 92] who quantified that the nonlinear feedback is overestimated by approximately 70% when using the discrete representation compared to the finite-bandwidth approach. Here, we use the finite-bandwidth formulation described by [100] with the normal function bandwidth.

Due to the vanishing velocity and temperature fluctuations at the isothermal wall, the fluctuating wall pressure must be nonzero in order to satisfy continuity and avoid a trivial solution. Thus, since $\hat{p}$ is the only non-homogeneous variable in the system, setting the inlet turbulence intensity comes down to imposing a different fluctuating wall pressure, coupling two of the important variables in the system. Since the amplitude of $\hat{u}$ depends on $\hat{p}$, the incoming turbulence intensity can only be known *a posteriori*. The amplitudes of the initial fluctuation for the two cases are given in Table 5.3 and correspond to the finite-bandwidth area of the perturbation. The incoming flow consists of the superposition of the laminar base flow and 2 T-S waves of frequencies F and $2F$. The base flow field in the NPSE is initialized following the procedure proposed by [100]. The mode F has a bandwidth $\sigma_F = 4.5$ while $\sigma_{2F} = \sqrt{2}\sigma_F$, or, equivalently $\sigma_\omega = 0.0072$ and $\sigma_{2\omega} = 0.01018$. The perturbation is decomposed into 16 sinusoidal modes with $\Delta\omega = 0.0072$. Taking advantage of the Hermitian symmetry, the mode-specific RMS value corresponds to $\sqrt{2}|\hat{u}|_{max}$ and thus, the total disturbance RMS value and turbulence intensity are given by:

$$u'^2_{rms} = 2\sum_{n=0}^{N}|\text{Re}(\hat{u}_n)|^2_{max} \tag{5.21}$$

$$\text{Tu}[\%] = \sqrt{\frac{2}{3}\left(u'^2_{rms} + v'^2_{rms} + w'^2_{rms}\right)} \tag{5.22}$$

	F	$2F$	Tu [%]
Case 1	1e-4	5e-5	0.18
Case 2	2e-4	1e-4	0.36

TABLE 5.3. Initial amplitude of the fluctuation, normalized by $\hat{p}_{wall}$, for the case 1 and 2. The values correspond to the finite-bandwidth area of the perturbation. $F = \frac{\omega}{Re_\delta} = 18$.

.
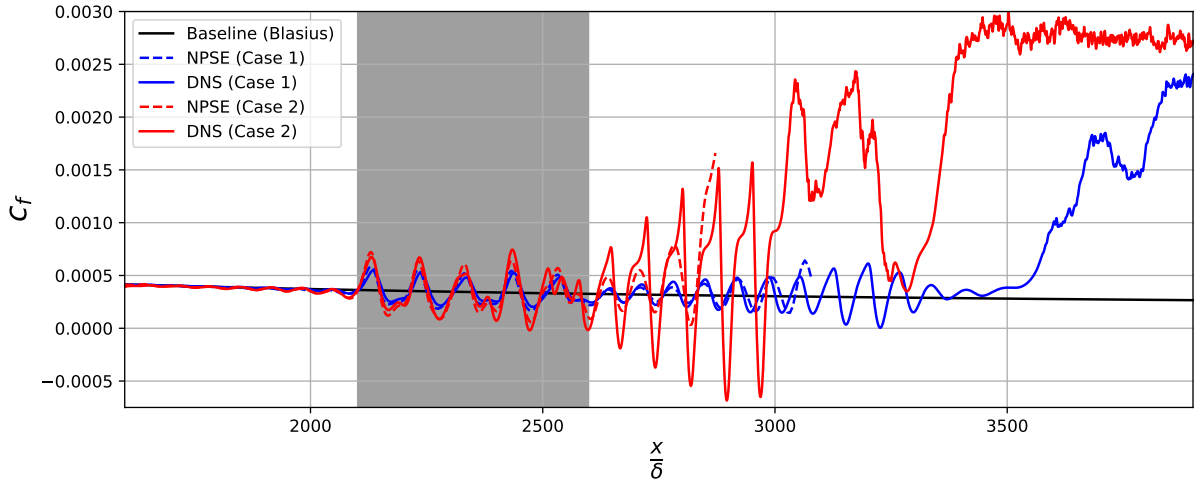
FIGURE 5.7. Skin friction coefficient obtained from the NPSE solver compared against Direct Numerical Simulations (DNS). The gray area corresponds to the location of the roughness array.

The methodology used to analyze the nonlinear PSE is quite different from linear analysis. In fact, since the amplitude of the modes is known, it is possible to reconstruct the fluctuations ϕ', and analyze the results in a way similar to a DNS. That is to say, we can reconstruct local indicators such as the wall friction coefficient (c_f), wall pressure, and vorticity. For example, Figure 5.7 shows a comparison of the friction coefficient of the wall skin obtained using NPSE and DNS. Regarding case 1, we denote a good agreement between the c_f estimated from the NPSE and the DNS. Although this is expected, since both the amplitude of the fluctuations and the height of the roughness array are relatively small. Nevertheless, it is a good indicator that the PSE remains valid even in presence of wall curvature. For case 2, we note a close agreement between the NPSE and DNS

89

until the amplitude of the fluctuations becomes sufficiently large to induce a periodic flow reversal identified by a negative friction factor from $x/\delta > 2490$. The fact that flow reversal arises might rightfully raise some concerns regarding the validity of the PSE since the solution is sought using a marching procedure in which the information can only travel downstream. Nevertheless, if the flow reversal is caused by the harmonics themselves, the information contained in the *wavefront*, is still progressing and the PSE remains valid. In fact, [73] conducted a linear PSE-based stability analysis in separated flows and concluded that, unless the reverse flow velocity is greater than the phase speed, the PSE is still applicable. In the case of NPSE, we must also account for the *stationary* MFD, which represents the modification of the base flow due to the effect of nonlinear interactions. Therefore, if the phase speed of the fluctuations remains greater than the mean flow, i.e. if $\frac{\omega}{\text{Re}(\alpha)} > u_{lam}(x,y) + u_{0,0}(x,y)$, the NPSE remains valid. Here, this condition is met for both Cases 1 and 2. Thus, the fact that the friction coefficient computed from the NPSE begins to deviate from the DNS when the flow is reversed is not tied to the validity of NPSE and should rather be seen as an early indicator of the rapid growth of higher frequency modes. These modes, characterized by sharp spikes in the skin friction coefficient downstream of the roughness array, are addressed in the next section.

To better quantify the dominant instability frequencies, a one-dimensional Fourier decomposition of the skin friction coefficient at various sections along the wall is shown in figure 5.8 for both the NPSE and DNS. In order to distinguish the signal from the laminar friction associated with the geometric wavelength of the roughness array, only the c_f of the fluctuating flow was used. Figure contains valuable information on the amplitude and spectral evolution of the disturbances. First, we see that, in both cases, the frequency content of the perturbations, in the region preceding the roughness array, contains a dominant peak, centered at $F = 18$, and a second mode with a larger bandwidth near $F = 36$, which are tied to the imposed T-S perturbations at the inlet. At this point, the modes evolved linearly; the dominant mode was amplified, while the second mode was damped but remains distinguishable in the Fourier decomposition. So far, the agreement between the NPSE and DNS is good in both cases. Now, moving downstream of the roughness array, the blue curves reveal the emergence of a third higher frequency peak near $F \approx 39$, which corresponds to the frequency associated with the wavelength of the roughness ar-

ray. This peak, visible in both cases but more prominent in case 2, is almost absent of the NPSE signals. At first glance, one could think that this is due to the inadequacy of the discrete spectral representation–inherent in the modal stability theory–to study the process of frequency band generation. However, for several reasons, we think that this is not the case. First, we use a finite-bandwidth approach which considerably enhances the study of spectral broadening and frequency band generation [100]. Second, the spectral widths of the first and second harmonics predicted by the NPSE agree well with those of the DNS, indicating that the spectral broadening is probably well estimated by the NPSE. Third, the high-frequency content seems to increase with the height of the roughness array, leading us to think that the phenomenon is intimately tied to the curvature of the wall rather than spectral interactions. Yet, surface roughness tends to generate stationary, often spanwise-varying, disturbances which can be adequately described by the transient growth framework [152]. Transient growth may be defined as a rapid change of the fluctuating energy resulting from the interactions between stable nonorthogonal modes [45]. It has been suggested as a possible route for several cases of bypass transition, many of which feature discrete roughness elements [210, 141, 45, 152]. The MFD, quantifiable by the difference between the time-averaged and the laminar base flow, is a form of streamwise-varying stationary disturbance. Although neglected in the present study, the stationary spanwise periodic modes (i.e. $(m, 0)$) is another example of a periodic stationary disturbance. Figure 5.9 shows the time and span-averaged wall friction coefficient compared with the laminar base flow and MFD of the NPSE calculations. We see that the roughness array seems to promote the formation of stationary disturbances, particularly in regions of high curvature, near the peaks and troughs. Once corrected by the MFD, the laminar friction approaches the time-averaged DNS results, especially downstream of the roughness, where the growth of the MFD is mostly driven by the increasing nonlinear interactions. We observe that both the DNS and the NPSE predict some spatial oscillations before the onset of turbulence, but it seems that their amplitude and frequency are not quite the same. While studying the effect of a smooth hump on hypersonic boundary layer instability, [144] noted a phase synchronization of the mode S and F downstream of the humps. Their analysis was conducted using the LST and thus in this context, the phase synchronization does not have a physical meaning. In the nonlinear PSE, the phase synchronization, promoted by

91
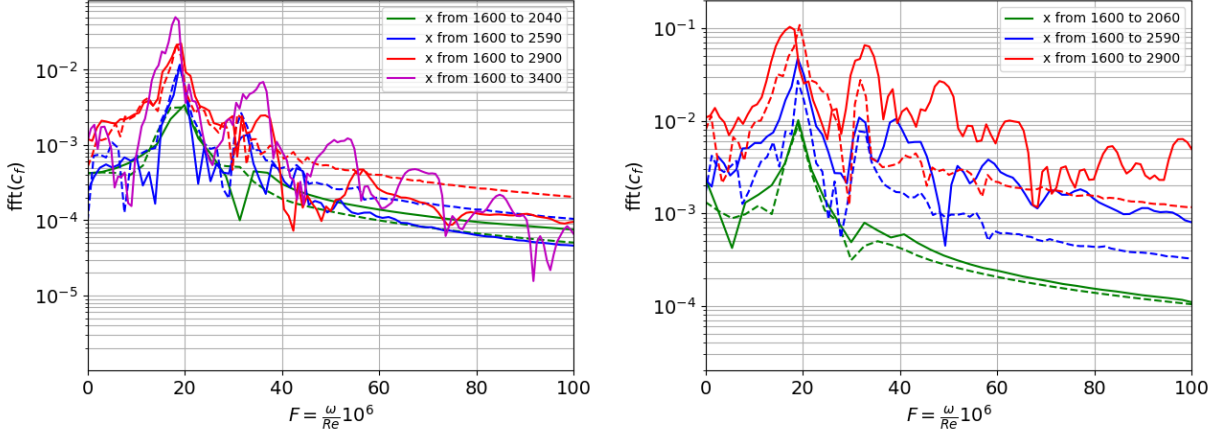
FIGURE 5.8. fft(c_f) at different regions for Case 1 (left) and Case 2 (right). Solid line is obtained from DNS and the dashed line from the NPSE. We used the c_f of the fluctuations

the presence of curvature could induce oscillations in the nonlinear forcing term, and, in turn, lead to spatial oscillations in the MFD. The observed difference in amplitude and frequency between the DNS and NPSE could very well be related to the optimal growth of spanwise instabilities inside and downstream of the roughness array. In this respect, in the next section we show how the vortical structures develop and eventually breakdown to turbulence downstream of the roughness array using the high-fidelity DNS data.

5.3.3   Transitional coherent structures

Figure 5.10 shows the isosurface of the Q-criterion (case 1), colored by the magnitude of the velocity. The structures identified by Q-criterion are overlaid on the wall, which is colored by the temperature at the plane of $y = 0.2\delta$, this highlights the near-wall streaks. As we can see, the T-S structures remain virtually unaffected by the presence of the roughness array until very far downstream (recalling the roughness array ends at $x/\delta = 2540$). The first sign of the onset of transition is seen around $x = 3620\delta$, and the transition occurs over a range of $\Delta x \approx 200\delta$. The transition is immediately preceded by what resembles streamwise streaks, visible in the temperature field, which are generally associated with a K- or H-type transition [77], depending on their alignment. These streaks are, however,

92
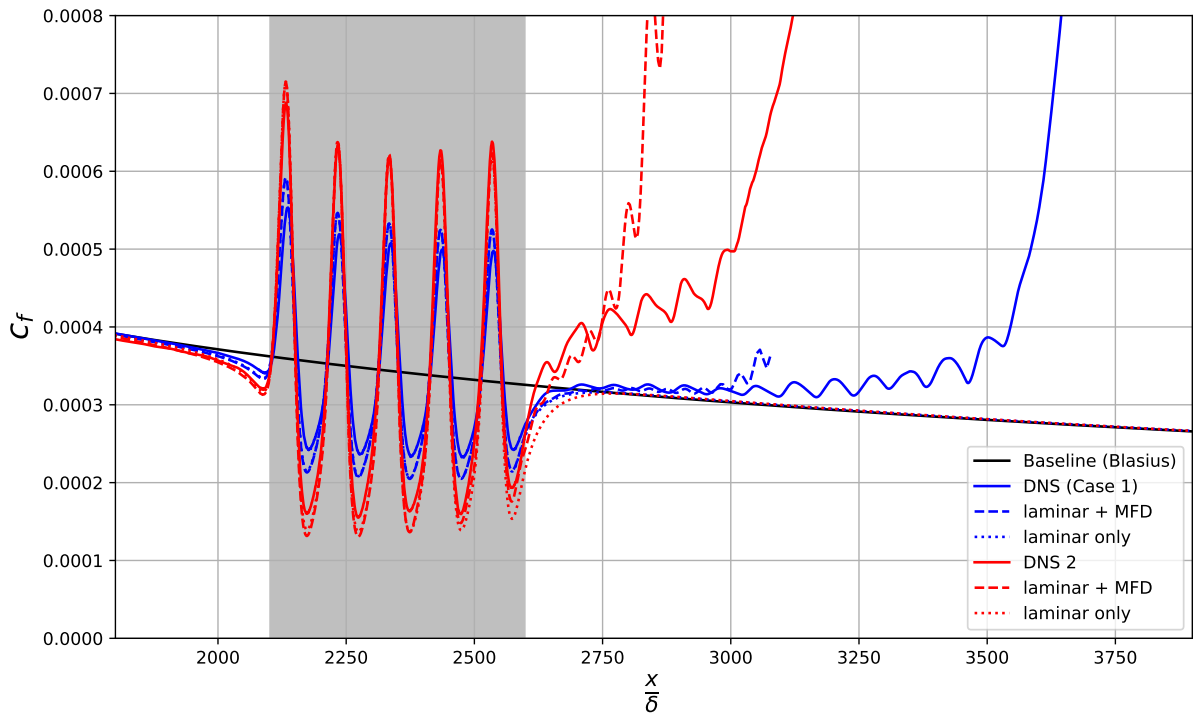
FIGURE 5.9. Time-averaged wall skin friction coefficient obtained from the Direct Numerical Simulations (DNS) and compared with the NPSE results. The gray area correspond to the location of the roughness array.
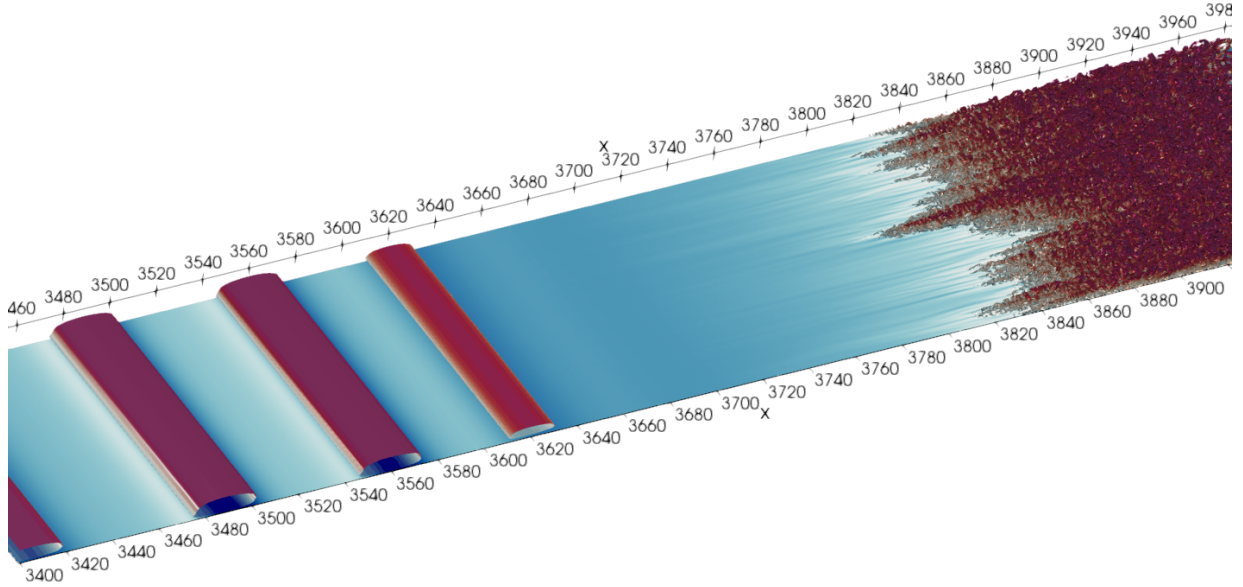
FIGURE 5.10. Iso-surfaces of Q-criterion (10^{-3}) coloured by contours of streamwise velocity, the wall is colored by the temperature at $y = 0.2\delta$ (Case 1)

quite short, unlike those observed in [215], and bypass the formation of typical K or H structures. The transitional patterns of Case 1 and Case 2 are surprisingly different from each other despite their similarities in terms of geometry and flow conditions. Figure 5.11, shows the isosurface of the Q-criterion, colored by the magnitude of the velocity at different time steps, for case 2. As seen in Figure 5.11, the recovery zone downstream of the roughness array is still dominated by the presence of 2D T-S waves. At this point, their amplitude is sufficiently high to induce a flow reversal in the vicinity of the wall. The first turbulent spots appear near $x = 3000\delta$ where vortical structures begin to interact with the edge of the boundary layer, bypassing the normal (H-type) transition process that we would have expected without the presence of roughness. The growth of these structures occurs over a relatively short distance of approximately half the wavelength of the dominant mode; consistent with the results from Figure 5.8. From a modal stability standpoint, under current flow conditions (Reynolds and Mach numbers), all modes with a frequency $(F > 30)$ are linearly stable over the roughness array (see Figure 5.3), and thus

94

their growth can only be sustained by nonlinear interactions or a significant modification to the base flow. In this regard, higher frequencies are generally the most strongly affected by the MFD. Thus, other types of stationary disturbance, such as span-periodic disturbances, could very well favor the early emergence of these secondary instabilities.

Interestingly, this transition path is not the only one in play, as we observe a cyclical transitional pattern driven by the rise of both two-dimensional secondary instabilities and lower-frequency T-S instabilities. For instance, we denote the presence of T-S waves further downstream, near $x/\delta = 3200$. These T-S waves gradually wrinkle and develop a spanwise periodicity featuring aligned Λ-vortices near $x/\delta = 3300$, typical in the K-type transition scenario. As discussed in [215], [97] had already made the connection by associating the term 'bypass' to the emergence of a secondary instability of natural transition. The shift from 2D to 3D instabilities was gradual and occurred over a distance of approximately $\Delta x \approx 250\delta$. Figure 5.12, displays the evolution of a typical vortical structure starting near $x/\delta = 3000$, at different time steps ($\Delta t = 50$). In the span direction, we count approximately 5.5 wavelengths, over a span distance of 125δ, which corresponds to a dimensionless spanwise wavenumber ($B = \frac{\beta}{Re_\delta} \times 10^6$) in the range of 25-30. It is generally assumed that at subsonic conditions, the most unstable mode is the two-dimensional T-S wave (spanwise wave number $B = 0$). This knowledge guided our decision to use this perturbation at the inlet of our domain. However, in light of these DNS results, we ran additional LPSE simulations with different spanwise wavenumbers in order to ascertain this assumption. Figure 5.13 reveals that the mode experiencing the highest linear growth inside the roughness array is the two-dimensional mode ($B = 0$) while the most amplified mode is, in agreement with the DNS, a three-dimensional mode $B = 25$. The mode $B = 0$ experiences both the highest growth and simultaneously the largest damping, depending on the local pressure gradient; this mutually cancelling effect allows for the growth of 3D instabilities. The highest growth occurs in the regions with the highest concavity and may therefore be related to the emergence of a Görtler instability. Another interesting finding is that this effect is observed early in the domain, upstream of the roughness elements, where the pressure gradient is already slightly favorable; due to the subsonic nature of the boundary layer flow, we observe a very slight pressure rise ahead of the roughness patch. This is consistent with the trend observed in the roughness array suggesting that
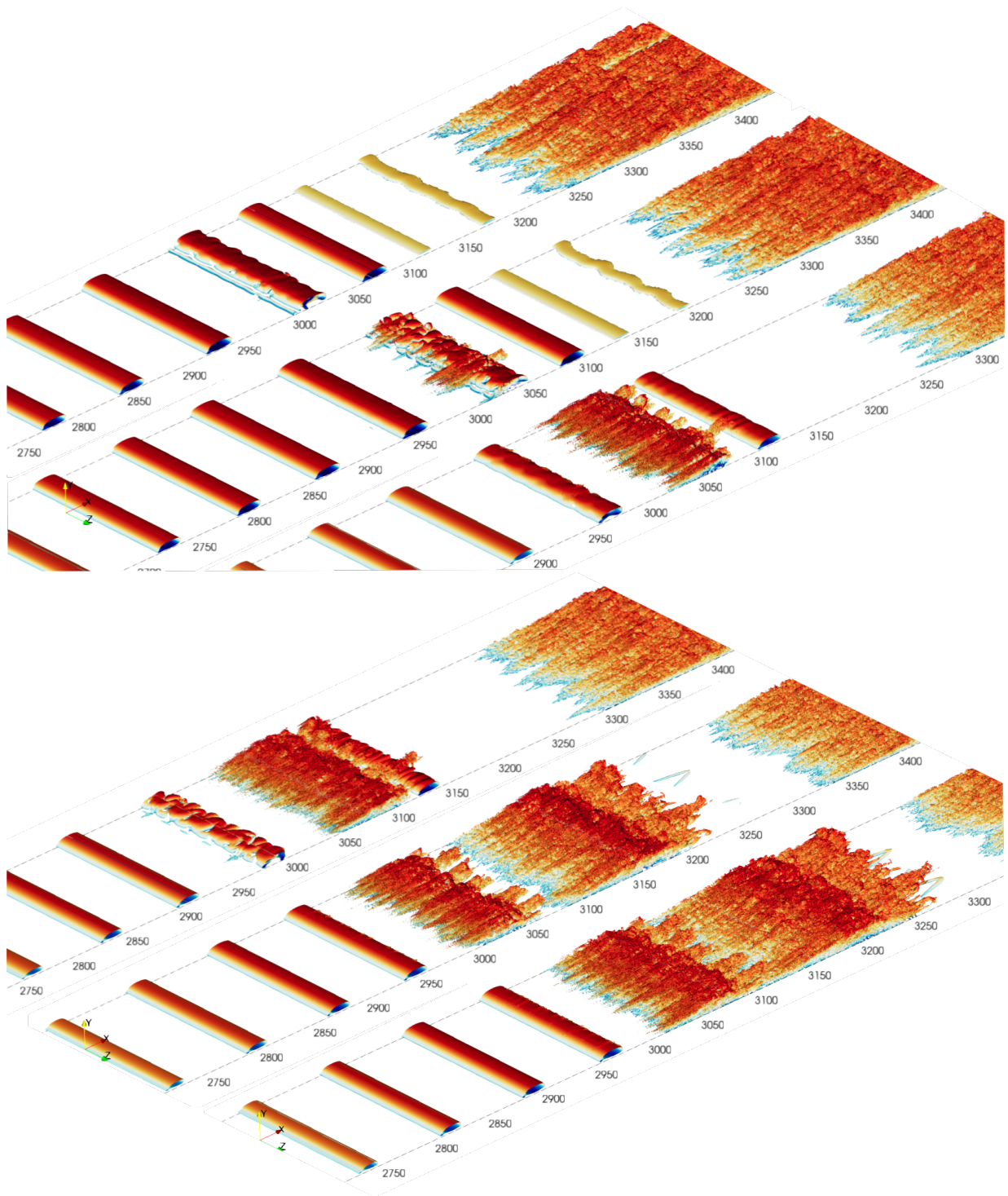
FIGURE 5.11. Iso-surfaces of Q-criterion (10^{-4}) coloured by contours of streamwise velocity at different time steps $(\Delta t = 50)$

96
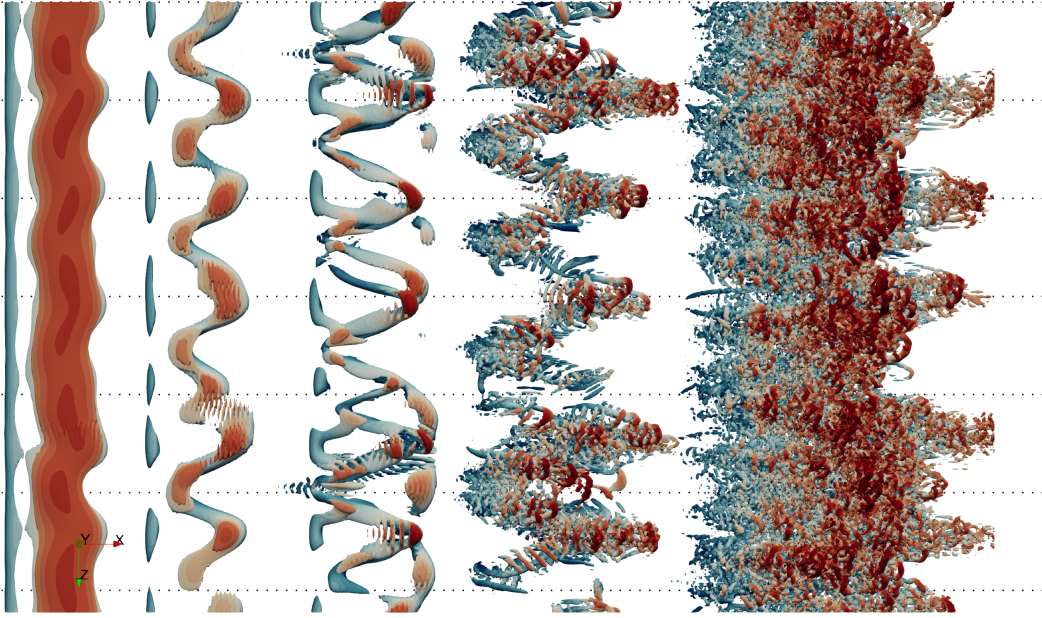
FIGURE 5.12. K-type structures near $x/\delta = 3100$. Iso-surface of Q-criterion (10^{-3}), colored by the velocity magnitude (Case 2). Flow direction: left to right. The sequence follows the evolution of a given structure at different time-steps $(\Delta t = 50)$, from $x/\delta \approx 3100$, to $x/\delta \approx 3300$. The horizontal spacing is not representative of the distance travelled between the time-steps. The width (span-direction) is 125δ
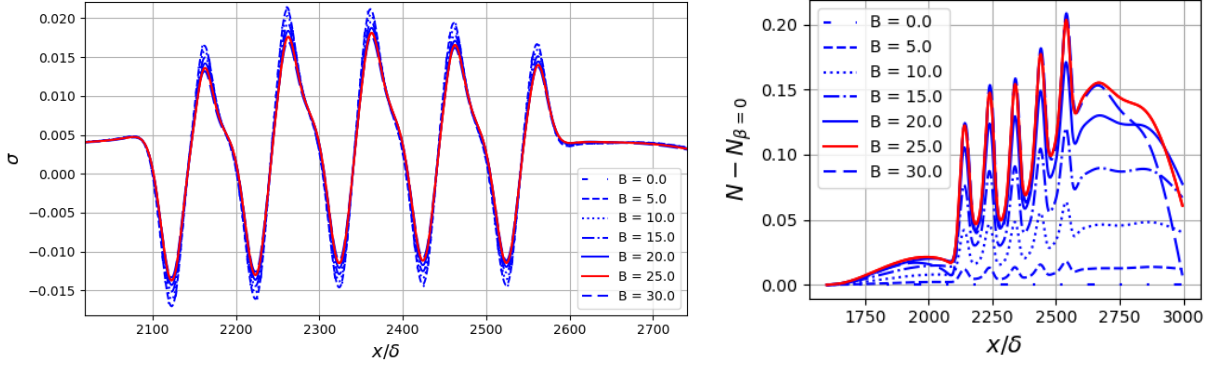
FIGURE 5.13. Local growth rate in the roughness array (left) and comparative N-factor curves (right) for $F = 18$ and a range of span-wise wavenumbers B. The red curves correspond to the most unstable mode $F = 18, B = 25$.

the 3D instabilities are less affected by the damping effect of the slight favorable pressure gradients.

This shift between 2D instabilities toward the most preferred spanwise periodic disturbance was highlighted by Kang, although in the opposite direction, who studied the combined effects of amplitude, frequency, and bandwidth on wavepackets in incompressible laminar turbulent transition a over flat plate [90]. The DNS conducted by Kang revealed that, depending on the frequency content of the incoming fluctuations, some cases exhibit a continuous or abrupt shift in the dominant frequency toward the 2D frequency of the lower branch. Kang speculated that the mechanism behind frequency shifting was caused by a linear process driven by the large difference in growth between the modes at play. Here, the difference in growth is small, almost marginal, and the frequency change is continuous and very gradual. Looking at the root mean squared of the streamwise fluctuation profiles at different locations, we can better interpret how the instabilities evolve over and downstream of the roughness array. Figure 5.14 shows the u'_{rms} profiles in the troughs of the roughness array. The solid lines come from the NPSE calculations, while the crosses indicate the DNS. The first profile was taken just before the roughness array, at $x = 2044\delta$. At this location, in Cases 1 and 2, the DNS and the NPSE predict very similar RMS profiles (amplitude and shape), indicating a nearly typical 2D modal growth. In case 1, the

agreement remains until the end of the roughness array, highlighting the good performance of the PSE in the presence of compressibility effects and moderate curvature. In case 2, the results are mixed. The shape and amplitude of the RMS profiles computed from the NPSE and the DNS tend to gradually differentiate themselves as the perturbations advance downstream. At $x = 2189\delta$, the RMS profile extracted from the DNS already shows a significant change in shape, compared to the RMS profile obtained with the NPSE. At this point, the amplitude of the higher modes is negligible, as shown in Figure 5.8, and cannot explain the difference in amplitude observed in Figure 5.14. Although not shown here, we tried to run the NPSE using the same temporal frequency content, but with a spanwise wavenumber of $B = 25$, to see if we could see any improvement in the shape or amplitude of the RMS profiles. The increase in the growth rate was marginal and led to similar amplitudes. We also tried with a range of five spanwise modes to see if the nonlinear response would trigger the growth of 3D instabilities, but it also led to similar outcomes.

Interesting work by [142] on the growth of optimal disturbances in hypersonic boundary layers provides a relevant starting point for the investigation of transient growth in the context of the modal stability theory. In his approach, Paredes uses the adjoint-PSE to determine the disturbance that leads to the maximum energy amplification at a certain point. This approach could provide a comprehensive framework to study the gradual passage from 2D to 3D instabilities observed in case 2. However, the coexistence of two transitional mechanisms characterized by the presence of both early 2D secondary instabilities and unstable K-type structures further downstream is in contradiction with the main ansatz of the method, i.e., that the path leading to transition is intimately tied to the growth of one optimal disturbance [187].

Alternatively, [36] studied the global energy balance in unstable boundary layers and found that, at a sufficiently high disturbance level, a two-dimensional flow will establish a catalytic feedback loop that leads to simultaneous growth of two-dimensional and three-dimensional waves, bypassing the classical T-S mechanism [71].
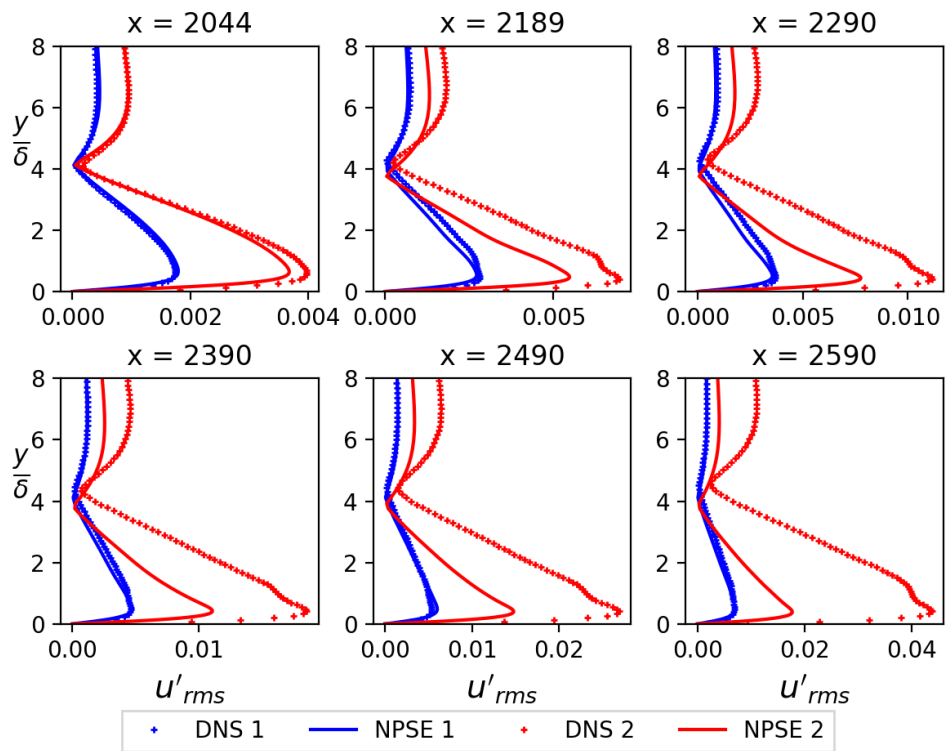
FIGURE 5.14. Root mean squared of stream-wise velocity profile in the roughness array, taken at minimums (valleys)

5.4 Conclusion

Numerical studies of a compressible laminar boundary layer in a normal transition scenario (T-S waves) were performed using a combination of parabolized stability equations (PSE) and Direct Numerical Simulations (DNS). A smooth roughness patch, consisting of five sinusoidal two-dimensional humps, was added to a zero-pressure gradient flat plate boundary layer in order to induce early transition. A parametric study was done to identify a physical setup in which transition takes place downstream of the smooth roughness array. The downstream transition in the setup allows a decoupling of the geometric complexity of the roughness array from the transition process. Two cases, with varying waviness amplitude, were studied using large-scale DNS. The main effect of compressibility is to dampen the growth of instabilities by reducing the inflection of the velocity profile in the vicinity of the wall. This effect is, however, marginal in region of high curvature as the height of the roughness array induces a stronger inflectional instability. In the case featuring the lowest roughness amplitude, the streamwise velocity profiles over the roughness array predicted by the NPSE were in good agreement with the DNS, indicating that it could be used as time-dependent boundary condition for DNS, DES or LES in order to reduce the size of the computational domain. In the second case, featuring higher humps, the results are mixed; the DNS suggests that strong curvature favors the nonmodal growth of higher-frequency modes. The linear modal analysis reveals that although the two-dimensional instability experiences the highest growth rate, it also experiences the largest damping in the regions of locally favorable pressure gradients. This mutually canceling effect allows for the growth of 3D instabilities, which are overall less impacted by the presence of curvature.

Despite the nearly identical setups, cases 1 and 2 showed surprisingly different transitional mechanisms. Case 1, with a lower roughness amplitude, had a well-defined transition path, similar to the main features of the classical T-S mechanisms. Case 2, with a slightly higher roughness amplitude, displayed a cyclical transition pattern that periodically shared features of the T-S mechanism and secondary instability bypass mechanism.

Chapter 6

Boundary layer stabilization via thermodynamic roughness

This chapter has been adapted from Francis Lacombe and Jean-Pierre Hickey. "Boundary layer stabilization via thermodynamic roughness," Physical Review Fluid, 2022 (to be submitted).

Abstract

The coupling effect between roughness and temperature strips is investigated at transonic condition (Ma = 0.714) using the nonlinear parabolized stability equations (NPSE). The NPSE-based parametric study confirms the stabilizing effect of cooling strips and the destabilizing effect of heating strips on the stability of T-S waves in the zero-pressure gradient (ZPG) flat plate boundary layer. The effect of a smooth roughness patch, consisting of five sinusoidal two-dimensional humps, is added to the zero-pressure gradient flat plate boundary layer to study the coupling effect between roughness and wall temperature. The temperature strips and the roughness elements are located after the onset of instability (branch I) and extend for 500δ. Both the heating strips and the roughness patch are defined using the same mathematical expression. The analysis reveals a catalytic coupling effect between the temperature strips and roughness that could help improve temperature-based active laminar flow control devices.

6.1 Introduction

Drag reduction in aerospace is one of the main drivers of technological innovation. By delaying the transition to turbulence, thus increasing the laminar footprint over the body, a favorable reduction of the frictional forces can be obtained which directly translates into improved operational efficiencies for the aircraft. Although it is desirable to delay transition to turbulence, a robust, resilient, and energy efficient approach to stabilize the boundary layer remains technically difficult to achieve. A number of physical mechanisms can be used to stabilize the boundary layer; to this end, natural laminar flow (NLF) design has shown the potential to deliver significant drag reduction. By considering the pressure distribution on the wetted surface during the design stage, engineers can adjust the favorable pressure gradients in specific regions to stabilize the boundary layer, thus naturally delaying the transition. NLF design considerations have been applied to airfoil shape optimization in a number of works [46, 68]. Although the potential for significant improvements through NLF is acknowledged, cross-flow-driven instabilities, which dominate swept wings or nacelle transition, often limit the efficacy of the stabilizing effects of favorable pressure gradients [26].

Although more complex than NLF, Laminar Flow Control (LFC) is another paradigm to delay transition, which seeks to increase the resilience of the boundary layer to transitional instabilities through active or passive means. Active flow controls have also shown a very significant potential in delaying the boundary transition through the use of synthetic jets and plasma actuation (e.g. [102]). Similarly, boundary layer suction targets inflectional instabilities in the base flow, although it has been shown to be most effective in low-Mach number regimes [119]. Recent numerical and experimental works showed the promise of transpiration-aided drag reduction [70]. The slow adoption of active laminar flow control approaches is attributable to the relative mechanical complexity of the systems and the often unfavorable integrated energy balance. In this regard, *passive* laminar flow control approaches remain particularly attractive. Bio-inspired leading edge design [55] or riblets [17] have been utilized as passive flow control mechanisms that target the modification of energetic turbulent structures in the boundary layer. These approaches tend to have a small operational window, which can result in an enhanced drag outside of the target range.

On the transitional side, Zahn [217] highlighted that surface imperfections, such as a deep gap, could result in a standing acoustic wave that can be tuned to dampen T-S modes in transitional flows. A more recent paradigm to delay transition combines both NLF and LFC. The premise is to supplement the pressure gradient-based design with a laminar flow control approach; this combined approach is often referred to as Hybrid Laminar Flow Control (HLFC). HLFC has been used for several decades [9] with sustained promise.

Boundary layer control through localized heating or cooling represents one of the classical approaches to active flow control, which targets the instability modes and are therefore less invasive to the base flow characteristics. As localized heating or cooling only slightly modifies the local density and viscosity, it imparts a modest modification to the boundary layer compared to more aggressive flow control technologies such as blowing or suction. Further, localized heating can represent an energy neutral active flow control approach through reuse of engine waste heat on the nacelle, for example. The use of thermodynamic flow control has been proposed in both laminar and turbulent flows. In a fully turbulent channel flow, for example, targeted heating can be used to modulate coherent structures and reduce drag [74, 18]. In the transitional regime, a series of investigations have been undertaken for over 40 years. As a general rule, uniform cooling has a stabilizing effect on laminar boundary layers because the viscosity increases in the wall-normal direction which dampens the viscous instabilities modes [148]. Inversely, uniform heating plays a destabilizing role. Although the heating of a gas increases the local viscosity, thus reducing the local Reynolds number, it can result in a local inflectional instability of the velocity profile, which leads to a precocious transition to turbulence. In the case of a heated wall, the viscosity is at its maximum value at the wall and decreases as the wall distance increases. This has a destabilizing effect on the shape of the velocity profile. To better illustrate this effect, Figure 6.1 shows the effect of cooling and heating on the velocity profile near the wall. As seen on Figure 6.1, the wall cooling tends to create a more stable, *thicker*, velocity profile, analogous to the effect of a favorable pressure gradient in a boundary layer, while wall heating tends to create an "S" shaped profile. Unlike uniform heating, strategically placed strips of localized heating can help delay the transition. Dogval [44] experimentally showed that localized heating delays transition in 2D and 3D boundary layers, but if the transition mechanism is due to cross-flow instabilities, the heating remains ineffective.
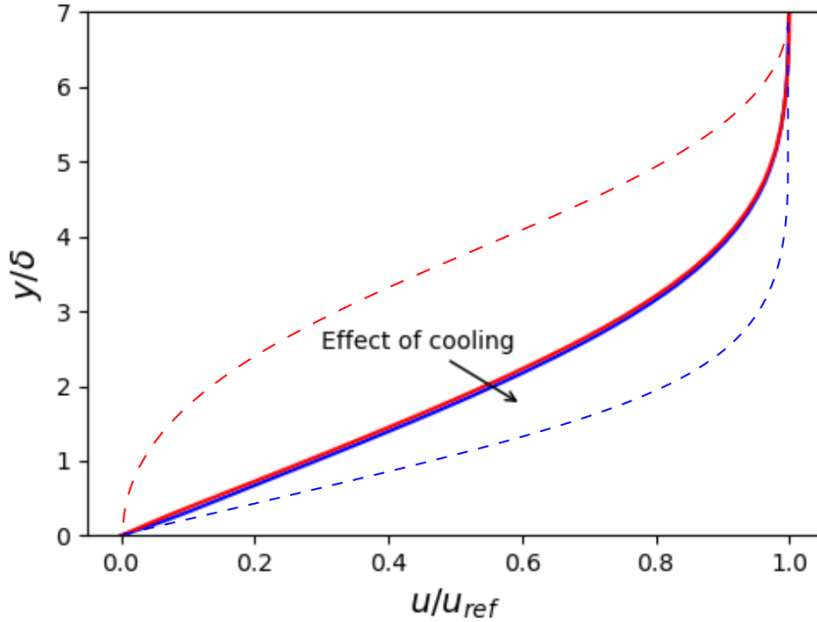
FIGURE 6.1. Effect of cooling and heating on the stream-velocity profile on a compressible Blasius boundary layer flow at Mach 0.714. The dashed line represent the exaggerated effect of cooling and heating

Physically, although localized heating is destabilizing when placed in regions of linear instability growth, if the strips are placed upstream of this point, the downstream unheated wall effectively becomes a *cooled wall*. The unheated wall acts to restabilize the boundary layer and delay the overall transition to turbulence [111]. Localized heating strips have been suggested as an active flow control approach for supersonic transport [25]. Heating strips can also be used to stabilize the first mode in supersonic flows[120]. The stabilizing effect was nuanced by [149] who suggested that the heating strip only had a stabilizing effect if the temperature of the 'cooled' wall remained below the adiabatic wall temperature. Several recent contributions have continued to optimize these flow stabilization strategies [110, 178, 54, 138, 219].

   The understanding of the effects of localized heating on the stabilization of the transitional boundary layer has greatly benefited from a number of theoretical and numerical studies. Krad *et al.*[98] completed early DNS of periodic forcing due to wall heating on a

flat plate boundary layer. Using PSE, [23] found that the optimal position of the heating strips was upstream of the neutral point. Stabilization among multiple disturbance frequencies remains an open question in their work. More recent work by [145] studied the sensitivity of methods to determine the location of the transition.

The existing body of research provides a good physical understanding of boundary layer stabilization through localized heating or cooling. However, most studies are applied in the context of active flow control design. In most applied settings, the active flow control device is operated in regions that have non-negligible wall curvature, for example, on the nacelle or wing. As a result, the stabilization effects due to the presence of localized heating are impacted by the local pressure gradients. In this context, assessing the effect of curvature, or surface imperfection, on the efficacy of thermodynamic flow control systems is not an easy task. Although some work has been done to investigate the effect of isolated roughness in the presence of cooling or heating, recent work on this topic is scarce. Among the most recent papers, Abid [1] investigated the effect of an isolated roughness element in the presence of a cooling strip on the stability of an incompressible boundary layer. Their LST results suggested that the presence of roughness was destabilizing regardless of the strip location. However, the height of the investigated hump was on the verge of causing flow separation. It was observed that cooling increases the growth rate near or in separation bubbles [121, 3]. Continuous cooling, on the other hand, has a thinning effect on the boundary layer and makes it more sensitive to roughness, as it artificially increases the apparent height of incoming obstacles [121]. In that perspective, the effect of low-amplitude roughness in the presence of short, localized, temperature strips on the modal response of compressible Blasius flow remains unclear. To this end, we conduct a NPSE-based parametric study on localized wall heating/cooling under high subsonic conditions. Then, the focus is moved toward a comparative study of the coupling effect between the use of roughness and cooling/heating strips. The potential benefits of distributed temperature strips and physical smooth roughness on the transitional characteristics of a flat plate boundary layer are explored and contrasted to the results presented in the previous chapter.

6.2 Numerical tools

The stability of a zero pressure gradient flat plate boundary layer with nonuniform wall heating is investigated using the nonlinear Parabolized Stability Equations (PSE). The PSE are a subset of modal stability theory which can be used to investigate weakly non-parallel flows such as the spatially evolving, laminar boundary layer. It was shown in the previous chapter that PSE and Direct Numerical Simulations (DNS) are nearly indistinguishable when the surface roughness remains small. The main discrepancies between the two approaches arise when nonlinear interactions cause a modification to the base flow. As thermodynamic heating provides a very subtle change to the main flow characteristics and the computational cost is about 4 orders of magnitude less than the equivalent DNS, the present study focuses solely on the use of PSE to parametrically investigate the stability characteristics of this flow.

To this end, we use Krypton [105], a new open source PSE code that integrates both the base flow computations of the laminar compressible Navier-Stokes equations on a curvilinear coordinate system; we use both the linear and nonlinear stability calculations of this solver. Details on the code are provided in the previous two chapters and are not repeated for brevity. The Reynolds and Mach reference numbers are defined on the basis of the *inlet* state and are defined as

$$Re_\delta = \sqrt{\frac{u_0 x_0}{\nu_0}} \qquad\qquad Ma = \frac{u_0}{\sqrt{\gamma R_0 T_0}} \qquad\qquad (6.1)$$

Where the subscript 0 represents the reference values of the freestream and $\delta = \sqrt{\frac{\nu_0 x_0}{u_0}}$ is a length scale proportional to the thickness of the *inlet* boundary layer.

6.3 Effect of wall temperature on transition

The parametric investigation of the stability characteristics of spatially varying wall temperature is investigated. First, we consider the case of a sinusoidal wall temperature oscillations on a flat plate boundary layer and compare the stability characteristics with
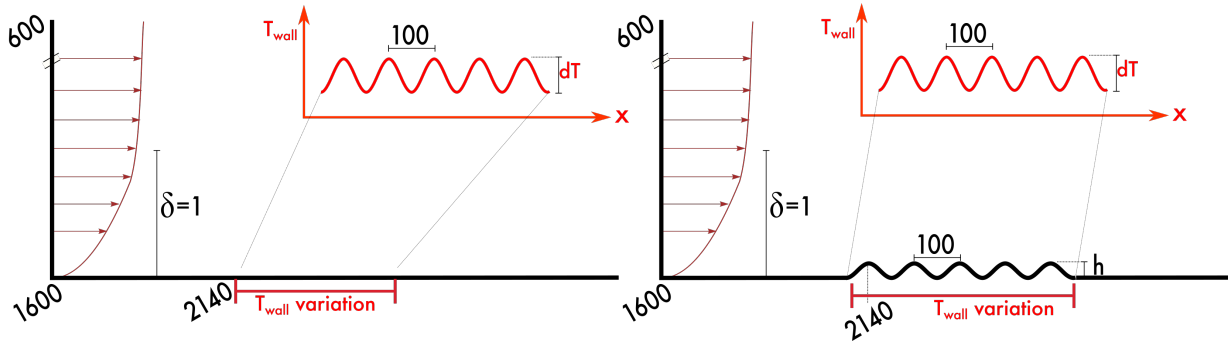
FIGURE 6.2. Diagram of the numerical setups. All the dimensions are scaled by δ. dT/T_0 is varied from -0.33 to 0.33 and $h = 0.33\delta$ (corresponding to less than $1/10$ of the boundary layer thickness). Figure on the left shows the domain with only thermal roughness (Section 6.3), figure on the right shows the combination of smooth roughness and wall temperature fluctuations (Section 6.4).

the smooth-roughness case investigated in the previous chapter, this corresponds to the setup in figure 6.2 (left). In the following section, we combine both the sinusoidal wall temperature variations with the smooth roughness to explore the stabilization effects, the setup is shown in figure 6.2 (right).

In the present work, we focus on the effect of two-dimensional heating and cooling strips on the boundary layer transition at a freestream Mach number of 0.714. The setup is very similar to the one investigated in Chapter 5, consists of a canonical spatially evolving, zero pressure gradient, flat plate boundary layer with 5 successive sinusoidal heating or cooling strips. The location and amplitude of the wall temperature undulations are based on the same mathematical function as the humps of Case 1, in Chapter 5, to facilitate comparison with a validated case with smooth roughness. The wall temperature and the roughness amplitude are illustrated in Figure 6.3, for completeness. Figure 6.4 shows the contour of the temperature of two representative cases for which the parametric study is conducted. In total, 9 different cases are investigated at various wall temperatures, ranging from $T_{wall}/T_\infty = 0.665$, to $T_{wall}/T_\infty = 1.335$. The intensity of incoming turbulence is set to 0.18% in all cases and the frequency content is the same as in the Case 1 in chapter 5.

As we can see, whereas the presence of heating or cooling strips has a very limited impact on the thickness of the boundary layer (see comparative boundary layer thickness in
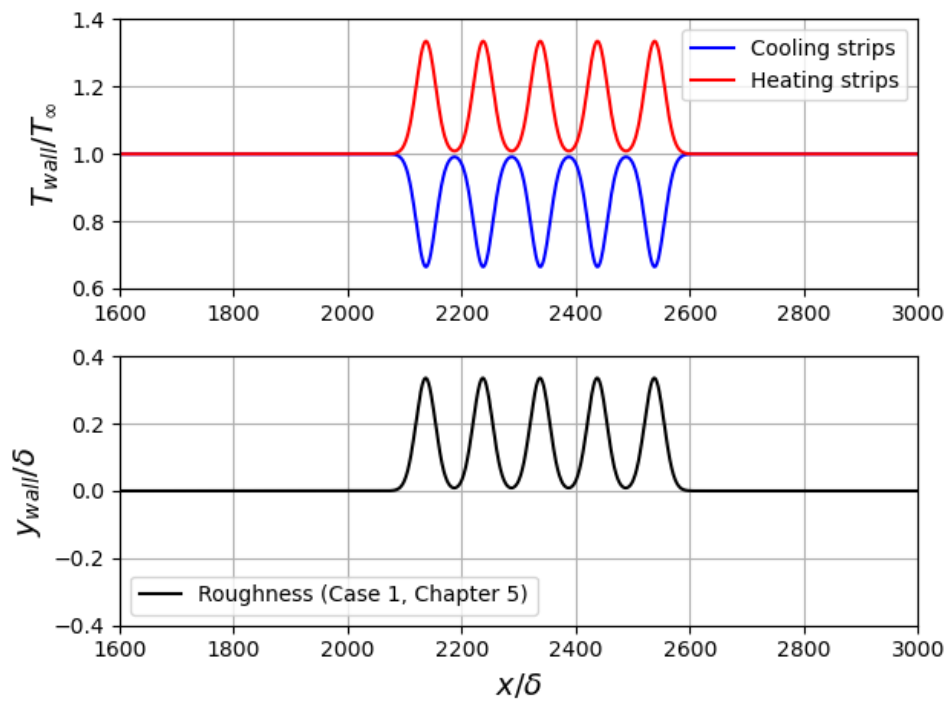
FIGURE 6.3. Illustration of the numerical setup. $y_{wall} = h(x)$, $T_{wall} = 1 \pm h(x)$
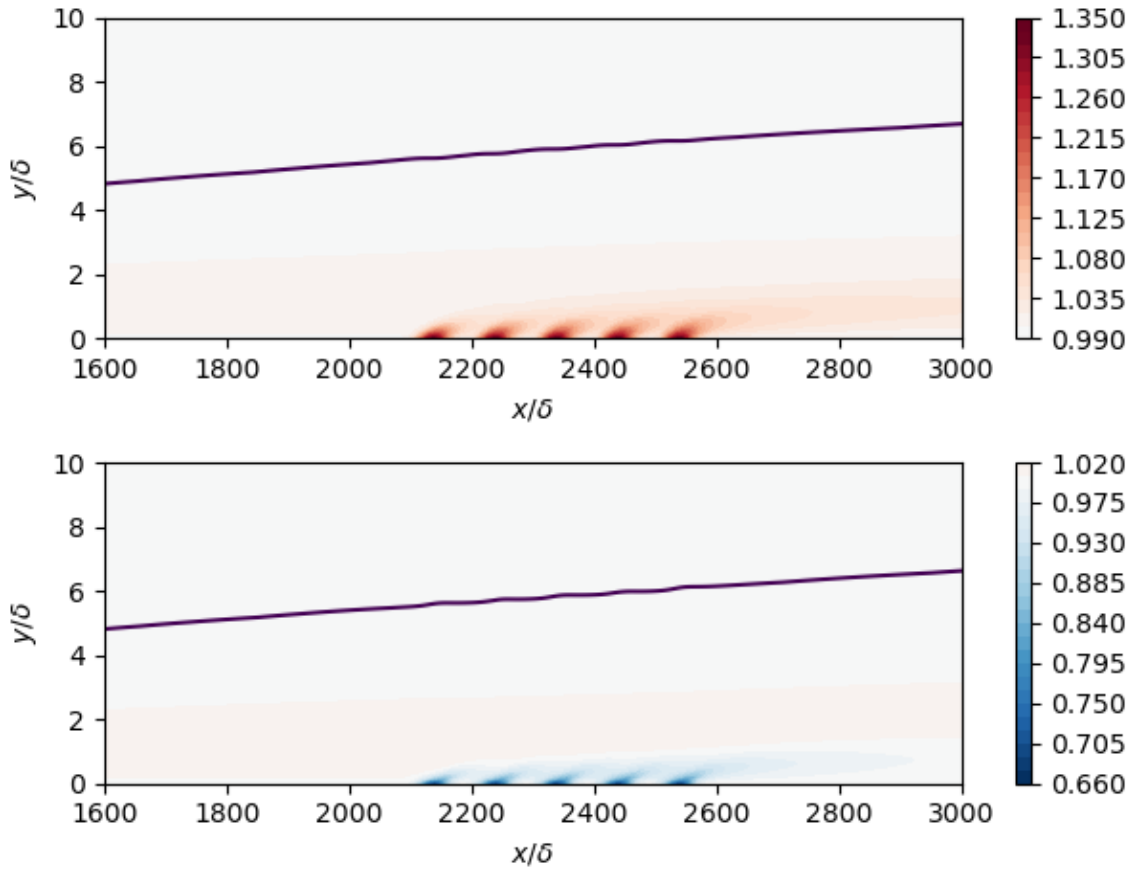
FIGURE 6.4. Contour plot of the temperature for the case with heating strips ($\frac{T_{wall}}{T_\infty} = 1.335$) and cooling stips ($\frac{T_{wall}}{T_\infty} = 0.665$). The solid line is the boundary layer thickness ($\delta_{0.99}$)

figure 6.4), the impact is most noticable on the wall friction coefficient, shown in figure 6.5. In figure 6.5, both the laminar and mean flow distortion (MFD) skin-friction coefficients are shown. These estimates can be used to determine the transition location. Adding cooling strips stabilizes the boundary layer, and in contrast, the addition of heating strips is drastically destabilizing. This result was expected because the location of the wall temperature perturbations is in the modal growth region [44]. Although it is possible to qualitatively estimate the transition location based on the wall friction in figure 6.5, it is more convenient to define a quantitative criterion to better highlight any physical trends that we could observe. Here, we define the beginning of transition based on the MFD wall friction, transition to turbulence is triggered once the absolute of the MFD wall friction exceeds 5% of the laminar friction, that is, when $|\frac{\partial \hat{u}_{(0,0)}}{\partial y} / \frac{\partial u_{lam}}{\partial y}| > 0.05$. Figure 6.6 shows the relative transitional Reynolds number as a function of the heating strips' temperature. ΔRe_{tr} is defined as the difference between the transition Reynolds number with and without heat transfer strips. The linear trend gave the best fit, but could lead to non-physical transition location prediction. For example, if used for temperatures higher than ≈ 2.5, the fit predicts a transition *before* the heating strip. However, the slope of the fit offers a good point of comparison.
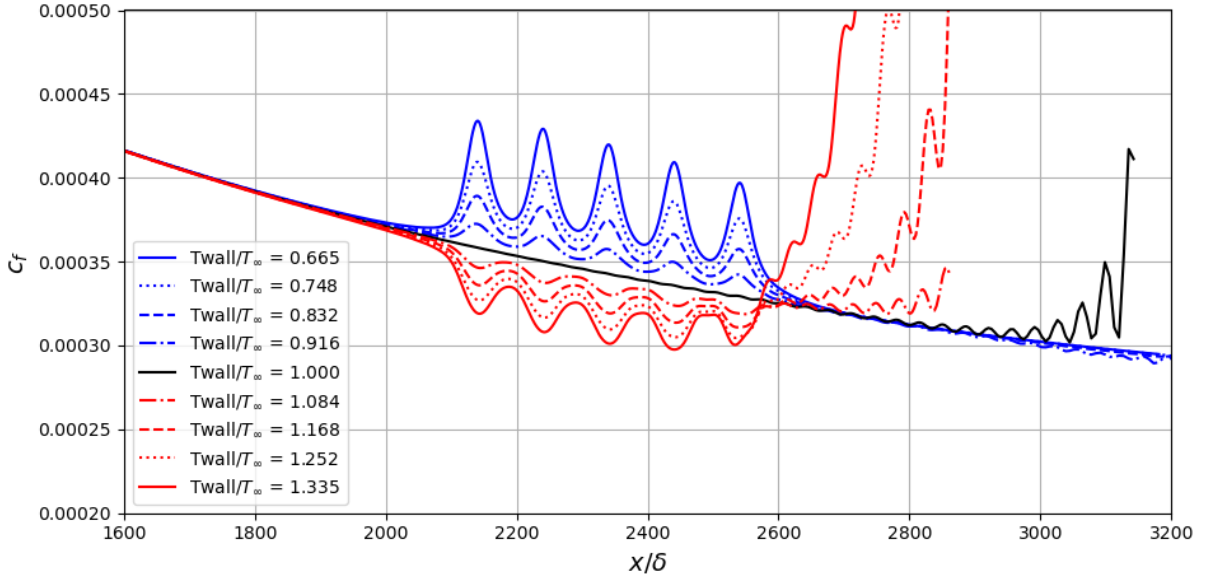
FIGURE 6.5. Effect of cooling and heating (without physical roughness) on the friction coefficient along the stream direction. The coefficient of friction is computed based on the sum of the laminar and MFD contributions.

6.4 Combined effect of temperature strips and smooth roughness on modal stability

In laminar boundary layers, cooling strips help stabilize the flow by decreasing the viscous instability. Other mechanisms can have a similar effect. In this regard, it was reported that the stabilizing effect of cooling strips is similar to that of a smooth forward-facing step (FFS) [3] while a backward-facing step (BFS) is analogous to wall heating, thus destabilizing. However, this conclusion is only valid for a smooth geometry, as the impact of discrete FFS and BFS is always destabilizing and increases with step height [43]. Ultimately, a smooth hump can be seen as a smooth FFS, immediately followed by a smooth BFS. Following this logic, a sequence of multiple humps could be seen as an alternating sequence of heating and cooling strips. Since the effect of BFS is generally *more* destabilizing than that of a FFS, a sequence of multiple humps is therefore considered to be destabilizing.
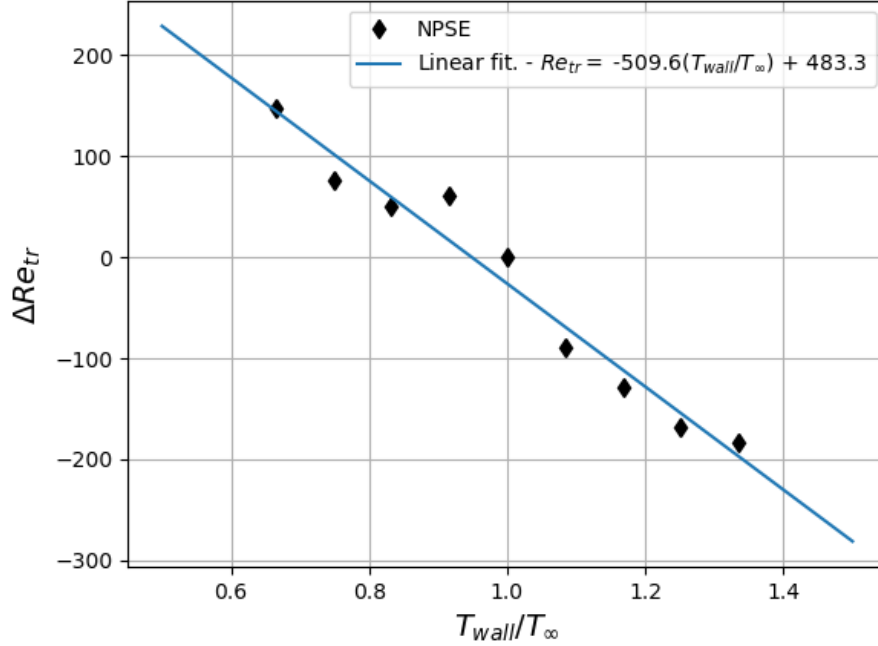
FIGURE 6.6. Effect of cooling and heating on the transition location. ZPG flat plate at $M = 0.714$. The transition criteria is met when $|\frac{\partial \hat{u}_{(0,0)}}{\partial y} / \frac{\partial u_{lam}}{\partial y}| > 0.05$

Now, let's say we add cooling strips at the most unstable points, i.e. at the crest of each physical roughness hump. We now have a different sequence in which a favorable pressure gradient enhances the stability, followed by a cooling strip which also has a beneficial effect, and, finally, the descent of the hump which causes destabilization. In this context, it is not clear whether the overall effect will be stabilizing or destabilizing. The quantification of this effect is investigated in the present section. Figure 6.7 shows the temperature contour of two representative cases of the same geometry.

Figure 6.8 shows the evolution of the disturbance kinetic energy (DKE) along the streamwise direction for 6 representative cases. The red, blue, and black curves correspond, respectively to the $T_{wall}/T_{\infty} = 1.335$, $T_{wall}/T_{\infty} = 0.665$ and isotherm cases. The solid line represents the combination of physical ($h = 0.33\delta$) and thermodynamic roughness, whereas the dashed line corresponds to the DKE of only the thermodynamic roughness. Solid and

114
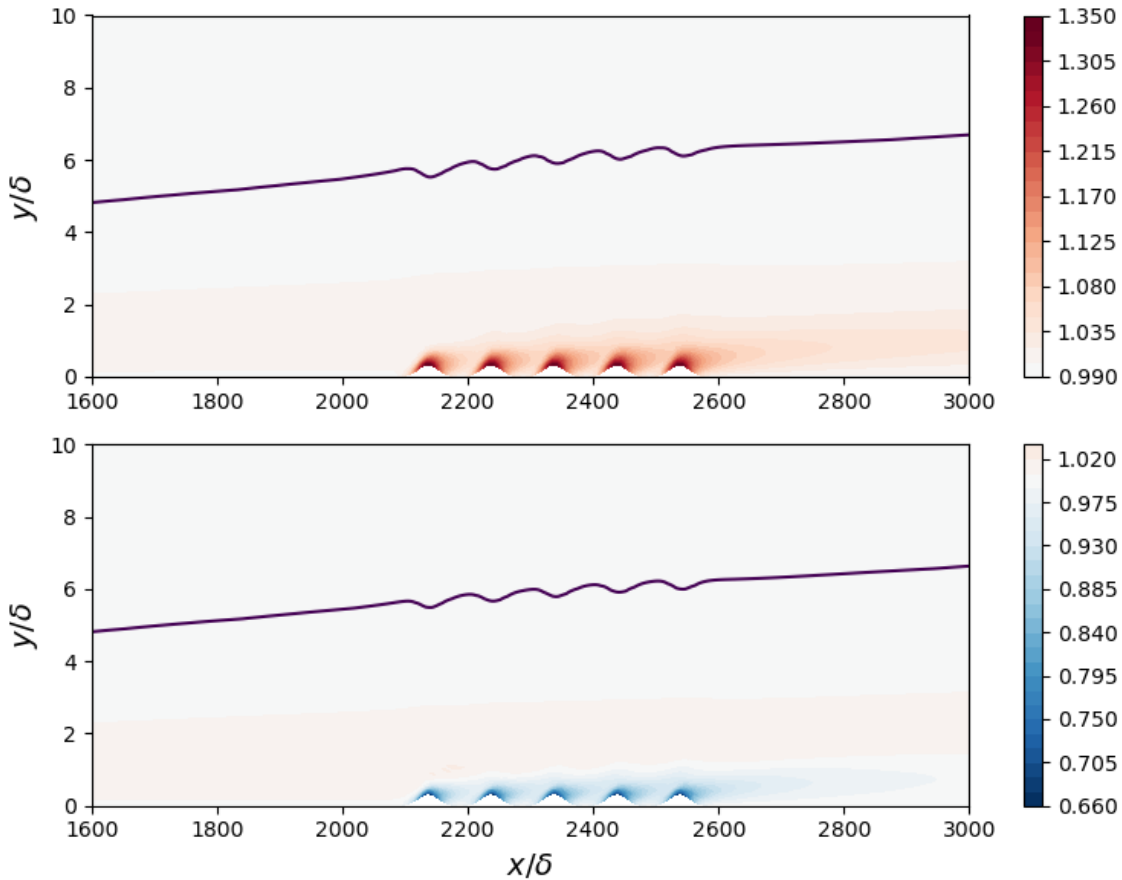
FIGURE 6.7. Contour plot of the temperature for the case with heating strips (top) and cooling stips (bottom). Both cases features a sequence of 5 sinusoidal humps of $h = 0.33\delta$. The solid line is the boundary layer thickness $(\delta_{0.99})$

dashed black has no thermodynamic roughness. We see that the humps have a slightly destabilizing effect in the isotherm and heated cases. Interestingly, the presence of physical roughness (humps) and thermodynamic cooling tends to enhance the effect of the cooling strips alone. One possible explanation is that the cooling strips stabilize the flow by acting on two fronts: (1) it reduces the inflectional instability, by locally decreasing the viscosity; (2) it induces a downward velocity by increasing the local density which partly cancels the effect of the flow going down the valley.

115
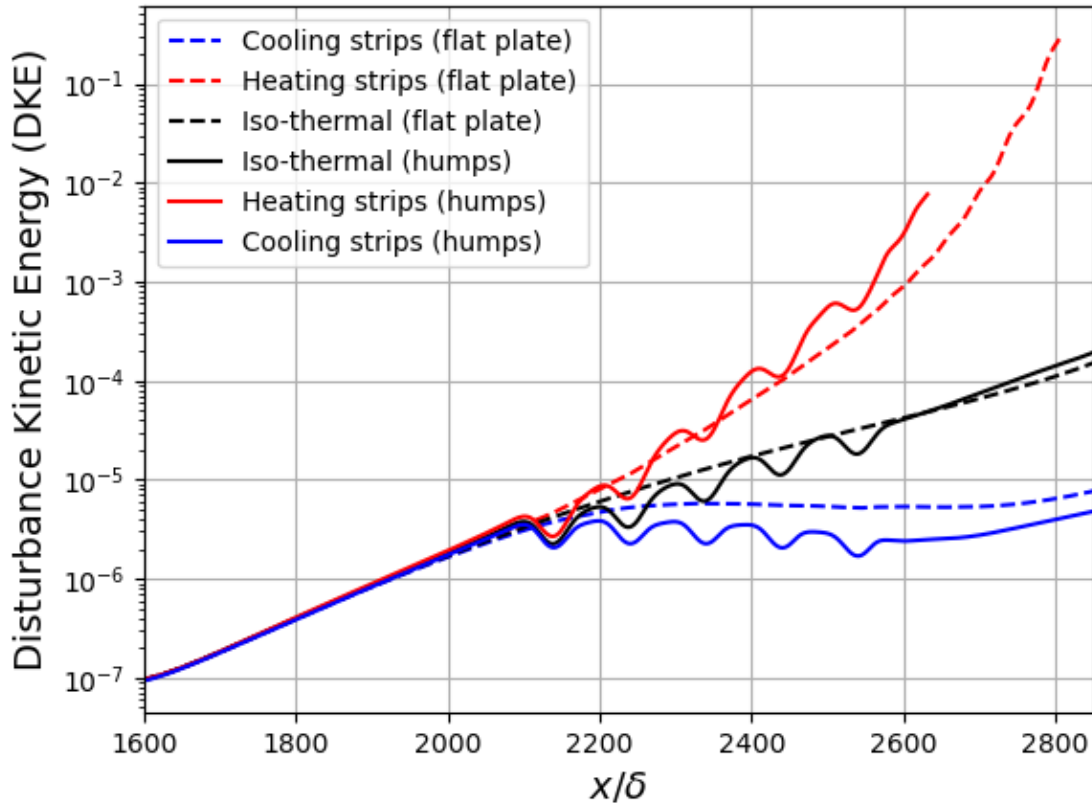
FIGURE 6.8. Disturbances Kinetic Energy (DKE) along the stream-wise direction

In figure 6.8, the scale is logarithmic and the damping is thus less apparent. The contour plot of the Disturbance Kinetic Energy (DKE), shown on figure 6.9, offers a fairer view of the stabilization caused by the combined cooling and roughness effects. For comparative purposes, the color range is identical for all panels. As we can see, the cooling strips are very effective at reducing the amplitude of the disturbances in the near-wall region, but are even more efficient at eliminating the onset of instabilities in the region above the boundary layer. The rise of disturbances above the boundary layer is particularly destabilizing and usually indicates the rapid growth of secondary instabilities. The cases featuring cooling strips are extremely efficient at neutralizing these freestream instabilities,

116
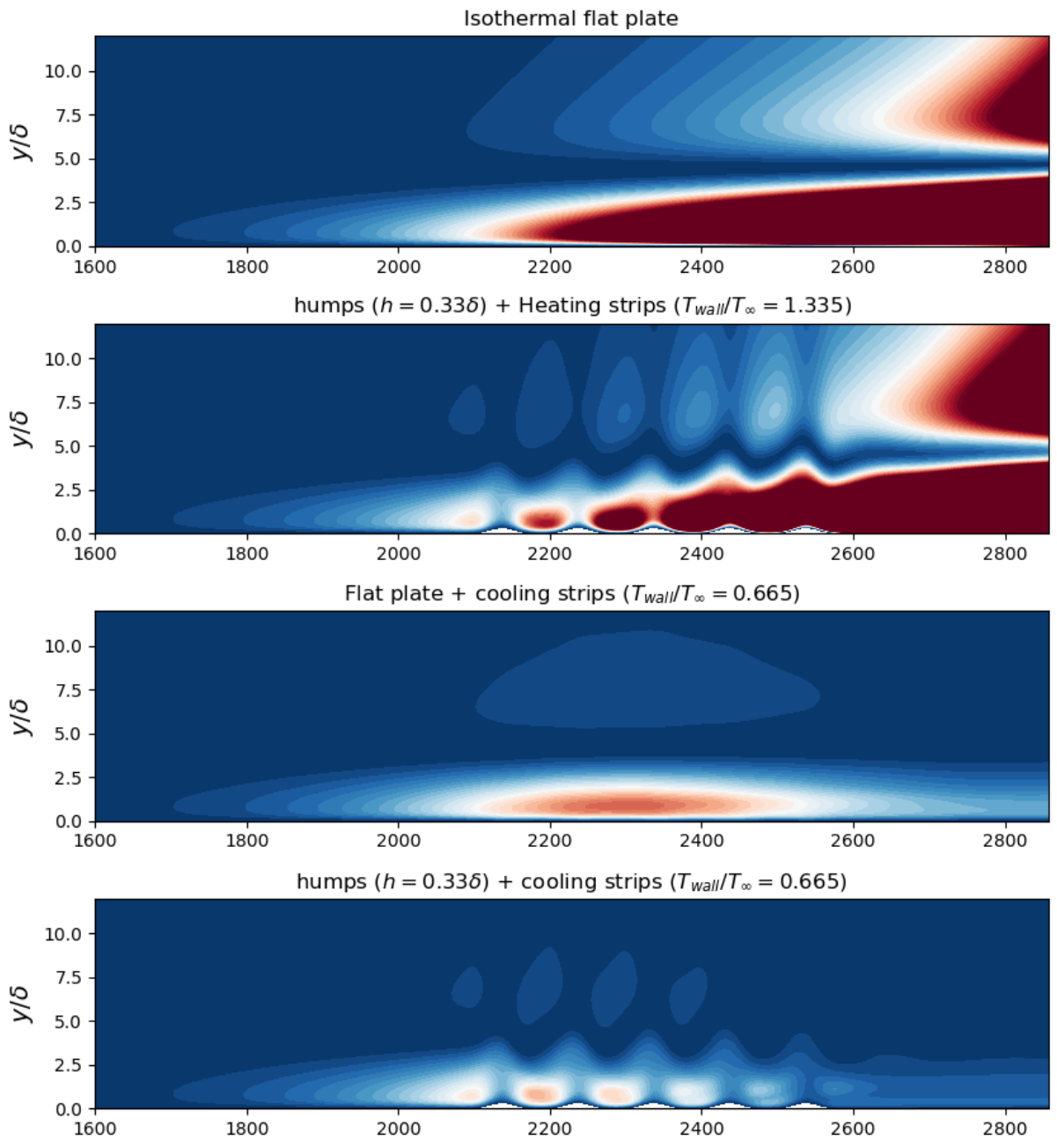
FIGURE 6.9. Contour plot of the Disturbances Kinetic Energy (DKE). The color range from blue (DKE $= 0$) to red (DKE $= 4 \times 10^{-6}$) and is the same for all plot.

117

suggesting a stronger damping effect on the higher frequencies. To verify this assumption, the wall friction spectrum for different regions is shown in figures 6.10 and 6.11. The colors indicate the wall temperature; each line style represents a different portion of the wall and is identified in the caption. Starting with the effect of the heating strips alone, we first observe on figure 6.10 that the heating strips tend to amplify the whole frequency spectrum, but more specifically the off-peak frequencies, as we observe a broader peak around the dominant frequency. This effect is even more noticeable at the 2F harmonic, for which the neighboring frequencies experience a considerably higher amplification which leads to the formation of a local minimum near $F \approx 32$. The cooling strips induce the opposite effect; we observe a dampening effect on the off-peak frequencies, which makes the dominating frequency more easily distinguishable. However, this time we see the emergence of a peak near $F \approx 32$ and 45. Recalling that the inlet T-S frequency is $F = 18$, and its harmonics are $36, 54, 72$, etc. It is interesting to note that in the presence of cooling strips we observe the formation of two other peaks at frequencies $(32, 45)$ that are not multiples of the fundamental T-S frequency (18), nor of the cooling strips (39). This effect is more pronounced in the presence of roughness, as seen in Figure 6.11, but the frequencies remain the same, leading us to think that the periodic excitation of the flow, whether by the use of temperature strips or smooth wall roughness, induces the formation of off-harmonic perturbations. The use of a finite-bandwidth approach was crucial to this observation, as in a classical discrete representation, only the dominant mode and its harmonics are solved $(F, 2F, 3F, ...)$.

6.5   Conclusion

The coupling effect between the roughness and the temperature strips is investigated under transonic conditions using the nonlinear parabolized stability equations (NPSE). To this end, we first study the effect of heating and cooling strips on the stability of a zero-pressure gradient flat plate boundary layer. The effect of a smooth roughness patch, consisting of five sinusoidal two-dimensional humps, was added to the zero-pressure gradient flat plate boundary layer in order to study the coupling effect between roughness and wall temperature. The temperature strips and the roughness elements are located after the
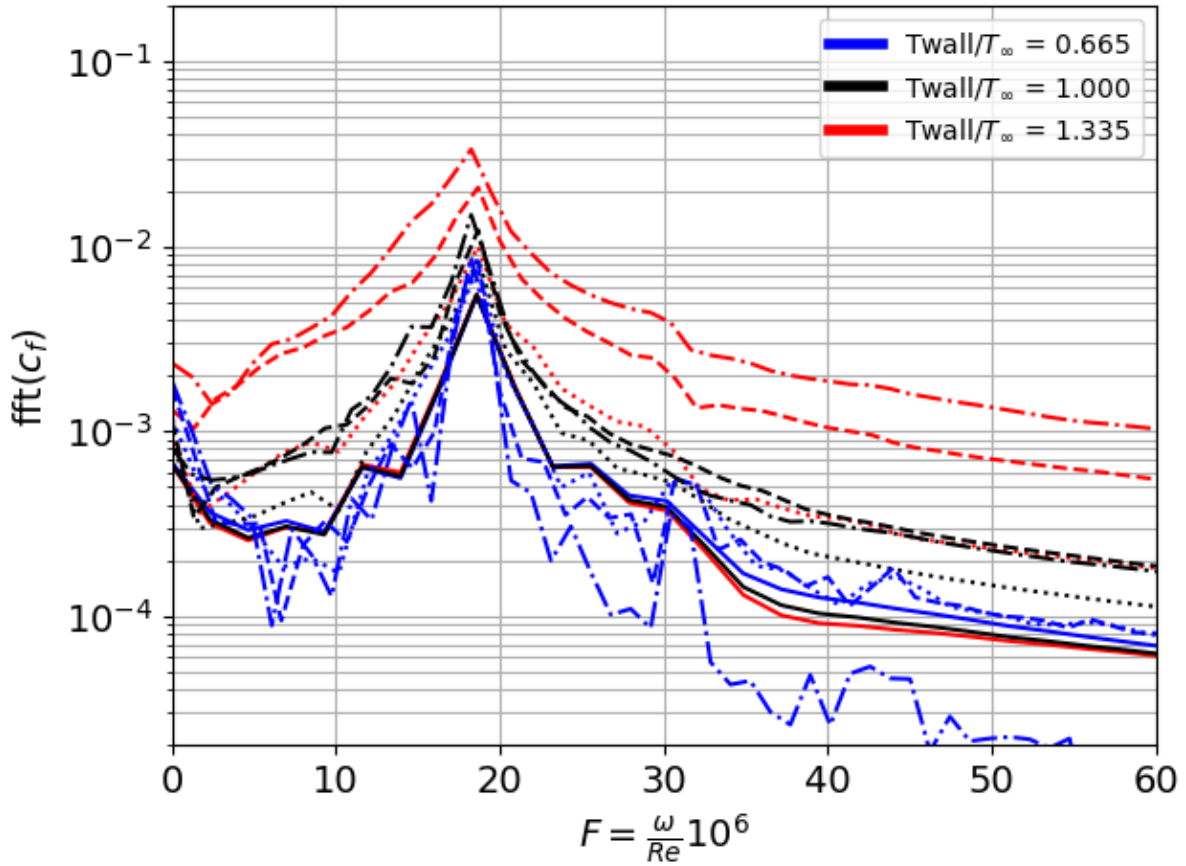
FIGURE 6.10. fft(c_f) for different wall regions in *absence* of wall curvature, obtained with NPSE. The colors indicate the temperature (cold, isothermal or hot). Each linestyle corresponds to a different region (—— is $x \in [1600, 2140]$, ········ is $x \in [1600, 2340]$, - - - - is $x \in [1600, 2540]$,-·-·-· is $x \in [1600, 2640]$)
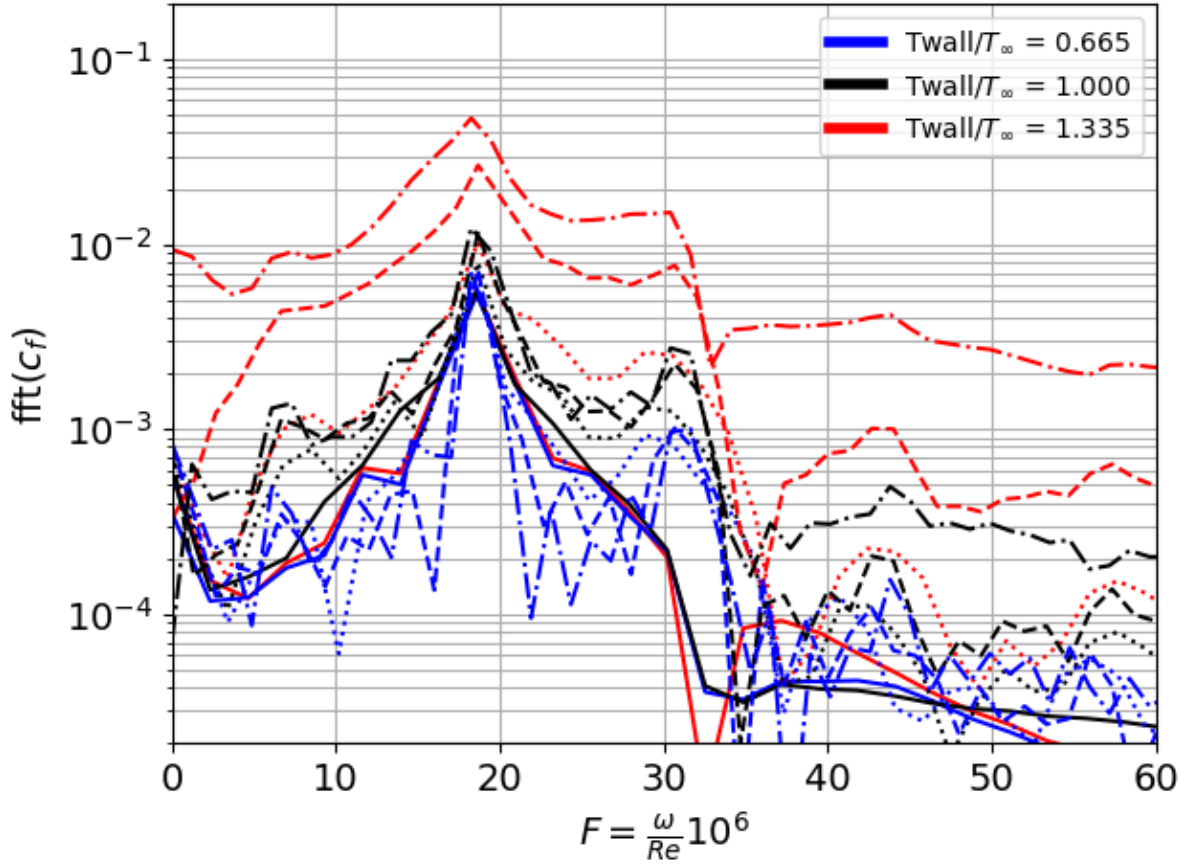
FIGURE 6.11. fft(c_f) for different wall regions in *presence* of humps, obtained with NPSE. The colors indicate the temperature (cold, isothermal or hot). Each linestyle corresponds to a different region (——— is $x \in [1600, 2140]$, ········· is $x \in [1600, 2340]$, - - - - is $x \in [1600, 2540]$,-·-··-·· is $x \in [1600, 2640]$)

onset of instability (branch I) and extend over a range of 500δ. Both the heating strips and the roughness patch are defined using the same mathematical expression. The NPSE-based parametric study confirms the stabilizing effect of cooling strips and the destabilizing effect of heating strips on the stability of T-S waves in the ZPG flat plate scenario. The analysis reveals a spectral broadening in the presence of heating and a spectral narrowing in the presence of cooling. The NPSE study reveals a catalytic coupling effect between the temperature strips and roughness. In other words, when compared to the flat plate case, the stability of the flow decreases in the presence of heating strips and roughness. Inversely, in comparison with the flat plate case, the stability is increased in the presence of cooling strips and roughness.

Chapter 7

Conclusion

The research was initially motivated by the lack of a sufficiently accurate and lightweight transition prediction tool for Natural or Hybrid Laminar flow control design in aerospace. Thus, the emphasis was placed on improving the transition predictions in complex aeronautical flows. More specifically, the research focuses on the effect of two-dimensional roughness on the modal stability of transonic flows. The term roughness here is used in the broad sense and regroups the effect of physical roughness, i.e. wall curvature, thermodynamic roughness, i.e. non-homogeneous wall temperature, or both.

In Chapters 3 and 4, we developed a comprehensive framework to study the propagation and amplification of modal-like perturbations in a variety of complex compressible flows. The model, based on the nonlinear parabolized stability equations (NPSE), is sufficiently exhaustive to be applied in realistic high-speed flow situations featuring wall curvature, compressibility effects, cross-flow, adverse pressure gradients, and nonadiabatic surface effects. The structure can be used to study acoustic propagation via PSE. The model is validated against published experimental and numerical data. The project, which was recently made open source [105], can serve as the basis for the future development of modal stability-based problems in aerospace engineering, geophysical and multiphase flows. All the necessary routines and methods included in the code allow for the extension of the code to 3D simulations.

In Chapter 3, we also describe the implementation of curvilinear coordinates in the

massively parallel DNS code Hybrid. The implementation of curvilinear coordinates in Hybrid helped lay the foundations of a large-scale DNS-based canonical case of study on the effect of smooth two-dimensional roughness on the stability characteristics of a transonic ($Ma = 0.714$) boundary layer (Chapter 5. In particular, the influence of the two-dimensional smooth roughness on the stability of 2D T-S waves is investigated using two variants of the same setup consisting of an array of five humps of two different heights. This case of study served three purposes. First, it helped validate the pertinence of the NPSE framework in the presence of wall curvature and compressibility effects. Second, DNS results revealed a stronger destabilizing effect on the higher frequencies for the case with the highest humps. This effect is believed to be associated with a rapid growth of secondary instabilities, which skips the standard T-S mechanism and gives rise to a cyclical transitional pattern in which both late K-type structures and premature bypass transition are observable. This numerical setup, at the limit between bypass and normal transition, brings to light that the role of surface imperfections on transition to turbulence is more nuanced than intuition would lead us to believe. Third, the DNS study helped identify span-periodic disturbances downstream of the roughness array, suggesting that at a sufficiently high curvature level, the mode experiencing the highest amplification is three-dimensional. An observation that is also supported by the –linear– PSE.

In Chapter 6, the effect of localized heating and cooling on the stability of compressible boundary layers under transonic conditions ($Ma = 0.714$) is investigated. More specifically, the scope is on the coupling effect between smooth roughness and temperature strips. The numerical setup is identical to the one used in the previous DNS study, in order to provide an additional layer of comprehension to the physics of the problem. The temperature strips and the roughness elements begin after the onset of instability (branch I) and extend for 500δ. Both the heating strips and the roughness patch are defined using the same mathematical expression. The parametric study confirms the stabilizing effect of the cooling strips and the destabilizing effect of the heating strips on the stability of the T-S waves in the ZPG flat plate scenario. The analysis reveals a spectral broadening in the presence of heating and a spectral narrowing in the presence of cooling, regardless of the presence of roughness. The NPSE analysis reveals a catalytic coupling effect between the temperature strips and the roughness. In other words, compared with the heated ZPG

geometry, the stability of the flow decreases in the presence of heating strips and roughness. Inversely, compared with the cooled ZPG geometry, the stability is increased in the presence of cooling strips and roughness. This finding is important because it could help improve temperature-based active laminar flow control devices.

7.1   Recommendations & future work

1. Chapter 5 discusses the effect of smooth, two-dimensional roughness on the stability characteristics of a transonic boundary layer. In this chapter, two variants of the same setup with two different heights are investigated. In the case featuring the highest humps, the agreement between the DNS and the NPSE gradually decreases as the perturbations progress downstream ; the DNS suggests that this increasing discrepancy is linked to a rapid growth of the higher harmonics. From a modal point of view, as seen in Chapters 5 and 6, higher modes are generally more sensitive to base flow modifications, and the presence of roughness, in the broad sense of the term, tends to promote the formation of such stationary disturbance. Now, if the height of the roughness is sufficiently high, for example, in Case 2 (Chapter 5), the parabolicy assumption becomes ill-suited to the problem. The use of a stabilization term in the marching procedure helps alleviate this effect by "removing" the remaining ellipticity. By experience, we observe that even though stabilization is necessary when the step size is reduced below a certain threshold regardless of the frequency, the problems related to ellipticity usually affect the low-frequency mode first, as they have a larger spectral radius. By definition, since the MFD is stationary, $Re(\alpha_{0,0}) = \omega_{0,0} = 0$. This implies that the MFD has an infinite spectral radius, in which case the use of a stabilization term is pointless and the ellipticity can only be removed by dropping the streamwise pressure gradient term completely. This assumption is questionable in the presence of high curvature and should be revisited. In the current state of theory, the MFD represents the accumulated effects of the nonlinear forcing on the base flow, without the elliptic component. In this sense, an interesting approach could be to separate the MFD into an elliptic component, which could be solved using a central scheme based on a global approach, and a parabolic component, which would be

solved using a similar marching procedure. The latter is important to maintain the effect of nonlinear interactions. Without exactly using this approach, the nonmodal stability theory and the One-Way Navier-Stokes equations represent steps in the same direction.

2. In Chapter 6, we investigated the coupling effect between temperature and curvature roughness. The analysis revealed that, when strategically located, the curvature of the wall can enhance the stabilizing effect of the cooling strips. In this optic, it is known that when placed before the onset of instability, i.e. before branch I, heating strips can have a stabilizing effect. In the current study, the temperature strips were defined using the same mathematical expression as the physical roughness and were thus located in the region experiencing the highest growth, i.e. at the top of each hump. It could be interesting to see if heating strips, when placed slightly upstream of physical roughness, could lead to a stabilizing effect similar to what is observed when placed upstream of branch I.

References

[1] Ridha Abid and Jamal A. Masad. Effect of localized cooling on laminar flow. *International Journal of Engineering Science*, 34(14):1573–1583, 1996.

[2] Christophe Airiau. Non-parallel acoustic receptivity of a Blasius boundary layer using an adjoint approach. *Flow, Turbulence and Combustion*, 65(3-4):347–367, 2000.

[3] Ayman Al-Maaitah, Ali Nayfeh, and Saad Ragab. Effect of wall cooling on the stability of compressible subsonic flows over smooth humps and backward-facing steps. *Physics of Fluids A Fluid Dynamics*, 2, 04 1990.

[4] Mohan Ananth and Mario F Trujillo. SoftwareX 2PJIT : Two-phase 3D jet instability tool in cylindrical coordinates. *SoftwareX*, 18:101011, 2022.

[5] John David Anderson. *Hypersonic and high temperature gas dynamics*. Aiaa, 2000.

[6] P Andersson, DS Henningson, and A Hanifi. On a stabilization procedure for the parabolic stability equations. *Journal of Engineering Mathematics*, 33(3):311–332, 1998.

[7] C.D. Argyropoulos and N.C. Markatos. Recent advances on the numerical modelling of turbulent flows. *Applied Mathematical Modelling*, 39(2):693–732, 2015.

[8] A. K. Bajaj and V. K. Garg. Linear Stability of Jet Flows. *Journal of Applied Mechanics*, 44(September 1977):378, 1977.

[9] P. Balakrishnan and K. Srinivasan. Jet noise reduction using co-axial swirl flow with curved vanes. *Applied Acoustics*, 126:149–161, 2017.

[10] Ponnampalam Balakumar and Michael Kegerise. Roughness-induced transition in a supersonic boundary layer. *AIAA Journal*, 54(8):2322–2337, 2016.

[11] S. Balay, J. Brown, K. Buschelman, V. Eijkhout, W. Gropp, D. Kaushik, M. Knepley, L. Curfman McInnes, B. Smith, and H. Zhang. PETSc Users Manual Revision 3.4. Technical report, Argonne National Laboratory (ANL), Argonne, IL (United States), 6 2014.

[12] Iván Bermejo-Moreno, Julien Bodart, Johan Larsson, Blaise M. Barney, Joseph W. Nichols, and Steve Jones. Solving the compressible Navier-Stokes equations on up to 1.97 million cores and 4.1 trillion grid points. *International Conference for High Performance Computing, Networking, Storage and Analysis, SC*, 2013.

[13] Matteo Bernardini, Sergio Pirozzoli, and Paolo Orlandi. Compressibility effects on roughness-induced boundary layer transition. *International Journal of Heat and Fluid Flow*, 35:45–51, 2012.

[14] F. P. Bertolotti and Th Herbert. Analysis of the linear stability of compressible boundary layers using the PSE. *Theoretical and Computational Fluid Dynamics*, 3(2):117–124, 1991.

[15] Fabio Bertolotti. The Effect of Approximations to the Thermodynamic Properties on the Stability of Compressible Boundary Layer Flow. In *Instability and Transition*, pages 83–98. Springer New York, New York, NY, 1990.

[16] FP Bertolotti. Linear and nonlinear stability of the Blasius boundary layer. *Journal of Fluid Mechanics*, 242(-1):441–474, 9 1992.

[17] A V Boiko, V V Kozlov, V V Syzrantsev, and V A Shcherbakov. Riblet control of the laminar-turbulent transition in a stationary vortex on an oblique airfoil. *Journal of Applied Mechanics and Technical Physics volume*, 37(1), 1996.

[18] T. Bon and J. Meyers. Stable channel flow with spanwise heterogeneous surface temperature. *Journal of Fluid Mechanics*, 933:A57, 2022.

[19] David Borgmann, Shirzad Hosseinverdi, Jesse C Little, and Hermann F Fasel. Investigation of low-speed boundary-layer instability and transition using experiments, theory and dns. In *AIAA AVIATION 2020 FORUM*, page 2948, 2020.

[20] V. I. Borodulin, A. V. Ivanov, Y. S. Kachanov, and A. P. Roschektaev. Receptivity coefficients at excitation of cross-flow waves due to scattering of free-stream vortices on surface vibrations. *Journal of Fluid Mechanics*, 793:162–208, 4 2016.

[21] V. I. Borodulin, A. V. Ivanov, Y. S. Kachanov, and A. P. Roschektaev. Receptivity coefficients at excitation of cross-flow waves due to scattering of free-stream vortices on surface vibrations. *Journal of Fluid Mechanics*, 793:162–208, 4 2016.

[22] R. J. Boyle and F. F. Simon. Mach Number Effects on Turbine Blade Transition Length Prediction. *Journal of Turbomachinery*, 121(4):694–702, 10 1999.

[23] A. M.H. Brooker, J. Severin, and H. Herwig. Analysis of boundary layer control by heat transfer strips using an asymptotic approach to the PSE. *Forschung im Ingenieurwesen/Engineering Research*, 67(1):11–18, 2002.

[24] M. A. Bucci, D. K. Puckert, C. Andriano, J. C. Loiseau, S. Cherubini, J. C. Robinet, and U. Rist. Roughness-induced transition by quasi-resonance of a varicose global mode. *Journal of Fluid Mechanics*, 836:167–191, 2018.

[25] D M Bushnell. Aircraft drag reduction—a review. *Proceedings of the I MECH E Part G Journal of Aerospace Engineering*, 217(1):1–18, 2003.

[26] Richard L Campbell and Michelle N Lynde. Building a practical natural laminar flow design capability. In *35th AIAA Applied Aerodynamics Conference*, page 3059, 2017.

[27] Chris D Cantwell, David Moxey, Andrew Comerford, Alessandro Bolis, Gabriele Rocco, Gianmarco Mengaldo, Daniele De Grazia, Sergey Yakovlev, J-E Lombard, D Ekelschot, et al. Nektar++: An open-source spectral/hp element framework. *Computer physics communications*, 192:205–219, 2015.

[28] Amanda Chou, Rudolph A. King, and Michael A. Kegerise. Transition induced by an egg-crate roughness on a flat plate in supersonic flow. *Aiaa Aviation 2020 Forum*, 1 PartF:1–16, 2020.

[29] Meelan Choudhari and Paul Fischer. Roughness-induced transient growth. 06 2005.

[30] Meelan Choudhari, Fei Li, and Pedro Paredes. Effect of distributed patch of smooth roughness elements on transition in a high-speed boundary layer. *2018 Fluid Dynamics Conference*, pages 1–19, 2018.

[31] Yann Colin, Bertrand Aupoix, J.F. Boussuge, and Philippe Chanez. Prediction of crosswind inlet flows : some numerical and modelling challenges. *AIAA paper*, page 27, 2008.

[32] Tim Colonius, Arnab Samanta, and Kristjan Gudmundsson. Parabolized stability equation models of large-scale jet mixing noise. *Procedia Engineering*, 6:64–73, 1 2010.

[33] J. C. Cooke and L. Howarth. The boundary layer of a class of infinite yawed cylinders. *Mathematical Proceedings of the Cambridge Philosophical Society*, 46(04):645, 10 1950.

[34] Marco Costantini. Experimental analysis of geometric, pressure gradient and surface temperature effects on boundary-layer transition in compressible high reynolds number flows. *DLR Deutsches Zentrum fur Luft- und Raumfahrt e.V. - Forschungsberichte*, 2016-Janua(62):1–279, 2016.

[35] Marco Costantini, Steffen Risius, and Christian Klein. Non-Adiabatic Surface Effects on Step-Induced Boundary-Layer Transition. *Flow, Turbulence and Combustion*, 100(4):1145–1177, 6 2018.

[36] Joseph W Croswell. *On the energetics of primary and secondary instabilities in plane Poiseuille flow*. PhD thesis, Virginia Polytechnic Institute and State University, 1985.

[37] J. D. Crouch and V. S. Kosorygin. Surface step effects on boundary-layer transition dominated by tollmien–schlichting instability. *AIAA Journal*, 58(7):2943–2950, 2020.

129

[38] Tyler S Dean, Gabrielle E Wroblewski, and Phillip J Ansell. Mission analysis and component-level sensitivity study of hybrid-electric general-aviation propulsion systems. *Journal of Aircraft*, 55(6):2454–2465, 2018.

[39] Antonio Di Giovanni and Christian Stemmer. Direct numerical simulations of roughness-induced transition in the boundary layer of a hypersonic spherical forebody under consideration of high-temperature gas effects. In *2018 Fluid Dynamics Conference*, page 4046, 2018.

[40] M Di Renzo and J Urzay. Direct numerical simulation of a hypersonic transitional boundary layer at suborbital enthalpies. *Journal of Fluid Mechanics*, 912, 2021.

[41] Alexander Dobrinsky. *Adjoint analysis for receptivity prediction*. PhD thesis, Rice University, 2002.

[42] Alexander Dobrinsky and S. Scott Collis. Adjoint parabolized stability equations for receptivity prediction. *Fluids 2000 Conference and Exhibit*, 2000-2651:2000, 6 2000.

[43] Ming Dong and Anyong Zhang. Scattering of Tollmien-Schlichting waves as they pass over forward-/backward-facing steps. *Applied Mathematics and Mechanics*, 39(10):1411–1424, 2018.

[44] A. V. Dovgal, V. Ya. Levchenko, and V. A. Timopeev. Boundary Layer Control by a Local Heating of the Wall. *Laminar-Turbulent Transition*, pages 113–121, 1990.

[45] Robert S. Downs, Edward B. White, and Nicholas A. Denissen. Transient growth and transition induced by random distributed roughness. *AIAA Journal*, 46(2):451–462, 2008.

[46] Jonathan Driver and David Zingg. Optimized natural-laminar-flow airfoils. In *44th AIAA Aerospace Sciences Meeting and Exhibit*, page 247, 2006.

[47] Zhiwei Duan, Zhixiang Xiao, and Song Fu. Direct numerical simulation of hypersonic transition induced by ramp roughness elements. In *52nd Aerospace Sciences Meeting*, page 0237, 2014.

[48] F. Gokhan Ergin and Edward B. White. Unsteady and Transitional Flows Behind Roughness Elements. *AIAA Journal*, 44(11):2504–2514, 2006.

[49] Sébastien Esquieu, Elizabeth Benitez, Steven P. Schneider, and Jean-Philippe Brazier. *Flow and Stability Analysis of a Hypersonic Boundary Layer over an Axisymmetric Cone Cylinder Flare Configuration.*

[50] A. Fage. The smallest size of spanwise surface corrugation which affects boundary-layer transition on an airfoil, 1943.

[51] H. Fasel. Investigation of the stability of boundary layers by a finite-difference model of the navier—stokes equations. *Journal of Fluid Mechanics*, 78(2):355–383, 1976.

[52] H Fasel and U Konzelmann. Non-parallel stability of a flat-plate boundary layer using the complete navier-stokes equations. *Journal of Fluid Mechanics*, 221:311–347, 1990.

[53] Alexander Fedorov. Transition and Stability of High-Speed Boundary Layers. *Annual Review of Fluid Mechanics*, 43(1):79–95, 2011.

[54] Alexander Fedorov, Vitaly Soudakov, Ivan Egorov, Andrey Sidorenko, Yury Gromyko, Dmitry Bountin, Pavel Polivanov, and Anatoly Maslov. High-speed boundary-layer stability on a cone with localized wall heating or cooling. *AIAA Journal*, 53(9):2512–2524, 2015.

[55] Frank E. Fish, Paul W. Weber, Mark M. Murray, and Laurens E. Howle. The tubercles on humpback whales' flippers: Application of bio-inspired technology. *Integrative and Comparative Biology*, 51(1):203–213, 2011.

[56] Kahei Danny Fong and Xiaolin Zhong. DNS and PSE study on the stabilization effect of hypersonic boundary layer waves using 2-D surface roughness. *46th AIAA Fluid Dynamics Conference*, (June):1–21, 2016.

[57] Sparsh Ganju, Sean C.C. Bailey, and Christoph Brehm. Amplitude and wavelength scaling of sinusoidal roughness effects in turbulent channel flow at fixed $\boldsymbol{Re_\tau}$=**720**. *Journal of Fluid Mechanics*, 937, 2022.

[58] Bing Gao and S. O. Park. Compressible Parabolized Stability Equation in Curvilinear Coordinate System and Integration, 2006.

[59] Ricardo García-Mayoral and Javier Jiménez. Hydrodynamic stability and breakdown of the viscous regime over riblets. *Journal of Fluid Mechanics*, 678:317–347, 2011.

[60] M. Serdar Genç, İlyas Karasu, H. Hakan Açıkel, and M. Tuğrul Akpolat. Low reynolds number flows and transition. In Mustafa Serdar Genc, editor, *Low Reynolds Number*, chapter 1. IntechOpen, Rijeka, 2012.

[61] Sacha Ghebali, Sergei I. Chernyshenko, and Michael A. Leschziner. Can large-scale oblique undulations on a solid wall reduce the turbulent drag? *Physics of Fluids*, 29(10), 2017.

[62] Nathan Gray, Shane McDonagh, Richard O Shea, Beatrice Smyth, and Jerry D Murphy. Decarbonising ships, planes and trucks: An analysis of suitable low-carbon fuels for the maritime, aviation and haulage sectors. *Advances in Applied Energy*, 1:100008, 2021.

[63] Kristjan Gudmundsson and Tim Colonius. Parabolized stability equation models for turbulent jets and their radiated sound. In *15th AIAA/CEAS Aeroacoustics Conference (30th AIAA Aeroacoustics Conference)*, page 3380, 2009.

[64] Christoph Hader and Hermann F Fasel. Direct numerical simulations of hypersonic boundary-layer transition for a flared cone: fundamental breakdown. *Journal of Fluid Mechanics*, 869:341–384, 2019.

[65] P. Hall. The linear development of Gortler vortices in growing boundary layers. *Journal of Fluid Mechanics*, 130:41–58, 1983.

[66] A. M. Hamed, M. Sadowski, Z. Zhang, and L. P. Chamorro. Transition to turbulence over 2D and 3D periodic large-scale roughnesses. *Journal of Fluid Mechanics*, 804:R6, 2016.

[67] Ali M. Hamed, Arpeet Kamdar, Luciano Castillo, and Leonardo P. Chamorro. Turbulent boundary layer over 2D and 3D large-scale wavy walls. *Physics of Fluids*, 27(10), 2015.

[68] Zhong-Hua Han, Jing Chen, Ke-Shi Zhang, Zhen-Ming Xu, Zhen Zhu, and Wen-Ping Song. Aerodynamic Shape Optimization of Natural-Laminar-Flow Wing Using Surrogate-Based Approach. *AIAA Journal*, 56(7):2579–2593, 2018.

[69] Stefan J. Hein, Alexander Theiss, Antonio Di Giovanni, Christian Stemmer, Thomas Schilden, Wolfgang Schroeder, Pedro Paredes, Meelan M. Choudhari, Fei Li, and Eli Reshotko. Numerical Investigation of Roughness Effects on Transition on Spherical Capsules. In *2018 AIAA Aerospace Sciences Meeting*, pages 1–25, Reston, Virginia, jan 2018. American Institute of Aeronautics and Astronautics.

[70] J P P Hemmen. Towards Practical Hybrid Laminar Flow Control Boundary Layer Stability with Suction and Scalability of Pressure Losses across Perforated Sheets. Technical report.

[71] T. Herbert. Secondary instability of boundary layers. *Annual Review of Fluid Mechanics*, 20:487–526, 1988.

[72] Thorwald Herbert. Parabolized Stability Equations. *Annual Review of Fluid Mechanics*, 29(1):245–283, 1997.

[73] T Hetsch and U Rist. Accuracy of local and nonlocal linear stability theory in swept separation bubbles. *AIAA journal*, 47(5):1116–1122, 2009.

[74] Jean-Pierre Hickey, Khaled Younes, Matthew X. Yao, Duosi Fan, and Joseph Mouallem. Targeted turbulent structure control in wall-bounded flows via localized heating. *Physics of Fluids*, 32(3):035104, 2020.

[75] Bruce J. Holmes, Clifford J. Obara, Glenn L. Martin, and Christopher S. Domack. Manufacturing Tolerances for Natural Laminar Flow Airframe Surfaces. *SAE Transactions*, 94:522–531, 1985.

[76] Shirzad Hosseinverdi and Masoud Boroomand. Prediction of laminar-turbulent transitional flow over single and two-element airfoils. In *40th Fluid Dynamics Conference and Exhibit*, page 4290, 2010.

[77] Shirzad Hosseinverdi and Hermann F Fasel. Role of klebanoff modes in active flow control of separation: direct numerical simulations. *Journal of Fluid Mechanics*, 850:954–983, 2018.

[78] M. Y. Hussaini, D. A. Kopriva, and A. T. Patera. Spectral collocation methods. *Applied Numerical Mathematics*, 5(3):177–208, 5 1989.

[79] M K Ibrahim and Y Nakamura. Correlation between Linear stability theory and transition of compressible jet shear layer. *Transactions of the Japan Society for Aeronautical and Space Sciences*, 45(147):35–44, 2002.

[80] J. L. van Ingen. A suggested semi-empirical method for the calculation of the boundary layer transition region, 1956.

[81] J. L. Van Ingen. Historical review of work at TU Delft. *38th Fluid Dynamics Conference and Exhibit*, (June):1–49, 2008.

[82] Maxime Itasse, Jean-Philippe Brazier, Olivier Léon, and Grégoire Casalis. Parabolized Stability Equations analysis of nonlinear interactions with forced eigenmodes to control subsonic jet instabilities. *Physics of Fluids*, 27(8):084106, 8 2015.

[83] N. Itoh. Secondary Instability of Laminar Flows. *Proceedings of the Royal Society A: Mathematical, Physical and Engineering Sciences*, 375(1763):565–578, 1981.

[84] J. John Soundar Jerome and Jean Marc Chomaz. Extended Squire's transformation and its consequences for transient growth in a confined shear flow. *Journal of Fluid Mechanics*, 744:430–456, 2014.

[85] Peter Jordan and Tim Colonius. Wave packets and turbulent jet noise. *Annual Review of Fluid Mechanics*, 45(1):173–195, 2013.

[86] Matthew P. Juniper, Ardeshir Hanifi, and Vassilios Theofilis. Modal stability theory: Lecture notes from the flow-nordita summer school on advanced instability methods for complex flows, stockholm, sweden, 2013. *Applied Mechanics Reviews*, 66(2):021004, 2014.

[87] Yu S Kachanov, VV Kozlov, and V Ya Levchenko. Nonlinear development of a wave in a boundary layer. *Fluid dynamics*, 12(3):383–390, 1977.

[88] Yu S Kachanov and V Ya Levchenko. The resonant interaction of disturbances at laminar-turbulent transition in a boundary layer. *Journal of Fluid Mechanics*, 138:209–247, 1984.

[89] Omar Kamal, Georgios Rigas, Matthew T. Lakebrink, and Tim Colonius. *Application of the One-Way Navier-Stokes (OWNS) Equations to Hypersonic Boundary Layers.*

[90] Kean Lee Kang and K.S. Yeo. Combined effects of amplitude, frequency and bandwidth on wavepackets in laminar turbulent transition. *Computers & Fluids*, 197:104358, 2020.

[91] Arham Amin Khan, Tony Liang, Armani Batista, and Joseph Kuehl. On energy redistribution for the nonlinear parabolized stability equations method. *Fluids*, 7(8), 2022.

[92] Arham Amin Khan, Tony Liang, Armani Batista, and Joseph Kuehl. On energy redistribution for the nonlinear parabolized stability equations method. *Fluids*, 7(8), 2022.

[93] Jae Wook Kim and Duck Joo Lee. Generalized characteristic boundary conditions for computational aeroacoustics. *AIAA journal*, 38(11):2040–2049, 2000.

[94] Jae Wook Kim and Duck Joo Lee. Generalized characteristic boundary conditions for computational aeroacoustics, part 2. *AIAA journal*, 42(1):47–55, 2004.

[95] Rudolph A King and Kenneth S Breuer. Acoustic receptivity and evolution of two-dimensional and oblique disturbances in a Blasius boundary layer. *Journal of Fluid Mechanics*, 432(April):69–90, 2001.

[96] P. S. Klebanoff and K. D. Tidstrom. Mechanism by which a two-dimensional roughness element induces boundary-layer transition. *Physics of Fluids*, 15(7):1173–1188, 1972.

[97] P. S. Klebanoff, K. D. Tidstrom, and L. M. Sargent. The three-dimensional nature of boundary-layer instability. *Journal of Fluid Mechanics*, 12(1):1–34, 1962.

[98] L.D. Kral and H. F. Fasel. Direct Numerical Simulation of Passive Control of Three-Dimensional Phenomena in Boundary-Layer Transition Using Wall Heating. *Journal of Fluid Mechanics*, 264:213–254, 1994.

[99] Joseph Kuehl, Eduardo Perez, and Helen Reed. JoKHeR: NPSE Simulations of Hypersonic Crossflow Instability. *50th AIAA Aerospace Sciences Meeting including the New Horizons Forum and Aerospace Exposition*, (January):1–14, 2012.

[100] Joseph J. Kuehl. Discrete- and finite-bandwidth-frequency distributions in nonlinear stability applications. *Physics of Fluids*, 29(2):024101, 2017.

[101] Joseph J. Kuehl. Discrete- and finite-bandwidth-frequency distributions in nonlinear stability applications. *Physics of Fluids*, 29(2):024101, 2017.

[102] A. Kurz, S. Grundmann, C. Tropea, M. Forte, A. Seraudie, O. Vermeersch, D. Arnal, R. Goldin, and R. King. Boundary Layer Transition Control using DBD Plasma Actuators. *Aerospace Lab*, (6):p. 1–8, June 2013.

[103] O. K. Kwon and R. H. Pletcher. Prediction of the incompressible flow over a rearward-facing step. Technical Report HTL-26, CFD-4, Iowa State Univ., Ames, IA, 1981.

[104] Francis Lacombe and Jean Pierre Hickey. Roughness-induced transition prediction over complex geometries with linear parabolized stability equations (LPSE). *11th International Symposium on Turbulence and Shear Flow Phenomena, TSFP 2019*, pages 1–6, 2019.

[105] Francis Lacombe and Jean-Pierre Hickey. Krypton: Nonlinear parabolized stability equation solver for transonic flow in curvilinear coordinates. *SoftwareX*, 20:101206, 2022.

[106] Johan Larsson, Ivan Bermejo-Moreno, and Sanjiva K Lele. Reynolds-and mach-number effects in canonical shock–turbulence interaction. *Journal of Fluid Mechanics*, 717:293–321, 2013.

[107] Johan Larsson and Sanjiva K. Lele. Direct numerical simulations of canonical shock-/turbulence interaction. *6th International Symposium on Turbulence and Shear Flow Phenomena, TSFP 2009*, 2009-June(January 2009):1345–1350, 2009.

[108] Fei Li, Meelan Choudhari, Chau-lyan Chang, and Jeffery White. Secondary Instability of Second Mode Disturbances in Hypersonic Boundary Layers. pages 1–14, 2013.

[109] Fei Li and Mujeeb R. Malik. Spectral analysis of parabolized stability equations. *Computers and Fluids*, 26(3):279–297, 1997.

[110] Xian Liang, Xinliang Li, Dexun Fu, and Yanwen Ma. Effects of wall temperature on boundary layer stability over a blunt cone at mach 7.99. *Computers & fluids*, 39(2):359–371, 2010.

[111] H. W. Liepmann, G. L. Brown, and D. M. Nosenchuck. Control of laminar-instability waves using a new technique. *Journal of Fluid Mechanics*, 118(-1):187, 1982.

[112] Jean Christophe Loiseau, Jean Christophe Robinet, Stefania Cherubini, and Emmanuel Leriche. Investigation of the roughness-induced transition: Global stability analyses and direct numerical simulations. *Journal of Fluid Mechanics*, 760:175–211, 2014.

[113] A. Lozano-Durán, M. J.P. Hack, and P. Moin. Modeling boundary-layer transition in direct and large-eddy simulations using parabolized stability equations. *Physical Review Fluids*, 3(2), 2018.

[114] Yuhan Lu, Fanzhi Zeng, Hongkang Liu, Zaijie Liu, and Chao Yan. Direct numerical simulation of roughness-induced transition controlled by two-dimensional wall blowing. *Journal of Fluid Mechanics*, 920:1–35, 2021.

[115] Paolo Luchini and Alessandro Bottaro. Adjoint Equations in Stability Analysis. *Annu. Rev. Fluid Mech*, 46:493–517, 2014.

[116] Leslie M Mack. Boundary-layer linear stability theory. Technical report, California Inst of Tech Pasadena Jet Propulsion Lab, 1984.

[117] M. R. Malik. Numerical methods for hypersonic boundary layer stability. *Journal of Computational Physics*, 86(2):376–413, 1990.

[118] Mujeeb R Malik. Prediction and control of transition in supersonic and hypersonic boundary layers. *AIAA journal*, 27(11):1487–1493, 1989.

[119] J. A. Masad and A. H. Nayfeh. Laminar flow control of subsonic boundary layers by suction and heat-transfer strips. *Physics of Fluids A*, 4(6):1259–1272, 1992.

[120] Jamal A. Masad and Ridha Abid. On transition in supersonic and hypersonic boundary layers. *International Journal of Engineering Science*, 33(13):1893–1919, 1995.

[121] Jamal A. Masad and Venkit Iyer. Transition prediction and control in subsonic flow over a hump. *Physics of Fluids*, 6(1):313–327, 1994.

[122] Matthias Baer. Findiff: A Python package for finite difference derivatives in any number of dimensions, 2018.

[123] Fred W Matting. General solution of the laminar compressible boundary layer in the stagnation region of blunt bodies in axisymmetric flow. Technical report, Ames Research Center (NASA), Moffett Field, CA, 1964.

[124] Sandip Mazumder. *Numerical methods for partial differential equations: Finite difference and finite volume methods*, volume M. 2015.

[125] Pascal Meyer. Application of HLF Technology to Civil Nacelle. *Aerodynamic Drag Reduction Technologies*, pages 107–114, 2001.

[126] MohammadMirzaieDaryan, Hamid. *Aeroacoustics of Compressible Vortex Reconnection*. PhD thesis, 2021.

[127] Marc Montagnac. Variable Normalization (Nondimensionalization and Scaling) for Navier-Stokes Equations: A Practical Guide. pages 1–14, 2013.

[128] Iván Padilla Montero and Fabio Pinna. Stability Analysis of the Boundary Layer Developing on a Flat Plate with Discrete Roughness Elements in Hypersonic Flow. (January), 2018.

[129] Emmanuel Motheau, Ann Almgren, and John B Bell. Navier–stokes characteristic boundary conditions using ghost cells. *AIAA Journal*, 55(10):3399–3408, 2017.

[130] Alexander J. Moyes, Pedro Paredes, Travis S. Kocian, and Helen L. Reed. Secondary instability analysis of crossflow on a hypersonic yawed straight circular cone. *Journal of Fluid Mechanics*, 812:370–397, 2017.

[131] Suman Muppidi and Krishnan Mahesh. Direct numerical simulations of roughness-induced transition in supersonic boundary layers. *Journal of Fluid Mechanics*, 693:28–56, 2012.

[132] NASA. Langley Stability and Transition Analysis Code (LASTRAC). https://software.nasa.gov/software/LAR-16260-1, 2022. [Online; accessed 19-May-2022].

[133] United Nations. 41st session of the icao assembly - environment, 2022.

[134] Jan Nordström. The use of characteristic boundary conditions for the navier-stokes equations. *Computers & Fluids*, 24(5):609–623, 1995.

[135] Andrey Novikov, Ivan Egorov, and Alexander Fedorov. Direct numerical simulation of supersonic boundary layer stabilization using grooved wavy surface. In *48th AIAA Aerospace Sciences Meeting Including the New Horizons Forum and Aerospace Exposition*, page 1245, 2010.

[136] Gustavo Luiz Olichevis Halila, Krzysztof J. Fidkowski, and Joaquim R. R. A. Martins. Toward automatic parabolized stability equation-based transition-to-turbulence prediction for aerodynamic flows. *AIAA Journal*, 59(2):462–473, 2021.

[137] Nick B Oliviero. *EPIC: A new and advanced nonlinear parabolized stability equation solver*. PhD thesis, Texas A&M, 2015.

[138] Furkan Oz and Kursat Kara. Effects of local cooling on hypersonic boundary-layer stability. In *AIAA Scitech 2021 Forum*, page 0940, 2021.

[139] Roberto Pacciani, Michele Marconcini, Andrea Arnone, and Francesco Bertini. An assessment of the laminar kinetic energy concept for the prediction of high-lift, low-reynolds number cascade flows. *Proceedings of the Institution of Mechanical Engineers Part A Journal of Power and Energy*, 225:995–1003, 11 2011.

[140] P. Paredes, V. Theofilis, D. Rodríguez, and J. A. Tendero. The PSE-3D instability analysis methodology for flows depending strongly on two and weakly on the third spatial dimension. *6th AIAA Theoretical Fluid Mechanics Conference*, (June):1–21, 2011.

[141] Pedro Paredes, Meelan M. Choudhari, Fei Li, and Chau-Lyan Chang. Transient Growth Analysis of Compressible Boundary Layers with Parabolized Stability Equations. In AIAA SciTech Forum, editor, *54th AIAA Aerospace Sciences Meeting*, number January, pages 1–19, Reston, Virginia, 1 2016. American Institute of Aeronautics and Astronautics.

[142] Pedro Paredes, Meelan M. Choudhari, Fei Li, and Chau-Lyan Chang. *Transient Growth Analysis of Compressible Boundary Layers with Parabolized Stability Equations*. 2016.

[143] Pedro Paredes, Ardeshir Hanifi, Vassilis Theofilis, and Dan S. Henningson. The Nonlinear PSE-3D Concept for Transition Prediction in Flows with a Single Slowly-varying Spatial Direction. *Procedia IUTAM*, 14:36–44, 2015.

[144] Donghun Park and Seung O Park. Study of effect of a smooth hump on hypersonic boundary layer instability. *Theoretical and Computational Fluid Dynamics*, 30(6):543–563, 2016.

[145] J. Park and T. A. Zaki. Sensitivity of high-speed boundary-layer stability to base-flow distortion. *Journal of Fluid Mechanics*, 476:476–515, 2019.

[146] Fabio Pinna. VESTA toolkit: a Software to Compute Transition and Stability of Boundary Layers. *43rd Fluid Dynamics Conference*, pages 1–9, 2013.

[147] T.J Poinsot and S.K Lelef. Boundary conditions for direct simulations of compressible viscous flows. *Journal of Computational Physics*, 101(1):104–129, 1992.

[148] By Jan O Pralits and Ardeshir Hanifi. Optimization of Steady Wall Temperature for Disturbance Control. 1992.

[149] Jan Pralits. Optimal Design of Natural and Hybrid Laminar Flow Control on Wings. *Department of Mechanics*, (October), 2003.

[150] Dominik K. Puckert and Ulrich Rist. Experiments on critical Reynolds number and global instability in roughness-induced laminar-turbulent transition. *Journal of Fluid Mechanics*, 844:878–904, 2018.

[151] John A. Redford, Neil D. Sandham, and Graham T. Roberts. Compressibility effects on boundary-layer transition induced by an isolated roughness element. *AIAA Journal*, 48(12):2818–2830, 2010.

[152] Eli Reshotko. Transient growth: A factor in bypass transition. *Physics of Fluids*, 13(5):1067–1075, 2001.

[153] Lewis Richardson. *Weather Prediction by Numerical Process*. Cambridge University Press, Cambridge, 1st edition, 2007.

[154] Georgios Rigas, Omar Kamal, Aaron Towne, and Tim Colonius. Efficient global resolvent analysis via the one-way Navier-Stokes equations. Part 2. Optimal response. pages 1–45, 2021.

[155] Steffen Risius, Marco Costantini, Stefan Koch, Stefan Hein, and Christian Klein. Unit Reynolds number, Mach number and pressure gradient effects on laminar–turbulent transition in two-dimensional boundary layers. *Experiments in Fluids*, 59(5):86, may 2018.

[156] W. B. Roberts. Discussion: "The Role of Laminar-Turbulent Transition in Gas Turbine Engines" (Mayle, Robert Edward, 1991, ASME J. Turbomach., 113, pp. 509–536). *Journal of Turbomachinery*, 113(4):536, 1991.

[157] Daniel Rodríguez, Mamta R. Jotkar, and Elmer M. Gennaro. Wavepacket models for subsonic twin jets using 3D parabolized stability equations. *Comptes Rendus - Mecanique*, 1:1–13, 2018.

[158] Daniel Rodriguez, Aniruddha Sinha, Guillaume A. Brès, and Tim Colonius. Acoustic field associated with parabolized stability equation models in turbulent jets. In *19th AIAA/CEAS Aeroacoustics Conference*, Reston, Virginia, 5 2013. American Institute of Aeronautics and Astronautics.

[159] Yannis Sadoudi. Simulation num´ erique de l'interaction soufflante/nacelle en pr´ esence de vent de travers. 2017.

[160] Bijaylakshmi Saikia, Leonard Dueñas, Niclas Dotzauer, and Christoph Brehm. Effect of Parametric Variation of Sinusoidal Surface Roughness on High-Speed Boundary Layer Stability. *AIAA Aviation and Aeronautics Forum and Exposition, AIAA AVIATION Forum 2021*, pages 1–20, 2021.

[161] William S Saric, Helen L Reed, and Edward J Kerschen. Boundary-layer receptivity to freestream disturbances. *Annual Review of Fluid Mechanics*, 34(1):291–319, 1 2002.

[162] William S. Saric, Helen L. Reed, and Edward J. Kerschen. Boundary-layer receptivity to freestream turbulence. *Annual Review of Fluid Mechanics*, 34(1):291–319, 1 2002.

[163] William S. Saric, Helen L. Reed, and Edward B. White. Stability and transition of three-dimensional boundary layers. *Annual Review of Fluid Mechanics*, 35(1989):413–440, 2003.

[164] T Sayadi, JW Nichols, PJ Schmid, and MR Jovanovic. Dynamic mode decomposition of h-type transition to turbulence. In *Proceedings of the Summer Program*, pages 5–14. Center for Turbulence Research, 2012.

[165] Taraneh Sayadi, Curtis W Hamman, and Parviz Moin. Direct numerical simulation of complete h-type and k-type transitions with implications for the dynamics of turbulent boundary layers. *Journal of Fluid Mechanics*, 724:480–509, 2013.

[166] Peter Schmid. Nonmodal stability theory. *Annual Review of Fluid Mechanics*, 39:129–162, 12 2006.

[167] Oliver T. Schmidt, Aaron Towne, Tim Colonius, André V. G. Cavalieri, Peter Jordan, and Guillaume A. Brès. Wavepackets and trapped acoustic modes in a turbulent jet: coherent structure eduction and global stability. *Journal of Fluid Mechanics*, 825:1153–1181, 8 2017.

[168] L.-U. Schrader, L. Brandt, and D. Henningson. Receptivity of boundary layers. *AIAA, Aerospace Sciences Meeting and Exhibit, 31 st, Reno, NV*, page 14, 2008.

[169] Lars U. Schrader, Luca Brandt, and Dan S. Henningson. Receptivity mechanisms in three-dimensional boundary-layer flows. *Journal of Fluid Mechanics*, 618:209–241, 2009.

[170] G B Schubauer and H K Skramstad. Laminar-boundary-layer oscillations and transition on a flat plate. *Journal of Research of the National Bureau of Standards*, 38(February):251–292, 1947.

[171] Aditi Sengupta, VK Suman, and Tapan K Sengupta. Direct numerical simulation of vortex-induced instability for a zero-pressure-gradient boundary layer. *Physical Review E*, 100(3):033118, 2019.

[172] Nima Shahriari, Daniel J. Bodony, Ardeshir Hanifi, and Dan S. Henningson. Acoustic receptivity simulations of flow past a flat plate with elliptic leading edge. *Journal of Fluid Mechanics*, 800:1–11, 2016.

[173] Jie Shen, Tao Tang, and Li-Lian Wang. *Spectral Methods*, volume 41 of *Springer Series in Computational Mathematics*. Springer Berlin Heidelberg, Berlin, Heidelberg, 2011.

[174] Chunhua Sheng. *Advances in Transitional Flow Modeling*. SpringerBriefs in Applied Sciences and Technology. Springer International Publishing, Cham, 2017.

[175] Prakash Shrestha and Graham V Candler. Direct numerical simulation of high-speed transition due to roughness elements. *Journal of Fluid Mechanics*, 868:762–788, 2019.

[176] Jayahar Sivasubramanian and Hermann F Fasel. Direct numerical simulation of transition in a sharp cone boundary layer at mach 6: fundamental breakdown. *Journal of Fluid Mechanics*, 768:175–218, 2015.

[177] Charles R Smith. Aerodynamic heating in hypersonic flows, 2021.

[178] VG Soudakov, AV Fedorov, and IV Egorov. Stability of high-speed boundary layer on a sharp cone with localized wall heating or cooling. *Progress in Flight Physics–Volume 7*, 7:569–584, 2015.

[179] E. M. Sparrow. Fluid-to-fluid conjugate heat transfer for a vertical pipe - internal forced convection and external natural convection. *ASME Journal of Heat Transfer*, 102:402–407, 1980.

[180] E. M. Sparrow. Forced-convection heat transfer in a duct having spanwise-periodic rectangular protuberances. *Numerical Heat Transfer*, 3:149–167, 1980.

[181] Kenneth Stetson and Roger Kimmel. On hypersonic boundary-layer stability. In *30th aerospace sciences meeting and exhibit*, page 737, 1992.

[182] Caihong Su and Heng Zhou. Transition prediction for supersonic and hypersonic boundary layers on a cone with angle of attack. *Science in China, Series G: Physics, Mechanics and Astronomy*, 52(8):1223–1232, 2009.

[183] Caihong Su and Heng Zhou. Transition prediction of a hypersonic boundary layer over a cone at small angle of attack-with the improvement of eN method. *Science in China, Series G: Physics, Mechanics and Astronomy*, 52(1):115–123, 2009.

[184] Pramod K Subbareddy, Matthew D Bartkowicz, and Graham V Candler. Direct numerical simulation of high-speed transition due to an isolated roughness element. *Journal of Fluid Mechanics*, 748:848–878, 2014.

[185] Saikishan Suryanarayanan, David B. Goldstein, Alexandre R. Berger, Edward B. White, and Garry L. Brown. Mechanics of Distributed Roughness Shielding for Suppression of Roughness Induced Boundary Layer Transition. *47th AIAA Fluid Dynamics Conference*, (June):1–17, 2017.

[186] Kunihiko Taira, Steven L Brunton, Scott T M Dawson, Clarence W Rowley, Tim Colonius, Beverley J. McKeon, Oliver T Schmidt, Stanislav Gordeyev, Vassilios Theofilis, and Lawrence S Ukeiley. Modal Analysis of Fluid Flows: An Overview. *AIAA Journal*, 55(12):4013–4041, 12 2017.

[187] DAVID Tempelmann, ARDESHIR HANIFI, and DAN S. HENNINGSON. Spatial optimal growth in three-dimensional boundary layers. *Journal of Fluid Mechanics*, 646:5–37, 2010.

[188] David Tempelmann, Lars-Uve Schrader, Ardeshir Hanifi, Luca Brandt, and Dan S. Henningson. Swept wing boundary-layer receptivity to localized surface roughness. *Journal of Fluid Mechanics*, 711:516–544, 2012.

[189] David Tempelmann, Lars-Uve Schrader, Ardeshir Hanifi, Luca Brandt, and Dan S Henningson. Swept wing boundary-layer receptivity to localized surface roughness. *J. Fluid Mech*, 711:516–544, 2018.

[190] Christian Thomas, Shahid Mughal, Richard Ashworth, Christian Thomas, Shahid Mughal, and Richard Ashworth. On predicting receptivity to surface roughness in a compressible infinite swept wing boundary layer On predicting receptivity to surface roughness in a compressible infinite swept wing boundary layer. 034102:1–30, 2017.

[191] Christian Thomas, Shahid M. Mughal, Hannah Roland, Richard Ashworth, and Alejandro Martinez-Cava. Effect of small surface deformations on the stability of tollmien-schlichting disturbances. *AIAA Journal*, 56(6):2157–2165, 2018.

[192] John Thome, Anubhav Dwivedi, Joseph W Nichols, and Graham V Candler. Direct numerical simulation of bolt hypersonic flight vehicle. In *2018 Fluid Dynamics Conference*, page 2894, 2018.

[193] Vasana Tolieng, Budsabathip Prasirtsak, Jaruwan Sitdhipol, Nuttha Thongchul, and Somboon Tanasupawat. Identification and lactic acid production of bacteria isolated from soils and tree barks. *Malaysian Journal of Microbiology*, 13(2):100–108, 2017.

[194] Aaron Towne, Georgios Rigas, and Tim Colonius. A critical assessment of the parabolized stability equations. *Theoretical and Computational Fluid Dynamics*, 33(3-4):359–382, 2019.

[195] Aaron Towne, Georgios Rigas, Omar Kamal, Ethan Pickering, and Tim Colonius. Efficient global resolvent analysis via the one-way navier–stokes equations. *Journal of Fluid Mechanics*, 948, sep 2022.

[196] Lloyd N. Trefethen. Spectral Methods in MATLAB. 2000.

[197] Andrew Trettel and Johan Larsson. Mean velocity scaling for compressible wall turbulence with heat transfer. *Physics of Fluids*, 28(2):026102, 2016.

[198] Anatoli Tumin and Eli Reshotko. Optimal disturbances in compressible boundary layers. *AIAA journal*, 41(12):2357–2363, 2003.

[199] M. R. Turner and P. W. Hammerton. Asymptotic receptivity analysis and the parabolized stability equation: A combined approach to boundary layer transition. *Journal of Fluid Mechanics*, 562(1992):355–381, 2006.

[200] M. R. Turner and P. W. Hammerton. Asymptotic receptivity analysis and the parabolized stability equation: A combined approach to boundary layer transition. *Journal of Fluid Mechanics*, 562(1992):355–381, 2006.

[201] C. J. Tyson and N. D. Sandham. Numerical simulation of fully-developed compressible flows over wavy surfaces. *International Journal of Heat and Fluid Flow*, 41:2–15, 2013.

[202] VirtusAero. STABL2D. https://virtusaero.com/stabl2d/, 2022. [Online; accessed 19-May-2022].

[203] R. J. Volino, M. P. Schultz, and K. A. Flack. Turbulence structure in rough- and smooth-wall boundary layers. *Journal of Fluid Mechanics*, 592:263–293, 2007.

[204] R. J. Volino, M. P. Schultz, and K. A. Flack. Turbulence structure in rough- and smooth-wall boundary layers. *Journal of Fluid Mechanics*, 592:263–293, 2007.

[205] Wavy Walls and Physical Explanation. Turbulence . Detailed Simulation and Physical Explanation. pages 1–13, 2021.

[206] M Wang, Th Herbert, The Ohio, G K Stuckert, and I Reno. PSE Analysis of Receptivity and Stability in Swept Wing Flows 32nd Aerospace Sciences Meeting & Exhibit. 1994.

[207] Bono Wasistho. *Spatial Direct Numerical Simulation of Compressible Boundary Layer Flow*. Number december. 1996.

[208] Sven Westerbeek. Development of a nonlinear parabolized stability equation (npse) analysis tool for spanwise invariant boundary layers. 2020.

[209] K. J.A. Westin, A. V. Boiko, B. G.B. Klingmann, V. V. Kozlov, and P. H. Alfredsson. Experiments in a boundary layer subjected to free stream turbulence. Part 1. Boundary layer structure and receptivity. *Journal of Fluid Mechanics*, 281(4):193–218, 1994.

[210] Edward B. White. Transient growth of stationary disturbances in a flat plate boundary layer. *Physics of Fluids*, 14(12):4429–4439, 2002.

[211] Yong Sun Wie and Mujeeb R. Malik. Effect of surface waviness on boundary-layer transition in two-dimensional flow. *Computers and Fluids*, 27(2):157–181, 1998.

[212] Xiaohua Wu. New insights into turbulent spots. *Annual Review of Fluid Mechanics*, 55(1), 2023.

[213] Xiaohua Wu and Parviz Moin. Direct numerical simulation of turbulence in a nominally zero-pressure-gradient flat-plate boundary layer. *Journal of Fluid Mechanics*, 630:5–41, 2009.

[214] Xiaohua Wu, Parviz Moin, and Jean-Pierre Hickey. Boundary layer bypass transition. *Physics of Fluids*, 26(9):091104, 9 2014.

[215] Xiaohua Wu, Parviz Moin, James M. Wallace, Jinhie Skarda, Adrián Lozano-Durán, and Jean-Pierre Hickey. Transitional–turbulent spots and turbulent–turbulent spots in boundary layers. *Proceedings of the National Academy of Sciences*, 114(27):E5292–E5299, 7 2017.

[216] Trevor M. Young. An investigation into potential fuel savings for 110-130 seat passenger transport aircraft due to the incorporation of natural laminar flow or hybrid laminar flow control on the engine nacelles. *Proceedings of the Institution of Mechanical Engineers, Part G: Journal of Aerospace Engineering*, 227(8):1300–1324, 2013.

[217] Johannes Zahn and Ulrich Rist. Impact of deep gaps on laminar - Turbulent transition in compressible boundary-layer flow. *AIAA Journal*, 54(1):66–76, 2016.

[218] Yong Ming Zhang and Heng Zhou. Verification of parabolized stability equations for its application to compressible boundary layers. *Applied Mathematics and Mechanics (English Edition)*, 28(8):987–998, 2007.

[219] R Zhao, CY Wen, XD Tian, TH Long, and W Yuan. Numerical simulation of local wall heating and cooling effect on the stability of a hypersonic boundary layer. *International Journal of Heat and Mass Transfer*, 121:986–998, 2018.

[220] Xiaolin Zhong and Xiaowen Wang. Direct numerical simulation on the receptivity, instability, and transition of hypersonic boundary layers. *Annual Review of Fluid Mechanics*, 44:527–561, 2012.

[221] Yunlong Zhou, Wei Liu, Zhenxia Chai, and Xiaoliang Yang. Numerical simulation of wavy surface effect on the stability of a hypersonic boundary layer. *Acta Astronautica*, 140(August):485–496, 2017.

[222] W. K. Zhu, D. W. Gu, W. F. Si, M. J. Zhang, S. Y. Chen, C. R. Smith, Y. D. Zhu, and C. B. Lee. Instability evolution in the hypersonic boundary layer over a wavy wall. *Journal of Fluid Mechanics*, 943:1–32, 2022.

[223] G. Zoppini, S. Westerbeek, D. Ragni, and M. Kotsonis. Receptivity of crossflow instability to discrete roughness amplitude and location. *Journal of Fluid Mechanics*, 939:A33, 2022.

[224] Giulia Zoppini, Daniele Ragni, and Marios Kotsonis. Transition due to isolated roughness in a swept wing boundary layer. *Physics of Fluids*, 34(8):084113, 2022.

[225] Giulia Zoppini, Daniele Ragni, and Marios Kotsonis. Transition due to isolated roughness in a swept wing boundary layer. *Physics of Fluids*, 34(8):084113, 2022.

[226] Simone Zuccher and Paolo Luchini. Boundary-layer receptivity to external disturbances using multiple scales. *Meccanica*, 49(2):441–467, 2014.

APPENDICES

This document is intended to provide a clear derivation of the Compressible Navier-Stokes Equations (CNSE) in curvilinear coordinates as implemented in HybridX.

Appendix A

Governing equations

We begin with the compressible Navier-Stokes for a calorically perfect gas in cartesian coordinates:

$$\frac{\partial \rho}{\partial t} + \frac{\partial \rho u_i}{\partial x_i} = 0 \tag{A.1}$$

$$\frac{\partial \rho u_i}{\partial t} + \frac{\partial}{\partial x_j}\left(\rho u_i u_j + p\delta_{ij}\right) = \frac{\partial \sigma_{ij}}{\partial x_j} \tag{A.2}$$

$$\frac{\partial E}{\partial t} + \frac{\partial}{\partial x_j}\left(u_j(E+p)\right) = \frac{\partial}{\partial x_j}\left(u_i\sigma_{ij} - \kappa\frac{\partial T}{\partial x_j}\right) \tag{A.3}$$

Appendix B

Coordinate transformation

The idea of a coordinate transformation is to map a rectangular on to a body of arbitrary shape. Here we use the following notation:

$$\text{Forward transformation} \qquad\qquad \text{Backward transformation} \qquad\qquad \text{(B.1)}$$

$$x_1 = x_1(\xi_1, \xi_2, \xi_3) \qquad\qquad\qquad \xi_1 = \xi_1(x_1, x_2, x_3) \qquad\qquad \text{(B.2)}$$

$$x_2 = x_2(\xi_1, \xi_2, \xi_3) \qquad\qquad\qquad \xi_2 = \xi_2(x_1, x_2, x_3) \qquad\qquad \text{(B.3)}$$

$$x_3 = x_3(\xi_1, \xi_2, \xi_3) \qquad\qquad\qquad \xi_3 = \xi_3(x_1, x_2, x_3) \qquad\qquad \text{(B.4)}$$

Where x_i and ξ_i are the coordinates in cartesian and curvilinear coordinates, respectively. In general, the forward transformation can be written explicitly using a functional relation. The backward transformation is usually more difficult to define (implicit relationship with x_i).

B.1 Chain rule

$$\frac{\partial \phi}{\partial x_1} = \frac{\partial \phi}{\partial \xi_1}\frac{\partial \xi_1}{\partial x_1} + \frac{\partial \phi}{\partial \xi_2}\frac{\partial \xi_2}{\partial x_1} + \frac{\partial \phi}{\partial \xi_3}\frac{\partial \xi_3}{\partial x_1} \tag{B.5}$$

$$\frac{\partial \phi}{\partial x_2} = \frac{\partial \phi}{\partial \xi_1}\frac{\partial \xi_1}{\partial x_2} + \frac{\partial \phi}{\partial \xi_2}\frac{\partial \xi_2}{\partial x_2} + \frac{\partial \phi}{\partial \xi_3}\frac{\partial \xi_3}{\partial x_2} \tag{B.6}$$

$$\frac{\partial \phi}{\partial x_3} = \frac{\partial \phi}{\partial \xi_1}\frac{\partial \xi_1}{\partial x_3} + \frac{\partial \phi}{\partial \xi_2}\frac{\partial \xi_2}{\partial x_3} + \frac{\partial \phi}{\partial \xi_3}\frac{\partial \xi_3}{\partial x_3} \tag{B.7}$$

In matrix form, the **Jacobian of the backward transformation** reads:

$$\begin{bmatrix} \frac{\partial \phi}{\partial x_1} \\ \frac{\partial \phi}{\partial x_2} \\ \frac{\partial \phi}{\partial x_3} \end{bmatrix} = \begin{bmatrix} \frac{\partial \xi_1}{\partial x_1} & \frac{\partial \xi_2}{\partial x_1} & \frac{\partial \xi_3}{\partial x_1} \\ \frac{\partial \xi_1}{\partial x_2} & \frac{\partial \xi_2}{\partial x_2} & \frac{\partial \xi_3}{\partial x_2} \\ \frac{\partial \xi_1}{\partial x_3} & \frac{\partial \xi_2}{\partial x_3} & \frac{\partial \xi_3}{\partial x_3} \end{bmatrix} \begin{bmatrix} \frac{\partial \phi}{\partial \xi_1} \\ \frac{\partial \phi}{\partial \xi_2} \\ \frac{\partial \phi}{\partial \xi_3} \end{bmatrix} \tag{B.8}$$

As mentioned earlier, the backward is not known in explicit form. The Jacobian of the backward transformation can thus not be computed. To make it possible, we begin with the Jacobian of the forward transformation:

$$x_1 = x_1(\xi_1, \xi_2, \xi_3) \quad \rightarrow \quad dx_1 = \frac{\partial x_1}{\partial \xi_1}d\xi_1 + \frac{\partial x_1}{\partial \xi_2}d\xi_2 + \frac{\partial x_1}{\partial \xi_3}d\xi_3 \quad = \frac{\partial x_1}{\partial \xi_i}d\xi_i$$

$$x_2 = x_2(\xi_1, \xi_2, \xi_3) \quad \rightarrow \quad dx_2 = \frac{\partial x_2}{\partial \xi_1}d\xi_1 + \frac{\partial x_2}{\partial \xi_2}d\xi_2 + \frac{\partial x_2}{\partial \xi_3}d\xi_3 \quad = \frac{\partial x_2}{\partial \xi_i}d\xi_i \tag{B.9}$$

$$x_3 = x_3(\xi_1, \xi_2, \xi_3) \quad \rightarrow \quad dx_3 = \frac{\partial x_3}{\partial \xi_1}d\xi_1 + \frac{\partial x_3}{\partial \xi_2}d\xi_2 + \frac{\partial x_3}{\partial \xi_3}d\xi_3 \quad = \frac{\partial x_3}{\partial \xi_i}d\xi_i$$

Similarly, from the backward transformation, we know that

$$d\xi_1 = \frac{\partial \xi_1}{\partial x_j}dx_j \qquad d\xi_2 = \frac{\partial \xi_2}{\partial x_j}dx_j \qquad d\xi_3 = \frac{\partial \xi_3}{\partial x_j}dx_j \tag{B.10}$$

Substituting equations (B.9) into (B.10) leads to

$$dx_1 = \frac{\partial x_1}{\partial \xi_1}\left(\frac{\partial \xi_1}{\partial x_j}dx_j\right) + \frac{\partial x_1}{\partial \xi_2}\left(\frac{\partial \xi_2}{\partial x_j}dx_j\right) + \frac{\partial x_1}{\partial \xi_3}\left(\frac{\partial \xi_3}{\partial x_j}dx_j\right)$$

$$dx_2 = \frac{\partial x_2}{\partial \xi_1}\left(\frac{\partial \xi_1}{\partial x_j}dx_j\right) + \frac{\partial x_2}{\partial \xi_2}\left(\frac{\partial \xi_2}{\partial x_j}dx_j\right) + \frac{\partial x_2}{\partial \xi_3}\left(\frac{\partial \xi_3}{\partial x_j}dx_j\right) \quad \text{(B.11)}$$

$$dx_3 = \frac{\partial x_3}{\partial \xi_1}\left(\frac{\partial \xi_1}{\partial x_j}dx_j\right) + \frac{\partial x_3}{\partial \xi_2}\left(\frac{\partial \xi_2}{\partial x_j}dx_j\right) + \frac{\partial x_3}{\partial \xi_3}\left(\frac{\partial \xi_3}{\partial x_j}dx_j\right)$$

$$\text{(B.12)}$$

x_1, x_2 and x_3 form an orthonormal basis, therefore, dx_1 cannot be written in terms of dx_2 and/or dx_3 and the only way the equation (B.11) can be true is if

$$dx_1 = \frac{\partial x_1}{\partial \xi_i}\frac{\partial \xi_1}{\partial x_1}dx_1 \quad \text{(B.13)}$$

$$1 = \frac{\partial x_1}{\partial \xi_i}\frac{\partial \xi_1}{\partial x_1} \quad \text{(B.14)}$$

Or, in matrix notation

$$\underbrace{\begin{bmatrix} \frac{\partial x_1}{\partial \xi_1} & \frac{\partial x_1}{\partial \xi_2} & \frac{\partial x_1}{\partial \xi_3} \\ \frac{\partial x_2}{\partial \xi_1} & \frac{\partial x_2}{\partial \xi_2} & \frac{\partial x_2}{\partial \xi_3} \\ \frac{\partial x_3}{\partial \xi_1} & \frac{\partial x_3}{\partial \xi_2} & \frac{\partial x_3}{\partial \xi_3} \end{bmatrix}}_{\text{Forward Jacobian}=[J]} \underbrace{\begin{bmatrix} \frac{\partial \xi_1}{\partial x_1} & \frac{\partial \xi_1}{\partial x_1} & \frac{\partial \xi_1}{\partial x_1} \\ \frac{\partial \xi_2}{\partial x_2} & \frac{\partial \xi_2}{\partial x_2} & \frac{\partial \xi_2}{\partial x_2} \\ \frac{\partial \xi_3}{\partial x_3} & \frac{\partial \xi_3}{\partial x_3} & \frac{\partial \xi_3}{\partial x_3} \end{bmatrix}}_{\text{Backward Jacobian}=[J]^{-1}} = \begin{bmatrix} 1 & 0 & 0 \\ 0 & 1 & 0 \\ 0 & 0 & 1 \end{bmatrix} \quad \text{(B.15)}$$

Therefore, the next task is to find the inverse of the Forward Jacobian $[J]$. Using the Cramer's rule and supposing $[K] = [J]^{-1}$:

$$[K] = \frac{1}{J}\begin{bmatrix} \beta_{11} & \beta_{12} & \beta_{13} \\ \beta_{21} & \beta_{22} & \beta_{23} \\ \beta_{31} & \beta_{32} & \beta_{33} \end{bmatrix} \quad \text{Where } \beta_{ij} = \text{Co-factors of [J] and } J = det(J) \quad \text{(B.16)}$$

154

We thus have the following relationship

$$\frac{\partial \phi}{\partial x_i} = \frac{\beta_{ik}}{J} \frac{\partial \phi}{\partial \xi_k} \tag{B.17}$$

Another way of writing this is

$$\frac{\partial \phi}{\partial x_i} = \frac{1}{J} \frac{\partial}{\partial \xi_k} (\beta_{ik}\phi) \tag{B.18}$$

Therefore

$$\frac{\partial^2 \phi}{\partial x_i \partial x_j} = \frac{1}{J} \frac{\partial}{\partial \xi_k} \left(\beta_{ik} \frac{\partial \phi}{\partial x_j} \right) \tag{B.19}$$

$$\frac{\partial^2 \phi}{\partial x_i \partial x_j} = \frac{1}{J} \frac{\partial}{\partial \xi_k} \left(\beta_{ik} \frac{1}{J} \frac{\partial}{\partial \xi_k} (\beta_{jk}\phi) \right) \tag{B.20}$$

$$\frac{\partial^2 \phi}{\partial x_i \partial x_j} = \frac{1}{J} \frac{\partial}{\partial \xi_k} \left(\beta_{ik}\beta_{jk} \frac{1}{J} \frac{\partial \phi}{\partial \xi_k} \right) \tag{B.21}$$

B.2 Curvilinear Navier-Stokes

B.2.1 Continuity equation

$$\frac{\partial \rho}{\partial t} + \frac{\partial \rho u_i}{\partial x_i} = 0 \tag{B.22}$$

$$\frac{\partial \rho}{\partial t} + \frac{1}{J} \frac{\partial}{\partial \xi_k} (\beta_{ik}\rho u_i) = 0 \tag{B.23}$$

Expanding the terms,

$$\frac{\partial \rho}{\partial t} + \frac{1}{J} \frac{\partial}{\partial \xi_1} (\beta_{i1}\rho u_i) + \frac{1}{J} \frac{\partial}{\partial \xi_2} (\beta_{i2}\rho u_i) + \frac{1}{J} \frac{\partial}{\partial \xi_3} (\beta_{i3}\rho u_i) = 0 \tag{B.24}$$

$$\frac{\partial \rho}{\partial t} + \frac{1}{J}\frac{\partial}{\partial \xi_1} \left(\beta_{11}\rho u_1 + \beta_{21}\rho u_2 + \beta_{31}\rho u_3 \right) \tag{B.25}$$

$$+ \frac{1}{J}\frac{\partial}{\partial \xi_2} \left(\beta_{12}\rho u_1 + \beta_{22}\rho u_2 + \beta_{32}\rho u_3 \right) \tag{B.26}$$

$$+ \frac{1}{J}\frac{\partial}{\partial \xi_3} \left(\beta_{13}\rho u_1 + \beta_{23}\rho u_2 + \beta_{33}\rho u_3 \right) = 0 \tag{B.27}$$

B.2.2   Momentum equations

$$\frac{\partial \rho u_i}{\partial t} + \frac{\partial}{\partial x_j} \left(\rho u_i u_j + p\delta_{ij} \right) = \frac{\partial \sigma_{ij}}{\partial x_j} \tag{B.28}$$

$$\frac{\partial \rho u_i}{\partial t} + \frac{1}{J}\frac{\partial}{\partial \xi_k} \left(\beta_{jk}(\rho u_i u_j + p\delta_{ij}) \right) = \frac{1}{J}\frac{\partial}{\partial \xi_k} \left(\beta_{jk}\sigma_{ij} \right) \tag{B.29}$$

Where

$$\sigma_{ij} = \mu \left(\frac{\partial u_i}{\partial x_j} + \frac{\partial u_j}{\partial x_i} \right) - \frac{2}{3}\mu\frac{\partial u_k}{\partial x_k}\delta_{ij} \tag{B.30}$$

$$\sigma_{ij} = \frac{\mu}{J} \left[\frac{\partial}{\partial \xi_l} \left(\beta_{jl}u_i \right) + \frac{\partial}{\partial \xi_l} \left(\beta_{il}u_j \right) - \frac{2}{3}\frac{\partial}{\partial \xi_l} \left(\beta_{kl}u_k \right) \delta_{ij} \right] \tag{B.31}$$

Expanding the terms,

x-momentum

$$\frac{\partial \rho u_1}{\partial t} + \frac{1}{J}\frac{\partial}{\partial \xi_1}\left(\beta_{j1}(\rho u_1 u_j + p\delta_{ij})\right) \tag{B.32}$$

$$+ \frac{1}{J}\frac{\partial}{\partial \xi_2}\left(\beta_{j2}(\rho u_1 u_j + p\delta_{ij})\right) \tag{B.33}$$

$$+ \frac{1}{J}\frac{\partial}{\partial \xi_3}\left(\beta_{j3}(\rho u_1 u_j + p\delta_{ij})\right) \tag{B.34}$$

$$= \frac{1}{J}\frac{\partial}{\partial \xi_1}\left(\beta_{j1}\sigma_{1j}\right) \tag{B.35}$$

$$+ \frac{1}{J}\frac{\partial}{\partial \xi_2}\left(\beta_{j2}\sigma_{1j}\right) \tag{B.36}$$

$$+ \frac{1}{J}\frac{\partial}{\partial \xi_3}\left(\beta_{j3}\sigma_{1j}\right) \tag{B.37}$$

$$\frac{\partial \rho u_1}{\partial t} + \frac{1}{J}\frac{\partial}{\partial \xi_1}\left(\beta_{11}(\rho u_1 u_1 + p) + \beta_{21}\rho u_1 u_2 + \beta_{31}\rho u_1 u_3\right) \tag{B.38}$$

$$+ \frac{1}{J}\frac{\partial}{\partial \xi_2}\left(\beta_{12}(\rho u_1 u_1 + p) + \beta_{22}\rho u_1 u_2 + \beta_{32}\rho u_1 u_3\right) \tag{B.39}$$

$$+ \frac{1}{J}\frac{\partial}{\partial \xi_3}\left(\beta_{j3}(\rho u_1 u_1 + p) + \beta_{23}\rho u_1 u_2 + \beta_{33}\rho u_1 u_3\right) \tag{B.40}$$

$$= \frac{1}{J}\frac{\partial}{\partial \xi_1}\left(\beta_{11}\sigma_{11} + \beta_{21}\sigma_{12} + \beta_{31}\sigma_{13}\right) \tag{B.41}$$

$$+ \frac{1}{J}\frac{\partial}{\partial \xi_2}\left(\beta_{12}\sigma_{11} + \beta_{22}\sigma_{12} + \beta_{32}\sigma_{13}\right) \tag{B.42}$$

$$+ \frac{1}{J}\frac{\partial}{\partial \xi_3}\left(\beta_{13}\sigma_{11} + \beta_{23}\sigma_{12} + \beta_{33}\sigma_{13}\right) \tag{B.43}$$

$$\frac{\partial \rho u_1}{\partial t} + \frac{1}{J}\frac{\partial}{\partial \xi_1}\left(\rho u_1(\beta_{11}u_1 + \beta_{21}u_2 + \beta_{31}u_3) + \beta_{11}p\right) \tag{B.44}$$

$$+ \frac{1}{J}\frac{\partial}{\partial \xi_2}\left(\rho u_1(\beta_{12}u_1 + \beta_{22}u_2 + \beta_{32}u_3) + \beta_{12}p\right) \tag{B.45}$$

$$+ \frac{1}{J}\frac{\partial}{\partial \xi_3}\left(\rho u_1(\beta_{13}u_1 + \beta_{23}u_2 + \beta_{33}u_3) + \beta_{13}p\right) \tag{B.46}$$

$$= \frac{1}{J}\frac{\partial}{\partial \xi_1}\left(\beta_{11}\sigma_{11} + \beta_{21}\sigma_{12} + \beta_{31}\sigma_{13}\right) \tag{B.47}$$

$$+ \frac{1}{J}\frac{\partial}{\partial \xi_2}\left(\beta_{12}\sigma_{11} + \beta_{22}\sigma_{12} + \beta_{32}\sigma_{13}\right) \tag{B.48}$$

$$+ \frac{1}{J}\frac{\partial}{\partial \xi_3}\left(\beta_{13}\sigma_{11} + \beta_{23}\sigma_{12} + \beta_{33}\sigma_{13}\right) \tag{B.49}$$

Similarly, for the **y-momemtum**

$$\frac{\partial \rho u_2}{\partial t} + \frac{1}{J}\frac{\partial}{\partial \xi_1}\left(\rho u_2(\beta_{11}u_1 + \beta_{21}u_2 + \beta_{31}u_3) + \beta_{21}p\right) \tag{B.50}$$

$$+ \frac{1}{J}\frac{\partial}{\partial \xi_2}\left(\rho u_2(\beta_{12}u_1 + \beta_{22}u_2 + \beta_{32}u_3) + \beta_{22}p\right) \tag{B.51}$$

$$+ \frac{1}{J}\frac{\partial}{\partial \xi_3}\left(\rho u_2(\beta_{13}u_1 + \beta_{23}u_2 + \beta_{33}u_3) + \beta_{23}p\right) \tag{B.52}$$

$$= \frac{1}{J}\frac{\partial}{\partial \xi_1}\left(\beta_{11}\sigma_{21} + \beta_{21}\sigma_{22} + \beta_{31}\sigma_{23}\right) \tag{B.53}$$

$$+ \frac{1}{J}\frac{\partial}{\partial \xi_2}\left(\beta_{12}\sigma_{21} + \beta_{22}\sigma_{22} + \beta_{32}\sigma_{23}\right) \tag{B.54}$$

$$+ \frac{1}{J}\frac{\partial}{\partial \xi_3}\left(\beta_{13}\sigma_{21} + \beta_{23}\sigma_{22} + \beta_{33}\sigma_{23}\right) \tag{B.55}$$

and for the **z-momemtum**

$$\frac{\partial \rho u_3}{\partial t} + \frac{1}{J}\frac{\partial}{\partial \xi_1}\left(\rho u_3(\beta_{11}u_1 + \beta_{21}u_2 + \beta_{31}u_3) + \beta_{31}p\right) \tag{B.56}$$

$$+ \frac{1}{J}\frac{\partial}{\partial \xi_2}\left(\rho u_3(\beta_{12}u_1 + \beta_{22}u_2 + \beta_{32}u_3) + \beta_{32}p\right) \tag{B.57}$$

$$+ \frac{1}{J}\frac{\partial}{\partial \xi_3}\left(\rho u_3(\beta_{13}u_1 + \beta_{23}u_2 + \beta_{33}u_3) + \beta_{33}p\right) \tag{B.58}$$

$$= \frac{1}{J}\frac{\partial}{\partial \xi_1}\left(\beta_{11}\sigma_{31} + \beta_{21}\sigma_{32} + \beta_{31}\sigma_{33}\right) \tag{B.59}$$

$$+ \frac{1}{J}\frac{\partial}{\partial \xi_2}\left(\beta_{12}\sigma_{31} + \beta_{22}\sigma_{32} + \beta_{32}\sigma_{33}\right) \tag{B.60}$$

$$+ \frac{1}{J}\frac{\partial}{\partial \xi_3}\left(\beta_{13}\sigma_{31} + \beta_{23}\sigma_{32} + \beta_{33}\sigma_{33}\right) \tag{B.61}$$

B.2.3 Energy equation

$$\frac{\partial E}{\partial t} + \frac{\partial}{\partial x_j}\left(u_j(E + p)\right) = \frac{\partial}{\partial x_j}\left(u_j\sigma_{ij} - \kappa\frac{\partial T}{\partial x_j}\right) \tag{B.62}$$

$$\frac{\partial E}{\partial t} + \frac{1}{J}\frac{\partial}{\partial \xi_k}\left(\beta_{jk}(u_j(E + p))\right) = \frac{1}{J}\frac{\partial}{\partial \xi_k}\left[\beta_{jk}\left(u_j\sigma_{ij} - \kappa\frac{\partial T}{\partial x_j}\right)\right] \tag{B.63}$$

$$\frac{\partial E}{\partial t} + \frac{1}{J}\frac{\partial}{\partial \xi_k}\left(\beta_{jk}(u_j(E + p))\right) = \frac{1}{J}\frac{\partial}{\partial \xi_k}\left[\beta_{jk}\left(u_i\sigma_{ij} - \frac{\beta_{jl}}{J}\frac{\partial T}{\partial \xi_l}\right)\right] \tag{B.64}$$

Expanding the terms,

$$\frac{\partial E}{\partial t} + \frac{1}{J}\frac{\partial}{\partial \xi_1}\left(\beta_{11}u_1(E + p) + \beta_{21}u_2(E + p) + \beta_{31}u_3(E + p)\right) \tag{B.65}$$

$$+ \frac{1}{J}\frac{\partial}{\partial \xi_2}\left(\beta_{12}u_1(E + p) + \beta_{22}u_2(E + p) + \beta_{32}u_3(E + p)\right) \tag{B.66}$$

$$+ \frac{1}{J}\frac{\partial}{\partial \xi_3}\left(\beta_{13}u_1(E + p) + \beta_{23}u_2(E + p) + \beta_{33}u_3(E + p)\right) \tag{B.67}$$

$$= \textbf{RHS} \tag{B.68}$$

Where

$$\mathbf{RHS} = \frac{1}{J}\frac{\partial}{\partial\xi_1}\bigg[\beta_{11}\left(u_1(\sigma_{11}+\sigma_{21}+\sigma_{31}) - \frac{\beta_{11}}{J}\kappa\frac{\partial T}{\partial\xi_1} - \frac{\beta_{12}}{J}\kappa\frac{\partial T}{\partial\xi_2} - \frac{\beta_{13}}{J}\kappa\frac{\partial T}{\partial\xi_3}\right) \tag{B.69}$$

$$+\beta_{21}\left(u_2(\sigma_{12}+\sigma_{22}+\sigma_{32}) - \frac{\beta_{21}}{J}\kappa\frac{\partial T}{\partial\xi_1} - \frac{\beta_{22}}{J}\kappa\frac{\partial T}{\partial\xi_2} - \frac{\beta_{23}}{J}\kappa\frac{\partial T}{\partial\xi_3}\right) \tag{B.70}$$

$$+\beta_{31}\left(u_3(\sigma_{13}+\sigma_{23}+\sigma_{33}) - \frac{\beta_{31}}{J}\kappa\frac{\partial T}{\partial\xi_1} - \frac{\beta_{32}}{J}\kappa\frac{\partial T}{\partial\xi_2} - \frac{\beta_{33}}{J}\kappa\frac{\partial T}{\partial\xi_3}\right)\bigg] \tag{B.71}$$

$$+\frac{1}{J}\frac{\partial}{\partial\xi_2}\bigg[\beta_{12}\left(u_1(\sigma_{11}+\sigma_{21}+\sigma_{31}) - \frac{\beta_{11}}{J}\kappa\frac{\partial T}{\partial\xi_1} - \frac{\beta_{12}}{J}\kappa\frac{\partial T}{\partial\xi_2} - \frac{\beta_{13}}{J}\kappa\frac{\partial T}{\partial\xi_3}\right) \tag{B.72}$$

$$+\beta_{22}\left(u_2(\sigma_{12}+\sigma_{22}+\sigma_{32}) - \frac{\beta_{21}}{J}\kappa\frac{\partial T}{\partial\xi_1} - \frac{\beta_{22}}{J}\kappa\frac{\partial T}{\partial\xi_2} - \frac{\beta_{23}}{J}\kappa\frac{\partial T}{\partial\xi_3}\right) \tag{B.73}$$

$$+\beta_{32}\left(u_3(\sigma_{13}+\sigma_{23}+\sigma_{33}) - \frac{\beta_{31}}{J}\kappa\frac{\partial T}{\partial\xi_1} - \frac{\beta_{32}}{J}\kappa\frac{\partial T}{\partial\xi_2} - \frac{\beta_{33}}{J}\kappa\frac{\partial T}{\partial\xi_3}\right)\bigg] \tag{B.74}$$

$$+\frac{1}{J}\frac{\partial}{\partial\xi_3}\bigg[\beta_{13}\left(u_1(\sigma_{11}+\sigma_{21}+\sigma_{31}) - \frac{\beta_{11}}{J}\kappa\frac{\partial T}{\partial\xi_1} - \frac{\beta_{12}}{J}\kappa\frac{\partial T}{\partial\xi_2} - \frac{\beta_{13}}{J}\kappa\frac{\partial T}{\partial\xi_3}\right) \tag{B.75}$$

$$+\beta_{23}\left(u_2(\sigma_{12}+\sigma_{22}+\sigma_{32}) - \frac{\beta_{21}}{J}\kappa\frac{\partial T}{\partial\xi_1} - \frac{\beta_{22}}{J}\kappa\frac{\partial T}{\partial\xi_2} - \frac{\beta_{23}}{J}\kappa\frac{\partial T}{\partial\xi_3}\right) \tag{B.76}$$

$$+\beta_{33}\left(u_3(\sigma_{13}+\sigma_{23}+\sigma_{33}) - \frac{\beta_{31}}{J}\kappa\frac{\partial T}{\partial\xi_1} - \frac{\beta_{32}}{J}\kappa\frac{\partial T}{\partial\xi_2} - \frac{\beta_{33}}{J}\kappa\frac{\partial T}{\partial\xi_3}\right)\bigg] \tag{B.77}$$

$$\tag{B.78}$$

B.3 Verification

In Cartesian coordinates, $\beta_{i\neq j} = 0$, $\beta_{ii} = 1$ and $J = 1$. A first verification would be to make sure that we can retrieve the Cartesian equations from the curvilinear system.

B.3.1   Continuity

$$\frac{\partial \rho}{\partial t} + \frac{1}{1}\frac{\partial}{\partial \xi_1}\left(1\rho u_1 + 0\rho u_2 + 0\rho u_3\right) \tag{B.79}$$

$$+ \frac{1}{1}\frac{\partial}{\partial \xi_2}\left(0\rho u_1 + 1\rho u_2 + 0\rho u_3\right) \tag{B.80}$$

$$+ \frac{1}{1}\frac{\partial}{\partial \xi_3}\left(0\rho u_1 + 0\rho u_2 + 1\rho u_3\right) = 0 \tag{B.81}$$

$$\frac{\partial \rho}{\partial t} + \frac{\partial}{\partial \xi_1}\left(\rho u_1\right) + \frac{\partial}{\partial \xi_2}\left(\rho u_2\right) + \frac{\partial}{\partial \xi_3}\left(\rho u_3\right) = 0 \tag{B.82}$$

B.3.2   Momentum

x-momentum

$$\frac{\partial \rho u_1}{\partial t} + \frac{1}{1}\frac{\partial}{\partial \xi_1}\left(\rho u_1(1u_1 + 0u_2 + 0u_3) + 1p\right) \tag{B.83}$$

$$+ \frac{1}{1}\frac{\partial}{\partial \xi_2}\left(\rho u_1(0u_1 + 1u_2 + 0u_3) + 0p\right) \tag{B.84}$$

$$+ \frac{1}{1}\frac{\partial}{\partial \xi_3}\left(\rho u_1(0u_1 + 0u_2 + 1u_3) + 0p\right) \tag{B.85}$$

$$= \frac{1}{1}\frac{\partial}{\partial \xi_1}\left(1\sigma_{11} + 0\sigma_{12} + 0\sigma_{13}\right) \tag{B.86}$$

$$+ \frac{1}{1}\frac{\partial}{\partial \xi_2}\left(0\sigma_{11} + 1\sigma_{12} + 0\sigma_{13}\right) \tag{B.87}$$

$$+ \frac{1}{1}\frac{\partial}{\partial \xi_3}\left(0\sigma_{11} + 0\sigma_{12} + 1\sigma_{13}\right) \tag{B.88}$$

$$\frac{\partial \rho u_1}{\partial t} + \frac{\partial}{\partial \xi_1}\left(\rho u_1 u_1 + p\right) + \frac{\partial}{\partial \xi_2}\left(\rho u_1 u_2\right) + \frac{\partial}{\partial \xi_3}\left(\rho u_1 u_3\right) = \frac{\partial}{\partial \xi_1}\left(\sigma_{11}\right) + \frac{\partial}{\partial \xi_2}\left(\sigma_{12}\right) + \frac{\partial}{\partial \xi_3}\left(\sigma_{13}\right) \tag{B.89}$$

y-momentum

$$\frac{\partial \rho u_2}{\partial t} + \frac{1}{1}\frac{\partial}{\partial \xi_1}\left(\rho u_2(1u_1 + 0u_2 + 0u_3) + 0p\right) \tag{B.90}$$

$$+ \frac{1}{1}\frac{\partial}{\partial \xi_2}\left(\rho u_2(0u_1 + 1u_2 + 0u_3) + 1p\right) \tag{B.91}$$

$$+ \frac{1}{1}\frac{\partial}{\partial \xi_3}\left(\rho u_2(0u_1 + 0u_2 + 1u_3) + 0p\right) \tag{B.92}$$

$$= \frac{1}{1}\frac{\partial}{\partial \xi_1}\left(1\sigma_{21} + 0\sigma_{22} + 0\sigma_{23}\right) \tag{B.93}$$

$$+ \frac{1}{1}\frac{\partial}{\partial \xi_2}\left(0\sigma_{21} + 1\sigma_{22} + 0\sigma_{23}\right) \tag{B.94}$$

$$+ \frac{1}{1}\frac{\partial}{\partial \xi_3}\left(0\sigma_{21} + 0\sigma_{22} + 1\sigma_{23}\right) \tag{B.95}$$

$$\frac{\partial \rho u_2}{\partial t} + \frac{\partial}{\partial \xi_1}\left(\rho u_2 u_1\right) + \frac{\partial}{\partial \xi_2}\left(\rho u_2 u_2 + p\right) + \frac{\partial}{\partial \xi_3}\left(\rho u_2 u_3\right) = \frac{\partial}{\partial \xi_1}\left(\sigma_{21}\right) + \frac{\partial}{\partial \xi_2}\left(\sigma_{22}\right) + \frac{\partial}{\partial \xi_3}\left(\sigma_{23}\right) \tag{B.96}$$

z-momentum

$$\frac{\partial \rho u_3}{\partial t} + \frac{1}{1}\frac{\partial}{\partial \xi_1}\left(\rho u_3(1u_1 + 0u_2 + 0u_3) + 0p\right) \tag{B.97}$$

$$+ \frac{1}{1}\frac{\partial}{\partial \xi_2}\left(\rho u_3(0u_1 + 1u_2 + 0u_3) + 0p\right) \tag{B.98}$$

$$+ \frac{1}{1}\frac{\partial}{\partial \xi_3}\left(\rho u_3(0u_1 + 0u_2 + 1u_3) + 1p\right) \tag{B.99}$$

$$= \frac{1}{1}\frac{\partial}{\partial \xi_1}\left(1\sigma_{31} + 0\sigma_{32} + 0\sigma_{33}\right) \tag{B.100}$$

$$+ \frac{1}{1}\frac{\partial}{\partial \xi_2}\left(0\sigma_{31} + 1\sigma_{32} + 0\sigma_{33}\right) \tag{B.101}$$

$$+ \frac{1}{1}\frac{\partial}{\partial \xi_3}\left(0\sigma_{31} + 0\sigma_{32} + 1\sigma_{33}\right) \tag{B.102}$$

$$\frac{\partial \rho u_3}{\partial t} + \frac{\partial}{\partial \xi_1}(\rho u_3 u_1) + \frac{\partial}{\partial \xi_2}(\rho u_3 u_2) + \frac{\partial}{\partial \xi_3}(\rho u_3 u_3 + p) = \frac{\partial}{\partial \xi_1}(\sigma_{31}) + \frac{\partial}{\partial \xi_2}(\sigma_{32}) + \frac{\partial}{\partial \xi_3}(\sigma_{33})$$

$$\text{(B.103)}$$

B.3.3 Energy equation

$$\frac{\partial E}{\partial t} + \frac{1}{1}\frac{\partial}{\partial \xi_1}\left(1u_1(E+p) + 0u_2(E+p) + 0u_3(E+p)\right) \qquad \text{(B.104)}$$

$$+ \frac{1}{1}\frac{\partial}{\partial \xi_2}\left(0u_1(E+p) + 1u_2(E+p) + 0u_3(E+p)\right) \qquad \text{(B.105)}$$

$$+ \frac{1}{1}\frac{\partial}{\partial \xi_3}\left(0u_1(E+p) + 0u_2(E+p) + 1u_3(E+p)\right) \qquad \text{(B.106)}$$

$$= \mathbf{RHS} \qquad \text{(B.107)}$$

$$\frac{\partial E}{\partial t} + \frac{\partial}{\partial \xi_1}\left(u_1(E+p)\right) + \frac{\partial}{\partial \xi_2}\left(u_2(E+p)\right) + \frac{\partial}{\partial \xi_3}\left(u_3(E+p)\right) = \mathbf{RHS} \qquad \text{(B.108)}$$

Where

$$\mathbf{RHS} = \frac{1}{1}\frac{\partial}{\partial \xi_1}\Big[1\left(u_1(\sigma_{11}+\sigma_{21}+\sigma_{31}) - \frac{1}{1}\kappa\frac{\partial T}{\partial \xi_1} - \frac{0}{1}\kappa\frac{\partial T}{\partial \xi_2} - \frac{0}{1}\kappa\frac{\partial T}{\partial \xi_3}\right) \tag{B.109}$$

$$+0\left(u_2(\sigma_{12}+\sigma_{22}+\sigma_{32}) - \frac{0}{1}\kappa\frac{\partial T}{\partial \xi_1} - \frac{1}{1}\kappa\frac{\partial T}{\partial \xi_2} - \frac{0}{1}\kappa\frac{\partial T}{\partial \xi_3}\right) \tag{B.110}$$

$$+0\left(u_3(\sigma_{13}+\sigma_{23}+\sigma_{33}) - \frac{0}{1}\kappa\frac{\partial T}{\partial \xi_1} - \frac{0}{1}\kappa\frac{\partial T}{\partial \xi_2} - \frac{1}{1}\kappa\frac{\partial T}{\partial \xi_3}\right)\Big] \tag{B.111}$$

$$+\frac{1}{J}\frac{\partial}{\partial \xi_2}\Big[0\left(u_1(\sigma_{11}+\sigma_{21}+\sigma_{31}) - \frac{1}{1}\kappa\frac{\partial T}{\partial \xi_1} - \frac{0}{1}\kappa\frac{\partial T}{\partial \xi_2} - \frac{0}{1}\kappa\frac{\partial T}{\partial \xi_3}\right) \tag{B.112}$$

$$+1\left(u_2(\sigma_{12}+\sigma_{22}+\sigma_{32}) - \frac{0}{1}\kappa\frac{\partial T}{\partial \xi_1} - \frac{1}{1}\kappa\frac{\partial T}{\partial \xi_2} - \frac{0}{1}\kappa\frac{\partial T}{\partial \xi_3}\right) \tag{B.113}$$

$$+0\left(u_3(\sigma_{13}+\sigma_{23}+\sigma_{33}) - \frac{0}{1}\kappa\frac{\partial T}{\partial \xi_1} - \frac{0}{1}\kappa\frac{\partial T}{\partial \xi_2} - \frac{1}{1}\kappa\frac{\partial T}{\partial \xi_3}\right)\Big] \tag{B.114}$$

$$+\frac{1}{1}\frac{\partial}{\partial \xi_3}\Big[0\left(u_1(\sigma_{11}+\sigma_{21}+\sigma_{31}) - \frac{1}{1}\kappa\frac{\partial T}{\partial \xi_1} - \frac{0}{1}\kappa\frac{\partial T}{\partial \xi_2} - \frac{0}{1}\kappa\frac{\partial T}{\partial \xi_3}\right) \tag{B.115}$$

$$+0\left(u_2(\sigma_{12}+\sigma_{22}+\sigma_{32}) - \frac{0}{1}\kappa\frac{\partial T}{\partial \xi_1} - \frac{1}{1}\kappa\frac{\partial T}{\partial \xi_2} - \frac{0}{1}\kappa\frac{\partial T}{\partial \xi_3}\right) \tag{B.116}$$

$$+1\left(u_3(\sigma_{13}+\sigma_{23}+\sigma_{33}) - \frac{0}{1}\kappa\frac{\partial T}{\partial \xi_1} - \frac{0}{1}\kappa\frac{\partial T}{\partial \xi_2} - \frac{1}{1}\kappa\frac{\partial T}{\partial \xi_3}\right)\Big] \tag{B.117}$$

$$\tag{B.118}$$

$$\mathbf{RHS} = \frac{\partial}{\partial \xi_1}\Big[\left(u_1(\sigma_{11}+\sigma_{21}+\sigma_{31}) - \kappa\frac{\partial T}{\partial \xi_1}\right)\Big] \tag{B.119}$$

$$+\frac{\partial}{\partial \xi_2}\Big[\left(u_2(\sigma_{12}+\sigma_{22}+\sigma_{32}) - \kappa\frac{\partial T}{\partial \xi_2}\right)\Big] \tag{B.120}$$

$$+\frac{\partial}{\partial \xi_3}\Big[\left(u_3(\sigma_{13}+\sigma_{23}+\sigma_{33}) - \kappa\frac{\partial T}{\partial \xi_3}\right)\Big] \tag{B.121}$$

$$\tag{B.122}$$

And finally,

$$\frac{\partial E}{\partial t} + \frac{\partial}{\partial \xi_1}\left(u_1(E+p)\right) + \frac{\partial}{\partial \xi_2}\left(u_2(E+p)\right) + \frac{\partial}{\partial \xi_3}\left(u_3(E+p)\right) \tag{B.123}$$

$$= \frac{\partial}{\partial \xi_1}\left[\left(u_1(\sigma_{11} + \sigma_{21} + \sigma_{31}) - \kappa\frac{\partial T}{\partial \xi_1}\right)\right] \tag{B.124}$$

$$+ \frac{\partial}{\partial \xi_2}\left[\left(u_2(\sigma_{12} + \sigma_{22} + \sigma_{32}) - \kappa\frac{\partial T}{\partial \xi_2}\right)\right] \tag{B.125}$$

$$+ \frac{\partial}{\partial \xi_3}\left[\left(u_3(\sigma_{13} + \sigma_{23} + \sigma_{33}) - \kappa\frac{\partial T}{\partial \xi_3}\right)\right] \tag{B.126}$$

$$\tag{B.127}$$

Appendix C

Nonlinear Parabolized Stability Equations (NPSE)

C.1 Compressible Navier-Stokes equations in curvilinear coordinates

Continuity

$$
-pT \left(\frac{\partial u}{\partial x} J_{xx} + \frac{\partial u}{\partial y} J_{yx} + \frac{\partial v}{\partial x} J_{xy} + \frac{\partial v}{\partial y} J_{yy} \right) = T \left[u \frac{\partial p}{\partial x} J_{xx} + v \frac{\partial p}{\partial x} J_{xy} \right]
$$
$$
- p \left[(u J_{xx} + v J_{xy}) \frac{\partial T}{\partial x} + (u J_{yx} + v J_{yy}) \frac{\partial T}{\partial y} \right]
$$
$$
\tag{C.1}
$$

Momentum - x'

$$\rho\left[(uJ_{xx}+vJ_{xy})\frac{\partial u}{\partial x}+(uJ_{yx}+vJ_{yy})\frac{\partial u}{\partial y}\right]$$

$$=-\frac{\partial p}{\partial x}J_{xx}+\frac{1}{Re}\left[\left(\frac{4}{3}\frac{\partial\mu}{\partial x}J_{xx}^2+\frac{\partial\mu}{\partial x}J_{xy}^2+\frac{4}{3}\frac{\partial\mu}{\partial y}J_{xx}J_{yx}+\frac{\partial\mu}{\partial y}J_{yy}J_{xy}\right)\frac{\partial u}{\partial x}\right.$$

$$+\left(\frac{4}{3}\frac{\partial\mu}{\partial x}J_{xx}J_{yx}+\frac{\partial\mu}{\partial x}J_{yy}J_{xy}+\frac{4}{3}\frac{\partial\mu}{\partial y}J_{yx}^2+\frac{\partial\mu}{\partial y}J_{yy}^2\right)\frac{\partial u}{\partial y}+2\mu\left(\frac{4}{3}J_{xx}J_{yx}+J_{xy}J_{yy}\right)\frac{\partial^2 u}{\partial x\partial y}$$

$$+\mu\left(\frac{4}{3}J_{yx}^2+J_{yy}^2\right)\frac{\partial^2 u}{\partial y^2}+\left(\frac{\partial\mu}{\partial x}J_{xy}J_{xx}+\frac{\partial\mu}{\partial y}J_{xx}J_{yy}\right)\frac{\partial v}{\partial x}+\left(\frac{\partial\mu}{\partial x}J_{xy}J_{yx}+\frac{\partial\mu}{\partial y}J_{yy}J_{yx}\right)\frac{\partial v}{\partial y}$$

$$\left.+\mu\frac{\partial^2 v}{\partial x\partial y}\left(J_{yy}J_{xx}+J_{yx}J_{xy}\right)+\mu\frac{\partial v}{\partial y^2}J_{yx}J_{xy}\right]$$

$$\text{(C.2)}$$

Momentum - y'

$$\rho\left[(uJ_{xx}+vJ_{xy})\frac{\partial v}{\partial x}+(uJ_{yx}+vJ_{yy})\frac{\partial v}{\partial y}\right]$$

$$=-\frac{\partial p}{\partial x}J_{xy}+\frac{1}{Re}\left[\left(\frac{4}{3}\frac{\partial\mu}{\partial x}J_{xy}^2+\frac{\partial\mu}{\partial x}J_{xx}^2+\frac{4}{3}\frac{\partial\mu}{\partial y}J_{xy}J_{yy}+\frac{\partial\mu}{\partial y}J_{xx}J_{yx}\right)\frac{\partial v}{\partial x}\right.$$

$$+\left(\frac{4}{3}\frac{\partial\mu}{\partial x}J_{xy}J_{yy}+\frac{\partial\mu}{\partial x}J_{xx}J_{yx}+\frac{4}{3}\frac{\partial\mu}{\partial y}J_{yy}^2+\frac{\partial\mu}{\partial y}J_{yx}^2\right)\frac{\partial v}{\partial y}+2\mu\left(\frac{4}{3}J_{xy}J_{yy}+J_{yx}J_{xx}\right)\frac{\partial^2 v}{\partial x\partial y}$$

$$+\mu\left(\frac{4}{3}J_{yy}^2+J_{yx}^2\right)\frac{\partial^2 v}{\partial y^2}+\left(\frac{\partial\mu}{\partial x}J_{xx}J_{xy}+\frac{\partial\mu}{\partial y}J_{yx}J_{xy}\right)\frac{\partial u}{\partial x}+\left(\frac{\partial\mu}{\partial x}J_{xx}J_{yy}+\frac{\partial\mu}{\partial y}J_{yx}J_{yy}\right)\frac{\partial u}{\partial y}$$

$$\left.+\mu\frac{\partial^2 u}{\partial x\partial y}\left(J_{yy}J_{xx}+J_{yx}J_{xy}\right)+\mu\frac{\partial^2 u}{\partial y^2}J_{yx}J_{xy}\right]$$

$$\text{(C.3)}$$

Momentum - z'

$$\rho\left[(uJ_{xx}+vJ_{xy})\frac{\partial w}{\partial x}+(uJ_{yx}+vJ_{yy})\frac{\partial w}{\partial y}\right]=+\frac{1}{Re}\left[\left(\frac{\partial\mu}{\partial x}J_{xx}^2+\frac{\partial\mu}{\partial x}J_{xy}^2+\frac{\partial\mu}{\partial y}J_{xx}J_{yx}\right.\right.$$

$$+\left.\frac{\partial\mu}{\partial y}J_{xy}J_{yy}\right)\frac{\partial w}{\partial x}+\left(\frac{\partial\mu}{\partial x}J_{xx}J_{yx}+\frac{\partial\mu}{\partial x}J_{xy}J_{yy}\right.$$

$$+\left.\frac{\partial\mu}{\partial y}J_{yx}^2+\frac{\partial\mu}{\partial y}J_{yy}^2\right)\frac{\partial w}{\partial y}$$

$$+2\mu\left(J_{yx}J_{xx}+J_{xy}J_{yy}\right)\frac{\partial^2 w}{\partial x\partial y}$$

$$+\left.\mu\left(J_{yx}^2+J_{yy}^2\right)\frac{\partial w}{\partial^2 y^2}\right]-$$

(C.4)

Energy

$$\rho c_p\left[(uJ_{xx}+vJ_{xy})\frac{\partial T}{\partial x}+(uJ_{yx}+vJ_{yy})\frac{\partial T}{\partial y}\right]$$

$$=\frac{1}{RePr}\left[\left(\frac{\partial\lambda}{\partial x}J_{xx}^2+\frac{\partial\lambda}{\partial x}J_{xy}^2+\frac{\partial\lambda}{\partial y}J_{xx}J_{yx}+\frac{\partial\lambda}{\partial y}J_{xy}J_{yy}\right)\frac{\partial T}{\partial x}\right.$$

$$+\left(\frac{\partial\lambda}{\partial x}J_{xx}J_{yx}+\frac{\partial\lambda}{\partial x}J_{xy}J_{yy}+\frac{\partial\lambda}{\partial y}J_{yy}^2+\frac{\partial\lambda}{\partial y}J_{yx}^2\right)\frac{\partial T}{\partial y}+2\lambda\left(J_{yx}J_{xx}+J_{xy}J_{yy}\right)\frac{\partial^2 T}{\partial x\partial y}$$

$$+\left.\left(J_{yx}^2+J_{yy}^2\right)\frac{\partial T}{\partial y^2}\right]+(\gamma-1)Ma^2\left[uJ_{xx}+vJ_{xy}\right]\frac{\partial p}{\partial x}$$

$$+\frac{\mu(\gamma-1)Ma^2}{Re}\left[\left(\frac{4}{3}J_{xx}^2+J_{xy}^2\right)\left(\frac{\partial u}{\partial x}\right)^2+2\left(\frac{4}{3}J_{xx}J_{yx}+J_{xy}J_{yy}\right)\frac{\partial u}{\partial x}\frac{\partial u}{\partial y}\right.$$

$$+\left(\frac{4}{3}J_{yx}^2+J_{yy}^2\right)\left(\frac{\partial u}{\partial y}\right)^2+\left(\frac{4}{3}J_{xy}^2+J_{xx}^2\right)\left(\frac{\partial v}{\partial x}\right)^2+2\left(\frac{4}{3}J_{xy}J_{yy}+J_{xx}J_{yx}\right)\frac{\partial v}{\partial x}\frac{\partial v}{\partial y}$$

$$+\left(\frac{4}{3}J_{yy}^2+J_{yx}^2\right)\left(\frac{\partial v}{\partial y}\right)^2+(J_{xx}^2+J_{xy}^2)\left(\frac{\partial w}{\partial x}\right)^2+2\left(J_{xx}J_{yx}+J_{xy}J_{yy}\right)\frac{\partial w}{\partial x}\frac{\partial w}{\partial y}$$

$$+\left.(J_{yx}^2+J_{yy}^2)\left(\frac{\partial w}{\partial y}\right)^2+2\left(J_{xx}J_{yx}\frac{\partial v}{\partial x}\frac{\partial u}{\partial x}+J_{xx}J_{yy}\frac{\partial v}{\partial x}\frac{\partial u}{\partial y}+J_{yx}J_{xy}\frac{\partial v}{\partial y}\frac{\partial u}{\partial x}+J_{yx}J_{yy}\frac{\partial v}{\partial y}\frac{\partial u}{\partial y}\right)\right]$$

(C.5)

C.2 PSE in curvilinear coordinates

Continuity

$$-\bar{p}\overline{T}\left[J_{xx}\frac{\partial\hat{u}}{\partial x}+J_{yx}\frac{\partial\hat{u}}{\partial y}+i\alpha(J_{xx}\hat{u}+J_{xy}\hat{v})+J_{yy}\frac{\partial\hat{v}}{\partial y}+J_{xy}\frac{\partial\hat{v}}{\partial x}+i\beta\hat{w}\right]$$

$$-(\bar{p}\hat{T}+\overline{T}\hat{p})\left(J_{xx}\frac{\partial\overline{u}}{\partial x}+J_{yx}\frac{\partial\hat{u}}{\partial y}+J_{yy}\frac{\partial\overline{v}}{\partial y}+J_{xy}\frac{\partial\hat{v}}{\partial x}\right)$$

$$-\left[\overline{u}\left(J_{xx}\frac{\partial\overline{p}}{\partial x}+J_{xy}\frac{\partial\overline{p}}{\partial y}\right)+\overline{v}\left(J_{yy}\frac{\partial\overline{p}}{\partial y}+J_{xy}\frac{\partial\overline{p}}{\partial x}\right)\right]\hat{T}$$

$$-\overline{T}\left[-\omega i\hat{p}+\hat{u}\left(J_{xx}\frac{\partial\overline{p}}{\partial x}+J_{yx}\frac{\partial\overline{p}}{\partial y}\right)+\hat{v}\left(J_{yy}\frac{\partial\overline{p}}{\partial y}+J_{xy}\frac{\partial\overline{p}}{\partial x}\right)+\overline{u}\left(J_{xx}\frac{\partial\hat{p}}{\partial x}+J_{yx}\frac{\partial\hat{p}}{\partial y}+i\alpha J_{xx}\hat{p}\right)\right.$$

$$\left.+\overline{v}\left(J_{yy}\frac{\partial\hat{p}}{\partial y}+J_{xx}\frac{\partial\hat{p}}{\partial x}+i\alpha J_{xy}\hat{p}\right)+\overline{w}\beta i\hat{p}\right]+\left[\overline{u}\left(J_{xx}\frac{\partial\overline{T}}{\partial x}+J_{xy}\frac{\partial\overline{T}}{\partial y}\right)+\overline{v}\left(J_{yy}\frac{\partial\overline{T}}{\partial y}+J_{xy}\frac{\partial\overline{T}}{\partial x}\right)\right]\hat{p}$$

$$+\bar{p}\left[-\omega i\hat{T}+\hat{u}\left(J_{xx}\frac{\partial\overline{T}}{\partial x}+J_{yx}\frac{\partial\overline{T}}{\partial y}\right)+\hat{v}\left(J_{yy}\frac{\partial\overline{T}}{\partial y}+J_{xy}\frac{\partial\overline{T}}{\partial x}\right)+\overline{u}\left(J_{xx}\frac{\partial\hat{T}}{\partial x}+J_{yx}\frac{\partial\hat{T}}{\partial y}+i\alpha J_{xx}\hat{T}\right)\right.$$

$$\left.+\overline{v}\left(J_{yy}\frac{\partial\hat{T}}{\partial y}+J_{xx}\frac{\partial\hat{p}}{\partial x}+i\alpha J_{xy}\hat{T}\right)+\overline{w}\beta i\hat{T}\right]=\exp\left(-i\int_{x}\alpha dx\right)NLT_{cont}$$

$$(C.6)$$

Momentum - x

$$
\overline{\rho}\left(\frac{\hat{p}}{\overline{p}} - \frac{\hat{T}}{\overline{T}}\right)\left[\overline{u}\left(J_{xx}\frac{\partial\overline{u}}{\partial x} + J_{yx}\frac{\partial\overline{u}}{\partial y}\right) + \overline{v}\left(J_{yy}\frac{\partial\overline{u}}{\partial y} + J_{xy}\frac{\partial\overline{u}}{\partial x}\right)\right]
$$

$$
+ \overline{\rho}\left[-\omega i\hat{u} + \overline{u}\left(J_{xx}\frac{\partial\hat{u}}{\partial x} + J_{yx}\frac{\partial\hat{u}}{\partial y}\right) + \overline{v}\left(J_{yy}\frac{\partial\hat{u}}{\partial y} + J_{xy}\frac{\partial\hat{u}}{\partial x}\right)\right.
$$

$$
+ \left(i\beta\overline{w} + i\alpha(\overline{u}J_{xx} + \overline{v}J_{yx}) + J_{xx}\frac{\partial\overline{u}}{\partial x} + J_{yx}\frac{\partial\overline{u}}{\partial y}\right)\hat{u} + \left(J_{yy}\frac{\partial\overline{u}}{\partial y} + J_{xy}\frac{\partial\overline{u}}{\partial x}\right)\hat{v}\right] + J_{xx}\frac{\partial\hat{p}}{\partial x}
$$

$$
+ J_{yx}\frac{\partial\hat{p}}{\partial y} + i\alpha J_{xx}\hat{p} - \frac{\overline{\mu}}{Re}\left[2i\alpha\left(\frac{4}{3}J_{xx}^2 + J_{xy}^2\right)\frac{\partial\hat{u}}{\partial x} + 2i\alpha\left(\frac{4}{3}J_{xx}J_{yx} + J_{xy}J_{yy}\right)\frac{\partial\hat{u}}{\partial y}\right.
$$

$$
+ (i\alpha_x - \alpha^2)\left(\frac{4}{3}J_{xx}^2 + J_{xy}^2\right)\hat{u} - \beta^2\hat{u} + \left(\frac{4}{3}J_{yx}^2 + J_{yy}^2\right)\frac{\partial^2\hat{u}}{\partial y^2} + 2\left(\frac{4}{3}J_{xx}J_{yx} + J_{yy}J_{xy}\right)\frac{\partial^2\hat{u}}{\partial x\partial y}
$$

$$
+ \frac{1}{3}\left(2i\alpha(J_{xx}^2 + 2J_{xx}J_{xy} + J_{xy}^2)\frac{\partial\hat{v}}{\partial x} + 2i\alpha(J_{xx}J_{yy} + J_{xy}(J_{xx} + J_{yy}) + J_{xy}^2) + J_{xy}^2)\frac{\partial\hat{v}}{\partial y}\right.
$$

$$
+ (i\alpha_x - \alpha^2)(J_{xx}^2 + 2J_{xx}J_{xy} + J_{xy}^2)\hat{v} + 2(J_{xx}J_{yy} + J_{xy}^2)\frac{\partial^2\hat{v}}{\partial x\partial y}
$$

$$
+ 2J_{yy}J_{yx}\frac{\partial^2\hat{v}}{\partial y^2} + i\beta J_{xx}\frac{\partial\hat{w}}{\partial x} + i\beta J_{xy}\frac{\partial\hat{w}}{\partial y} - \alpha\beta J_{xx}\hat{w}\right)\right]
$$

$$
- \frac{1}{Re}\left(J_{xx}\frac{\partial\overline{\mu}}{\partial x} + J_{yx}\frac{\partial\overline{\mu}}{\partial y}\right)\left[\frac{4}{3}\left(J_{xx}\frac{\partial\hat{u}}{\partial x} + J_{yx}\frac{\partial\hat{u}}{\partial y} + i\alpha J_{xx}\hat{u}\right)\right.
$$

$$
- \frac{2}{3}\left(J_{yy}\frac{\partial\hat{v}}{\partial y} + J_{xy}\frac{\partial\hat{v}}{\partial x} + i\alpha J_{xy}\hat{v} + i\beta\hat{w}\right)\right]
$$

$$
- \frac{1}{Re}\left(J_{yy}\frac{\partial\overline{\mu}}{\partial y} + J_{xy}\frac{\partial\overline{\mu}}{\partial x}\right)\left[J_{yy}\frac{\partial\hat{u}}{\partial y} + J_{xy}\frac{\partial\hat{u}}{\partial x} + J_{xx}\frac{\partial\hat{v}}{\partial x} + J_{yx}\frac{\partial\hat{v}}{\partial y} + i\alpha J_{xx}\hat{v}\right]
$$

$$
- \frac{1}{Re}\frac{d\overline{\mu}}{d\overline{T}}\left(J_{xx}\frac{\partial\hat{T}}{\partial x} + J_{yx}\frac{\partial\hat{T}}{\partial y} + i\alpha J_{xx}\hat{T}\right)\left[\frac{4}{3}\left(J_{xx}\frac{\partial\overline{u}}{\partial x} + J_{yx}\frac{\partial\overline{u}}{\partial y}\right) - \frac{2}{3}\left(J_y\frac{\partial\overline{v}}{\partial y} + J_{xy}\frac{\partial\overline{v}}{\partial x}\right)\right]
$$

$$
- \frac{1}{Re}\frac{d\overline{\mu}}{d\overline{T}}\left(J_{yy}\frac{\partial\hat{T}}{\partial y} + J_{xy}\frac{\partial\hat{T}}{\partial x} + i\alpha J_{xy}\hat{T}\right)\left[J_{yy}\frac{\partial\overline{u}}{\partial y} + J_{xy}\frac{\partial\overline{u}}{\partial x} + J_{xx}\frac{\partial\overline{v}}{\partial x} + J_{yx}\frac{\partial\overline{v}}{\partial y}\right]
$$

$$
+ \frac{1}{Re}\frac{d\overline{\mu}}{d\overline{T}}\hat{T}\left[\frac{4}{3}\left(J_{xx}^2\frac{\partial^2\overline{u}}{\partial x^2} + 2J_{xx}J_{xy}\frac{\partial^2\overline{u}}{\partial x\partial y} + J_{yx}^2\frac{\partial\overline{u}}{\partial y}\right) + J_{yy}^2\frac{\partial^2\overline{u}}{\partial y^2} + 2J_{yy}J_{xy}\frac{\partial^2\overline{u}}{\partial x\partial y} + J_{xy}^2\frac{\partial^2\overline{u}}{\partial x^2}\right.
$$

$$
+ \frac{1}{3}\left(J_{xx}J_{xy}\frac{\partial^2\overline{v}}{\partial x^2} + J_{yy}J_{yx}\frac{\partial^2\overline{v}}{\partial y^2} + (J_{xx}J_{yy} + J_{xy}^2)\frac{\partial^2\overline{v}}{\partial x\partial y}\right)\right] = \exp\left(-i\int_x\alpha dx\right)NLT_{mom-x}
$$

$$
\text{(C.7)}
$$

Momentum - y

$$\overline{\rho}\left(\frac{\hat{p}}{\overline{p}}-\frac{\hat{T}}{\overline{T}}\right)\left[\overline{u}\left(J_{xx}\frac{\partial\overline{v}}{\partial x}+J_{yx}\frac{\partial\overline{v}}{\partial y}\right)+\overline{v}\left(J_{yy}\frac{\partial\overline{v}}{\partial y}+J_{xy}\frac{\partial\overline{v}}{\partial x}\right)\right]$$

$$+\overline{\rho}\left[-\omega i\hat{v}+\overline{u}\left(J_{xx}\frac{\partial\hat{v}}{\partial x}+J_{yx}\frac{\partial\hat{v}}{\partial y}\right)+\overline{v}\left(J_{yy}\frac{\partial\hat{v}}{\partial y}+J_{xy}\frac{\partial\hat{v}}{\partial x}\right)+\left(i\beta\overline{w}+J_{xx}\frac{\partial\overline{v}}{\partial x}+J_{yx}\frac{\partial\overline{v}}{\partial y}\right)\hat{u}$$

$$+\left(i\alpha(\overline{u}J_{xx}+\overline{v}J_{yx})+J_{yy}\frac{\partial\overline{v}}{\partial y}+J_{xy}\frac{\partial\overline{v}}{\partial x}\right)\hat{v}\right]+J_{yy}\frac{\partial\hat{p}}{\partial y}+J_{xy}\frac{\partial\hat{p}}{\partial x}+i\alpha J_{xx}\hat{p}$$

$$-\frac{\overline{\mu}}{Re}\left[2i\alpha\left(\frac{4}{3}J_{xy}^2+J_{xx}^2\right)\frac{\partial\hat{v}}{\partial x}+2i\alpha\left(\frac{4}{3}J_{xy}J_{yy}+J_{xx}J_{yx}\right)\frac{\partial\hat{v}}{\partial y}+(i\alpha_x-\alpha^2)\left(\frac{4}{3}J_{xy}^2+J_{xx}^2\right)\hat{v}\right.$$

$$-\beta^2\hat{v}+\left(\frac{4}{3}J_{yy}^2+J_{yx}^2\right)\frac{\partial^2\hat{v}}{\partial y^2}+2\left(\frac{4}{3}J_{yy}J_{yx}+J_{xx}J_{yx}\right)\frac{\partial^2\hat{v}}{\partial x\partial y}+\frac{1}{3}\left(2i\alpha(J_{xx}^2+2J_{xx}J_{xy}+J_{xy}^2)\frac{\partial\hat{u}}{\partial x}\right.$$

$$+2i\alpha(J_{xx}J_{yy}+J_{xy}(J_{xx}+J_{yy})+J_{xy}^2)\frac{\partial\hat{u}}{\partial y}+(i\alpha_x-\alpha^2)(J_{xx}^2+2J_{xx}J_{xy}+J_{xy}^2)\hat{u}$$

$$+2(J_{xx}J_{yy}+J_{xy}^2)\frac{\partial^2\hat{u}}{\partial x\partial y}+2J_{yy}J_{yx}\frac{\partial^2\hat{u}}{\partial y^2}+i\beta J_{xy}\frac{\partial\hat{w}}{\partial x}+i\beta J_{yy}\frac{\partial\hat{w}}{\partial y}-\alpha\beta J_{xy}\hat{w}\right)\right]$$

$$-\frac{1}{Re}\left(J_{xx}\frac{\partial\overline{\mu}}{\partial x}+J_{yx}\frac{\partial\overline{\mu}}{\partial y}\right)\left[J_{xx}\frac{\partial\hat{v}}{\partial x}+J_{yx}\frac{\partial\hat{v}}{\partial y}+i\alpha J_{xx}\hat{v}+J_{yy}\frac{\partial\hat{u}}{\partial y}+J_{xy}\frac{\partial\hat{u}}{\partial x}+i\alpha J_{xy}\hat{u}\right]$$

$$-\frac{1}{Re}\left(J_{yy}\frac{\partial\overline{\mu}}{\partial y}+J_{xy}\frac{\partial\overline{\mu}}{\partial x}\right)\left[\frac{4}{3}\left(J_{yy}\frac{\partial\hat{v}}{\partial y}+J_{xy}\frac{\partial\hat{v}}{\partial x}+i\alpha J_{xy}\hat{v}\right)\right.$$

$$-\frac{2}{3}\left(J_{xx}\frac{\partial\hat{u}}{\partial x}+J_{yx}\frac{\partial\hat{u}}{\partial y}+i\alpha J_{xx}\hat{u}+i\beta\hat{w}\right)\right]$$

$$-\frac{1}{Re}\frac{d\overline{\mu}}{d\overline{T}}\left(J_{xx}\frac{\partial\hat{T}}{\partial x}+J_{yx}\frac{\partial\hat{T}}{\partial y}+i\alpha J_{xx}\hat{T}\right)\left[J_{xx}\frac{\partial\overline{v}}{\partial x}+J_{xy}\frac{\partial\overline{v}}{\partial y}+J_{yy}\frac{\partial\overline{u}}{\partial y}+J_{xy}\frac{\partial\overline{u}}{\partial x}\right]$$

$$-\frac{1}{Re}\frac{d\overline{\mu}}{d\overline{T}}\left(J_{yy}\frac{\partial\hat{T}}{\partial y}+J_{xy}\frac{\partial\hat{T}}{\partial x}+i\alpha J_{xy}\hat{T}\right)\left[\frac{4}{3}\left(J_{yy}\frac{\partial\overline{v}}{\partial y}+J_{xy}\frac{\partial\overline{v}}{\partial x}\right)-\frac{2}{3}\left(J_{xx}\frac{\partial\overline{u}}{\partial x}+J_{yx}\frac{\partial\overline{u}}{\partial y}\right)\right]$$

$$+\frac{1}{Re}\frac{d\overline{\mu}}{d\overline{T}}\hat{T}\left[\frac{4}{3}\left(J_{yy}^2\frac{\partial^2\overline{v}}{\partial y^2}+2J_{yy}J_{xy}\frac{\partial^2\overline{v}}{\partial x\partial y}+J_{xy}^2\frac{\partial^2\overline{v}}{\partial x^2}\right)+J_{xx}^2\frac{\partial^2\overline{v}}{\partial x^2}+2J_{xx}J_{xy}\frac{\partial^2\overline{v}}{\partial x\partial y}+J_{xy}^2\frac{\partial^2\overline{v}}{\partial y^2}\right.$$

$$+\frac{1}{3}\left(J_{xx}J_{xy}\frac{\partial^2\overline{u}}{\partial x^2}+J_{yy}J_{yx}\frac{\partial^2\overline{u}}{\partial y^2}+(J_{xx}J_{yy}+J_{xy}^2)\frac{\partial^2\overline{u}}{\partial x\partial y}\right)\right]=\exp\left(-i\int_x\alpha dx\right)NLT_{mom-y}$$

$$(C.8)$$

Momentum - z

$$\overline{\rho}\left(\frac{\hat{p}}{\overline{p}} - \frac{\hat{T}}{\overline{T}}\right)\left[\overline{u}\left(J_{xx}\frac{\partial\overline{w}}{\partial x} + J_{yx}\frac{\partial\overline{w}}{\partial y}\right) + \overline{v}\left(J_{yy}\frac{\partial\overline{w}}{\partial y} + J_{xy}\frac{\partial\overline{w}}{\partial x}\right)\right]$$

$$+ \overline{\rho}\left[-\omega i\hat{w} + \overline{u}\left(J_{xx}\frac{\partial\hat{w}}{\partial x} + J_{yx}\frac{\partial\hat{w}}{\partial y}\right) + \overline{v}\left(J_{yy}\frac{\partial\hat{w}}{\partial y} + J_{xy}\frac{\partial\hat{w}}{\partial x}\right) + \left(i\beta\overline{w} + J_{xx}\frac{\partial\overline{v}}{\partial x} + J_{yx}\frac{\partial\overline{v}}{\partial y}\right)\hat{u}\right.$$

$$+ \left(J_{yy}\frac{\partial\overline{v}}{\partial y} + J_{xy}\frac{\partial\overline{v}}{\partial x}\right)\hat{v} + \left(i\alpha(\overline{u}J_{xx} + \overline{v}J_{yx}) + i\overline{w}\beta\right)\hat{w}\right] - \frac{\overline{\mu}}{Re}\left[2i\alpha J_{xx}^2\frac{\partial\hat{w}}{\partial x} + 2i\alpha J_{xx}J_{yx}\frac{\partial\hat{w}}{\partial y}\right.$$

$$+ \left(i\alpha_x - \alpha^2\right)\left(J_{xx}^2 + J_{xy}^2\right)\hat{w} - \frac{4}{3}\beta^2\hat{w} + \left(J_{yy}^2 + J_{yx}^2\right)\frac{\partial^2\hat{w}}{\partial y^2} + 2\left(J_{yy}J_{xy} + J_{xx}J_{yx}\right)\frac{\partial^2\hat{w}}{\partial x\partial y}$$

$$+ \frac{1}{3}\left(i\beta J_{xx}\frac{\partial\hat{u}}{\partial x} + i\beta J_{yx}\frac{\partial\hat{u}}{\partial y} - \alpha\beta J_{xx}\hat{u} + i\beta J_{xy}\frac{\partial\hat{v}}{\partial x} + i\beta J_{yy}\frac{\partial\hat{v}}{\partial y} - \alpha\beta J_{xy}\hat{v}\right)\right]$$

$$- \frac{1}{Re}\left(J_{xx}\frac{\partial\overline{\mu}}{\partial x} + J_{yx}\frac{\partial\overline{\mu}}{\partial y}\right)\left[J_{xx}\frac{\partial\hat{w}}{\partial x} + J_{yx}\frac{\partial\hat{w}}{\partial y} + i\alpha J_{xx}\hat{w} + i\beta\hat{u}\right]$$

$$- \frac{1}{Re}\left(J_{yy}\frac{\partial\overline{\mu}}{\partial y} + J_{xy}\frac{\partial\overline{\mu}}{\partial x}\right)\left[J_{yy}\frac{\partial\hat{w}}{\partial y} + J_{xy}\frac{\partial\hat{w}}{\partial x} + i\alpha J_{xy}\hat{w} + i\beta\hat{v}\right]$$

$$- \frac{1}{Re}\frac{d\overline{\mu}}{d\overline{T}}\left(J_{xx}\frac{\partial\hat{T}}{\partial x} + J_{yx}\frac{\partial\hat{T}}{\partial y} + i\alpha J_{xx}\hat{T}\right)\left[J_{xx}\frac{\partial\overline{w}}{\partial x} + J_{xy}\frac{\partial\overline{w}}{\partial y}\right]$$

$$- \frac{1}{Re}\frac{d\overline{\mu}}{d\overline{T}}\left(J_{yy}\frac{\partial\hat{T}}{\partial y} + J_{xy}\frac{\partial\hat{T}}{\partial x} + i\alpha J_{xy}\hat{T}\right)\left[\frac{4}{3}\left(J_{yy}\frac{\partial\overline{w}}{\partial y} + J_{xy}\frac{\partial\overline{w}}{\partial x}\right)\right]$$

$$+ \frac{1}{Re}\frac{d\overline{\mu}}{d\overline{T}}\hat{T}\left[J_{yy}^2\frac{\partial^2\overline{w}}{\partial y^2} + 2J_{yy}J_{xy}\frac{\partial^2\overline{w}}{\partial x\partial y} + J_{xy}^2\frac{\partial^2\overline{w}}{\partial x^2} + J_{xx}^2\frac{\partial^2\overline{w}}{\partial x^2}\right.$$

$$+ 2J_{xx}J_{xy}\frac{\partial^2\overline{w}}{\partial x\partial y} + J_{xy}^2\frac{\partial^2\overline{w}}{\partial y^2}\right] = \exp\left(-i\int_x\alpha dx\right)NLT_{mom-z} \tag{C.9}$$

Energy

$$
\begin{aligned}
&\overline{\rho}c_p \left(\frac{\hat{p}}{\overline{p}} - \frac{\hat{T}}{\overline{\overline{T}}} \right) \left[\overline{u} \left(J_{xx}\frac{\partial \overline{T}}{\partial x} + J_{yx}\frac{\partial \overline{T}}{\partial y} \right) + \overline{v} \left(J_{yy}\frac{\partial \overline{T}}{\partial y} + J_{xy}\frac{\partial \overline{T}}{\partial x} \right) \right] \\
&+ \overline{\rho}c_p \left[-\omega i\hat{T} + \overline{u} \left(J_{xx}\frac{\partial \hat{T}}{\partial x} + J_{yx}\frac{\partial \hat{T}}{\partial y} \right) + \overline{v} \left(J_{yy}\frac{\partial \hat{T}}{\partial y} + J_{xy}\frac{\partial \hat{T}}{\partial x} \right) \right. \\
&\left. + \left(J_{xx}\frac{\partial \overline{T}}{\partial x} + J_{yx}\frac{\partial \overline{T}}{\partial y} \right)\hat{u} + \left(J_{yy}\frac{\partial \overline{T}}{\partial y} + J_{xy}\frac{\partial \overline{T}}{\partial x} \right)\hat{v} + \left(i\alpha J_{xx}\overline{u} + i\alpha J_{xy}\overline{v} + i\beta\overline{w} \right)\hat{T} \right] \\
&- \frac{\overline{\lambda}}{RePr} \left[\left(\left(i\alpha_x - \alpha^2 \right) \left(J_{xx}^2 + J_{xy}^2 \right) - \beta^2 \right)\hat{T} + 2i\alpha \left(J_{xx}^2 + J_{xy}^2 \right)\frac{\partial \hat{T}}{\partial x} \right. \\
&\left. + 2i\alpha \left(J_{xx}J_{yx} + J_{yy}J_{xy} \right)\frac{\partial \hat{T}}{\partial y} + \left(J_{yy}^2 + J_{yx}^2 \right)\frac{\partial^2 \hat{T}}{\partial y^2} + 2(J_{xx}J_{yx} + J_{yy}J_{xy})\frac{\partial^2 \hat{T}}{\partial x\partial y} \right] \\
&- \frac{2}{RePr}\frac{d\overline{\lambda}}{d\overline{T}} \left[\left(J_{xx}\frac{\partial \overline{T}}{\partial x} + J_{yx}\frac{\partial \overline{T}}{\partial y} \right) \left(J_{xx}\frac{\partial \hat{T}}{\partial x} + J_{yx}\frac{\partial \hat{T}}{\partial y} + i\alpha J_{xx}\hat{T} \right) \right. \\
&\left. + \left(J_{yy}\frac{\partial \overline{T}}{\partial y} + J_{xy}\frac{\partial \overline{T}}{\partial x} \right) \left(J_{yy}\frac{\partial \hat{T}}{\partial y} + J_{xy}\frac{\partial \hat{T}}{\partial x} + i\alpha J_{xy}\hat{T} \right) \right] \\
&- \frac{1}{RePr}\frac{d\overline{\lambda}}{d\overline{T}}\hat{T} \left((J_{xx}^2 + J_{xy}^2)\frac{\partial^2 \overline{T}}{\partial x^2} + 2(J_{xx}J_{yx} + J_{yy}J_{xy})\frac{\partial^2 \overline{T}}{\partial x\partial y} + (J_{yy} + J_{yx}^2)\frac{\partial^2 \overline{T}}{\partial y^2} \right) \\
&- (\gamma - 1)Ma^2 \left[\overline{u} \left(J_{xx}\frac{\partial \hat{p}}{\partial x} + J_{yx}\frac{\partial \hat{p}}{\partial y} + i\alpha J_{xx}\hat{p} \right) + \overline{v} \left(J_{yy}\frac{\partial \hat{p}}{\partial y} + J_{xy}\frac{\partial \hat{p}}{\partial x} + i\alpha J_{xy}\hat{p} \right) \right. \\
&\left. + \overline{w}\beta i\hat{p} + \left(J_{xx}\frac{\partial \overline{p}}{\partial x} + J_{yx}\frac{\partial \overline{p}}{\partial y} \right)\hat{u} + \left(J_{yy}\frac{\partial \overline{p}}{\partial y} + J_{xy}\frac{\partial \overline{p}}{\partial x} \right)\hat{v} \right] \\
&+ 2\frac{\overline{\mu}(\gamma - 1)Ma^2}{Re}Q_1 + \frac{(\gamma - 1)Ma^2}{Re}Q_2 = \exp\left(-i\int_x \alpha dx \right) NLT_{ener}
\end{aligned}
$$

<div align="right">(C.10)</div>

Where:

$$
\begin{aligned}
Q_1 = {} & \left[\left(\frac{4}{3}J_{xx}^2 + J_{xy}^2\right)\frac{\partial \overline{u}}{\partial x} + \left(\frac{4}{3}J_{xx}J_{xy} + J_{yy}J_{xy}\right)\frac{\partial \overline{u}}{\partial y} + \frac{1}{3}J_{xx}J_{xy}\frac{\partial \overline{v}}{\partial x} + \left(J_{xy}^2 - \frac{2}{3}J_{xx}J_{yy}\right)\frac{\partial \overline{v}}{\partial y}\right]\frac{\partial \hat{u}}{\partial x} \\
& + \left[\left(\frac{4}{3}J_{xx}J_{yx} + J_{yy}J_{xy}\right)\frac{\partial \overline{u}}{\partial x} + \left(\frac{4}{3}J_{yx}^2 + J_{yy}^2\right)\frac{\partial \overline{u}}{\partial y} + \left(J_{xx}J_{yy} - \frac{2}{3}J_{xy}^2\right)\frac{\partial \overline{v}}{\partial x}\right. \\
& \left. + \frac{1}{3}J_{yy}J_{xy}\frac{\partial \overline{v}}{\partial y}\right]\frac{\partial \hat{u}}{\partial y} + i\alpha\left[\left(\frac{4}{3}J_{xx}^2 + J_{xy}^2\right)\frac{\partial \overline{u}}{\partial x} + \left(\frac{4}{3}J_{xx}J_{yx} + J_{yy}J_{xy}\right)\frac{\partial \overline{u}}{\partial y} + \frac{1}{3}J_{xx}J_{xy}\frac{\partial \overline{v}}{\partial x}\right. \\
& \left. + \left(J_{xy}^2 - \frac{2}{3}J_{xx}J_{yy}\right)\frac{\partial \overline{v}}{\partial y}\right]\hat{u} + i\beta\left(J_{xx}\frac{\partial \overline{u}}{\partial x} + J_{yx}\frac{\partial \overline{u}}{\partial y}\right)\hat{u} \\
& + \left[\frac{1}{3}J_{xx}J_{xy}\frac{\partial \overline{u}}{\partial x} + \left(J_{xx}J_{yy} - \frac{2}{3}J_{xy}^2\right)\frac{\partial \overline{u}}{\partial y} + \left(J_{xx}^2 + \frac{4}{3}J_{xy}^2\right)\frac{\partial \overline{v}}{\partial x} + \left(J_{xx}J_{xy} + J_{yy}J_{xy}\right)\frac{\partial \overline{v}}{\partial y}\right]\frac{\partial \hat{v}}{\partial x} \\
& + \left[\left(J_{yx}^2 - \frac{2}{3}J_{xx}J_{yy}\right)\frac{\partial \overline{u}}{\partial x} + \frac{1}{3}J_{yy}J_{yx}\frac{\partial \overline{u}}{\partial y} + \left(J_{xx}J_{yx} + \frac{4}{3}J_{yy}J_{xy}\right)\frac{\partial \overline{v}}{\partial x}\right. \\
& \left. + \left(J_{xy}^2 + \frac{4}{3}J_{yy}^2\right)\frac{\partial \overline{v}}{\partial y}\right]\frac{\partial \hat{v}}{\partial y} + i\alpha\left[\frac{1}{3}J_{xx}J_{xy}\frac{\partial \overline{u}}{\partial x} + \left(J_{xx}J_{yy} - \frac{2}{3}J_{xy}^2\right)\frac{\partial \overline{u}}{\partial y}\right. \\
& \left. + \left(J_{xx}^2 + \frac{4}{3}J_{xy}^2\right)\frac{\partial \overline{v}}{\partial x} + \left(J_{xx}J_{xy} + \frac{4}{3}J_{yy}J_{xy}\right)\frac{\partial \overline{v}}{\partial y}\right]\hat{v} \\
& + i\beta\left(J_{xx}\frac{\partial \overline{u}}{\partial x} + J_{yx}\frac{\partial \overline{u}}{\partial y}\right)\hat{v} + \left[\left(J_{xx}^2 + J_{xy}^2\right)\frac{\partial \overline{w}}{\partial x} + \left(J_{xx}J_{yx} + J_{yy}J_{xy}\right)\frac{\partial \overline{w}}{\partial y}\right]\frac{\partial \hat{w}}{\partial x} \\
& + \left[\left(J_{xx}J_{yx} + J_{yy}J_{xy}\right)\frac{\partial \overline{w}}{\partial x} + \left(J_{yx}^2 + J_{yy}^2\right)\frac{\partial \overline{w}}{\partial y}\right]\frac{\partial \hat{w}}{\partial y} \\
& + i\alpha\left[\left(J_{xx}^2 + J_{xy}^2\right)\frac{\partial \overline{w}}{\partial x} + \left(J_{xx}J_{yx} + J_{yy}J_{xy}\right)\frac{\partial \overline{w}}{\partial y}\right]\hat{w} \\
& - \frac{2}{3}i\beta\left(J_{xx}\frac{\partial \overline{u}}{\partial x} + J_{yx}\frac{\partial \overline{u}}{\partial y} + J_{xy}\frac{\partial \overline{v}}{\partial x} + J_{yy}\frac{\partial \overline{v}}{\partial y}\right)\hat{w}
\end{aligned}
$$

(C.11)

$$Q_2 = \frac{d\overline{\mu}}{d\overline{T}}\hat{T}\left[\left(\frac{4}{3}\left(J_{xx}\frac{\partial\overline{u}}{\partial x} + J_{yx}\frac{\partial\overline{u}}{\partial y}\right) - \frac{2}{3}\left(J_{xy}\frac{\partial\overline{v}}{\partial x} + J_{yy}\frac{\partial\overline{v}}{\partial y}\right)\right)\left(J_{xx}\frac{\partial\overline{u}}{\partial x} + J_{yx}\frac{\partial\overline{u}}{\partial y}\right)\right.$$

$$+ \left(J_{xy}\frac{\partial\overline{u}}{\partial x} + J_{yy}\frac{\partial\overline{u}}{\partial y} + J_{xx}\frac{\partial\overline{v}}{\partial x} + J_{yx}\frac{\partial\overline{v}}{\partial y}\right)\left(J_{xy}\frac{\partial\overline{u}}{\partial x} + J_{yy}\frac{\partial\overline{u}}{\partial y}\right)$$

$$+ \left(J_{xx}\frac{\partial\overline{v}}{\partial x} + J_{yx}\frac{\partial\overline{v}}{\partial y} + J_{xy}\frac{\partial\overline{u}}{\partial x} + J_{yy}\frac{\partial\overline{u}}{\partial y}\right)\left(J_{xx}\frac{\partial\overline{v}}{\partial x} + J_{yx}\frac{\partial\overline{v}}{\partial y}\right) \quad \text{(C.12)}$$

$$+ \left(\frac{4}{3}\left(J_{xy}\frac{\partial\overline{v}}{\partial x} + J_{yy}\frac{\partial\overline{v}}{\partial y}\right) - \frac{2}{3}\left(J_{xx}\frac{\partial\overline{u}}{\partial x} + J_{yx}\frac{\partial\overline{u}}{\partial y}\right)\right)\left(J_{xy}\frac{\partial\overline{v}}{\partial x} + J_{yy}\frac{\partial\overline{v}}{\partial y}\right)$$

$$\left. + \left(J_{xx}\frac{\partial\overline{w}}{\partial x} + J_{yx}\frac{\partial\overline{w}}{\partial y}\right)^2 + \left(J_{xy}\frac{\partial\overline{w}}{\partial x} + J_{yy}\frac{\partial\overline{w}}{\partial y}\right)^2\right]$$